Schweizerische Eidgenossenschaft
Confédération suisse
Confederazione Svizzera
Confederaziun svizra

Eidgenössisches Departement für Umwelt, Verkehr, Energie und Kommunikation UVEK

Bundesamt für Energie BFE

Final report June 2017

# 3D-CRFD models for low $CO_2$/low-emission mixing controlled combustion of biogenic/synthetic fuels in engines based on detailed reaction kinetics

# 3D-CRFD Modelle für $CO_2$- und emissionsarme motorische Brennverfahren bei der diffusionsgesteuerten Verbrennung biogener/synthetischer Kraftstoffe unter Verwendung von detaillierten Reaktionskinetiken

**Datum:** 30th June 2017

**Ort:** Zurich

Auftraggeber:
**Bundesamt für Energie BFE**
**Forschungsprogramm Verbrennung**
**CH-3003 Bern**
www.bfe.admin.ch

Auftragnehmer:
**Combustion and Flow Solutions GmbH**
**Technoparkstrasse 1**
**CH-8005 Zürich**
www.combustion-flow-solutions.com

Autoren:
Dr. Yuri M. Wright,
Combustion and Flow Solutions GmbH, wright@combustion-flow-solutions.com
Dr. Christian Lämmle,
Combustion and Flow Solutions GmbH, laemmle@combustion-flow-solutions.com
Dr. Sushant Pandurangi, Laboratorium für Aerothermochemie und Verbrennungssysteme,
ETH Zürich, pandurangi@lav.mavt.ethz.ch
Dr. Michele Bolla, Laboratorium für Aerothermochemie und Verbrennungssysteme,
ETH Zürich, mbolla@lav.mavt.ethz.ch
Dr. Daniele Farrace, Laboratorium für Aerothermochemie und Verbrennungssysteme,
ETH Zürich, dfarrace@lav.mavt.ethz.ch
Dr. Walter Vera-Tudela, Laboratorium für Aerothermochemie und Verbrennungssysteme,
ETH Zürich, wveratudela@lav.mavt.ethz.ch
Dr. Panagiotis Kyrtatos, Laboratorium für Aerothermochemie und Verbrennungssysteme,
ETH Zürich, kyrtatos@lav.mavt.ethz.ch
Dr. Cheng Qiang, Laboratorium für Aerothermochemie und Verbrennungssysteme,
ETH Zürich, jonny_cheng@lav.mavt.ethz.ch
Dr. Bruno Schneider, Laboratorium für Aerothermochemie und Verbrennungssysteme,
ETH Zürich, schneider@lav.mavt.ethz.ch
Prof. Dr. Konstantinos Boulouchos, Laboratorium für Aerothermochemie und Verbrennungssysteme,
ETH Zürich, boulouchos@lav.mavt.ethz.ch

BFE-Bereichsleiter: **Dr. Carina Alles**
BFE-Programmleiter: **Stephan Renz**
BFE-Vertrags- und TP-Nummer: **SI/500818-01 / 8100075**



**Bundesamt für Energie BFE**
Mühlestrasse 4, CH-3063 Ittigen; Postadresse: CH-3003 Bern
Tel. +41 58 462 56 11 · Fax +41 58 463 25 00 · contact@bfe.admin.ch · www.bfe.admin.ch

# Abstract

This project studies combustion and soot-forming propensity of Diesel surrogates, synthetic and biogenic fuel sprays at engine relevant conditions by means of experiments and three-dimensional Computational Fluid Dynamics. Highspeed imaging of spray morphology (Mie scattering/Schlieren), flame lift-off/penetration evolution (OH*) and combustion generated soot (broadband radiation/3-colour pyrometry) were performed for five pure fuels/blends, incl. *n*-heptane, toluene, *n*-butanol and oxy-methyl-ester. Upgrades to the ETH high-pressure/temperature spray combustion rig include development of a hydrogen precombustion system. Code developments encompass multiple injection adaptation and inclusion of complex kinetics (with in-situ adaptive tabulation). Validation is shown for diesel surrogates with injector diameters from automotive to large two-stroke marine engines (23 conditions). Excellent ignition delay/location, flame structure and soot distributions were predicted for changes in air temperature/oxygen content. The model was also applied to a heavy-duty single cylinder engine (54 conditions) with excellent agreement of pressure/heat release rates and soot/NOx emissions for changes to injection time, temperature and EGR. Post-injections were also studied, providing new insights w.r.t. post-injections soot reduction physics, complementing experimental findings. Simulation of ECN “Spray A” showed excellent ignition/soot timing/location predictions. *n*-butanol/*n*-heptane kinetics representing long-chain alcohol/Diesel blends were identified/tested. Methyl Decanoate kinetics and thermo-physical droplet data were procured and stand-alone testing performed. The developed code demonstrated very good combustion and emission prediction capabilities for wide ranges of operating conditions/injector diameters. It shows considerable promise for application to “classical” and future Low-Temperature Combustion concepts in compression ignition engines for conventional, synthetic and biogenic fuels.

# Kurzfassung

Dieses Projekt untersucht Verbrennung und Russbildungsneigung konventioneller, synthetischer und biogener Kraftstoffsprays bei motorischen Bedingungen mittels optischer Diagnostik und numerischer Simulation. Hochgeschwindigkeitsaufnahmen der Spraymorphologie (Miestreuung/Schlieren), der Flamme (OH*) sowie des Russleuchtens (Dreiwellenpyrometrie) für fünf reine Kraftstoffe bzw. Mischungen davon (*n*-Heptan, Toluen, *n*-Butanol and Oxy-Methyl-Ester) wurden durchgeführt in der weiterentwickelten Hochdruck-Temperaturzelle der ETH, welche um ein $H_2$-Vorverbrennungssystem ergänzt wurde. Die Modellentwicklung umfasste Erweiterungen zur Abbildung von Mehrfacheinspritzungen, sowie In-Situ adaptive Tabellierungsmethoden, welche die Verwendung komplexer Kinetiken ermöglichen. Modellvalidierung erfolgt für Dieselsurrogate im Düsendurchmesserbereich von Automobil- bis Zweitakt-Marinemotoren (23 Betriebspunkte) mit hervorragender Übereinstimmung von Zündverzügen/-orten, Flammenstrukturen und räumlichen Russverteilungen. Das Modell wurde anhand von 54 Punkten eines heavy-duty Dieselmotors weiter validiert mit sehr guter Übereinstimmung von Druck-/Wärmefreisetzungsverläufen und Russ/NOx Emissionen in Funktion von Einspritzzeit, Temperatur und AGR-Rate. Nacheinspritzungen wurden ebenfalls untersucht; dabei wurde ein neues Verständnis der chemisch-physikalischen Prozesse bei Nacheinspritzungen generiert, komplementär zum Experiment. Simulationen des *n*-Dodekan «Spray A» des ECN zeigten ferner ausgezeichnete Übereinstimmung von Zeit/Ort der Zündung bzw. Russemission. Diverse Kinetiken für n-Butanol/n-Heptan repräsentativ für langkettige Alkohol/Dieselmischungen wurden untersucht. Thermochemische Eigenschaften sowie Reaktionskinetiken für Methyldekanoat wurden ferner ausfindig gemacht und getestet. Das entwickelte Modell weist für weite Bereiche der diffusionsgesteuerten Verbrennung und für eine Vielzahl von Kraftstoffen und Betriebsbedingungen sehr gute Vorhersagekraft aus.

# Résumé

Ce projet étudie la combustion et la tendance de formation de suie des sprays de carburant conventionnel, synthétique et biogénique dans le moteur, au moyen de méthodes de diagnostic optique et de simulations numériques. L'imagerie à grande vitesse de la morphologie de pulvérisation (mie scattering/Schlieren), de la flamme (OH*) et du rayonnement des particules de suie (pyrométrie en 3 couleurs) a été réalisée pour cinq combustibles resp. mélanges y inclus *n*-heptane, toluène, *n*-butanol et oxyméthylester. Les expériences ont été réalisées dans le dispositif de combustion à haute pression/température de l'EPFZ; ce dernier fut augmenté par un système de précombustion à hydrogène. Au niveau de la modélisation, les codes ont été adaptés aux injections multiples et à l'inclusion de cinétiques complexes (au moyen de tabulation adaptative). Les modèles ont été validés pour les substituts de diesel avec des injecteurs de diamètres allant de l'automobile aux moteurs marins à deux temps (23 conditions); il résultait une excellente concordance entre les délais et lieux d'allumage, structure de la flamme et des distributions spatiales de suie. De même, le modèle reproduisait les courbes de pression, dégagement de chaleur et émissions de suie et NOx pour 54 variations du temps d'injection, de la température et de la recirculation des gaz d'échappement dans un moteur service intense. Une étude approfondie des post-injections a mené à de nouvelles perceptions des effets physico-chimiques lors de la post-injection, complétant les résultats expérimentaux. Des simulations *n*-Dodécaène «Spray A» de l'ECN conformaient avec les délais et lieux de l'inflammation et du rayonnement de suie. La cinétique du butanol et de l'heptane représentant les mélanges alcool/diesel à longue chaîne a été identifiée et testée. Différents mécanismes réactionnels du *n*-Butanol et *n*-Heptan ont été explorés en lieu d'alcools et des mélanges Diesel à longues chaînes. En plus, les propriétés thermochimiques et mécanismes réactionnels du décanoate de méthyle ont été déterminés. En conclusion, le modèle développé est prédictif pour la combustion par flamme de diffusion sous une large bande de conditions et pour différents combustibles.

# Contents

# Acronyms

| | |
|---|---|
| (a/b)TDC | (after/before) Top Dead Centre |
| AHRR | Apparent Heat Release Rate |
| CA | Crank Angle |
| CFD | Computational Fluid Dynamics |
| CMC | Conditional Moment Closure |
| CPU | Central Processing Unit |
| DI | Direct Integration |
| DME | Dimethyl Ether |
| DOI | Duration Of Injection |
| ET | Energizing Time |
| HTDZ | High Pressure High Temperature spray test rig |
| ID | Ignition Delay |
| ISAT | In-Situ Adaptive Tabulation |
| ECN | Engine Combustion Network |
| EGR | Exhaust Gas Recirculation |
| HRRT | Heat Release Rate |
| (g)IMEP | (gross) Indicated Mean Effective Pressure |
| LAV | Aerothermochemistry and Combustion Technology Laboratory, ETH Zurich |
| LOL | Lift-Off Length |
| LLNL | Lawrence Livermore National Laboratory |
| LTC | Low Temperature Combustion |
| MD | Methyl Decanoate |
| OME | Oxy-Methyl Ether |
| PAH | Polycyclic Aromatic Hydrocarbons |
| PDA | Phase Doppler Anemometry |
| PDF | Probability Density Function |
| PSI | Paul Scherer Institute |
| RANS | Reynolds Averaged Navier-Stokes |
| ROI | Rate Of Injection |
| RPM | Revolutions Per Minute |
| SCC | Spray Combustion Chamber |
| SAE | Society of Automotive Engineers |
| (c)SOI | (commanded) Start Of Injection |
| SOE | Start of Energizing |
| TDC | Top Dead Centre |

# Executive summary

An in-house Conditional Moment Closure (CMC) combustion model has been successfully applied to study spray combustion for different fuels in various test rigs, including two optically accessible spray combustion chambers and a heavy-duty single-cylinder research engine. **Model developments** include the adaptation to account for multiple injection as well as the ability to include more complex kinetics in conjunction with in-situ adaptive tabulation techniques; the combination of the above allows for application to engine relevant injection strategies and fuels, including in particular also oxygenated compounds.

Validation is performed for **diesel surrogates** using data from two spray test rigs, namely an automotive injection configuration as well as orifice diameters ranging from heavy-duty to large two-stroke marine engine nozzles, for 23 operating conditions. Excellent agreement is reported concerning changes in reactivity of the ambient air (temperature and oxygen content) with respect to ignition delay and location, flame structure as well as soot spatial distributions. The developed platform has furthermore been compared to a combustion treatment which neglects turbulence-chemistry interaction, clearly highlighting the advantages of CMC. The model is subsequently applied to study combustion in a heavy-duty single cylinder engine for a total of 54 operating conditions. Excellent predictions are reported in terms of thermodynamic quantities (pressure and heat release rate evolutions) as well as emissions (soot and NOx) as a function of ignition timing, top dead centre temperature and exhaust gas recirculation rate, while the predictive capability with respect to the two-phase flow was previously validated using optical fuel tracer Laser Induced Fluorence data. The impact of post-injections has also been investigated, providing new insights with respect to the chemico-physical processes of soot reduction by means of post injections, thus complementing experimental findings.

Concerning **synthetic fuels**, validation has been perfomed using data from the *n*-dodecane “Spray A” of the Engine Combustion Network. Excellent prediction of ignition delay and location, soot onset timing and location as well as its evolution are reported, confirming the ability of the new code developments to treat complex chemical kinetics. Concerning **biogenic fuels,** *n*-butanol/*n*-heptane kinetics representing blends of longer-chain alcohols with Diesel have been tested and compared to pure *n*-heptane. As a surrogate representing lipid biogenic fuel, Methyl Decanoate kinetics have also undergone stand-alone testing and droplet thermophysical data has further been procured. Overall, the developed simulation platform has demonstrated very good predictive capabilities concerning combustion and emissions over wide ranges of operating conditions and injector orifice dimensions. **The model shows considerable promise concerning its application to present and future combustion concepts in compression ignition engines both for “classical” diesel and Low Temperature Combustion concepts**. Furthermore, the framework allows for the simulation of conventional and biogenic fuels - provided appropriate chemical kinetics and thermophysical properties are available.

Substantial **improvements to the optically accessible spray combustion chamber experimental facility** installed at the Aerothermochemistry and Combustion systems laboratory at ETH have been carried out during this project. The developments include 1) re-design of the control system and installation at a new location, 2) installation of a high-temperature mirror enabling the application of Schlieren double-pass imaging through the larger front-window, 3) recommissioning of a hydrogen pre-combustion system (with spark plug) to reach higher pressure/temperature conditions at start of injection as well as 4) definition and acquisition of standardized coaxial single-orifice injectors with a range of diameters. **Characterization of** the **new injectors** was performed in terms of A) mass flow rate in dependence of

energizing time, injection pressure and back pressure and B) injection rate profiles for different injection and back pressures.

**Measurements** were subsequently performed for a total **of five different fuels**, including *n*-heptane, *n*-heptane/*n*-toluene and *n*-heptane/1-butanol blends as well as two mixtures of Oxy-Methyl-Ethers (OME) for four different ambient temperatures at a constant density for one injection pressure. The techniques applied for **spray characterization** include Mie scattering for the liquid and Schlieren imaging for the vapour phase penetration, OH* chemiluminescence for characterization of lift-off length and flame penetration evolution, as well as measurements of **combustion generated soot** by means of broadband radiation and three-colour pyrometry. An assessment of different methods concerning the determination of ignition delay and locations is further presented.

This project has resulted in eight journal publications and five peer reviewed conference proceedings; **dissemination of the results** has further taken place at four invited talks plus an article in the ERCOFTAC bulletin.

# Motivation and objectives

This project seeks to develop a 3D-CRFD model to be employed in the engine development process for future low $CO_2$/low-emission mixing controlled combustion concepts. Particular emphasis is placed on Diesel surrogates and biogenic/synthetic fuels with appropriately detailed reaction kinetics to enable quantitative predictions of engine relevant parameters. To support the model development and validation, experiments for these fuels will be conducted in the high pressure/high temperature test rig of LAV at ETH Zurich in parallel.

As a combustion model, the Conditional Moment Closure (CMC) code jointly developed by the Aero-thermochemistry and Combustion Systems Laboratory of ETH and Cambridge University will be used as a starting point for the developments foreseen. The model has already seen successful application [1-3] to generic, optically accessible spray combustion test rigs [3, 4]. First inclusion of soot in the CMC context is reported in [5]. All these investigations were carried out using n-heptane, for which thermo-physical properties and chemical kinetics are well understood. For dual-fuel configurations, the model has shown good agreement [6] with experimental ignition delay data from a Rapid Compression Expansion Machine (RCEM) [7]. First successful application of the model to a heavy-duty Diesel engine was reported in [1, 8, 9] using data from [10], with good agreement in terms of pressure evolutions, heat release rates and NOx emissions for changes in load, engine speed, fuel injection parameters and Exhaust Gas Recirculation (EGR).

Motor fuels used in contemporary Internal Combustion Engines (ICE) however include – aside aliphatic components – also cyclic compounds and aromatics, the latter of which exhibit considerable potential for soot formation. In this project, the sooting propensity of such fuels will be assessed experimentally to procure validation data including integral quantities such as photo-multiplier and pressure signals as well as heat release rates. The combination thereof with optical data ignition delay and location and spray lift-off length will allow for in-depth validation of the model.

On the model development side the following bottom-up procedure will be followed:

- Mechanism screening and selection
- Stand-alone testing of kinetics with differing complexity in view of predictive capability and computational resources
- Investigation of different soot precursor species
- Implementation of chosen kinetics in the existing CMC code and extensive testing using optical test rig data.
- Application of the model to engines and validation for wide ranges of operating conditions.

The project is structured in six work packages as detailled below; a summary can be found in Table 1.

In Work Package 1 (**WP1**) suitable surrogates for Diesel are chosen and the combustion model's performance assessed in a first step by means of data from optically accessible test rigs and, later on using engine data for a variety of conditions. In parallel the high-pressure/high-temperature optically accessible test rig from ETH will undergo modifications in **WP3** for lateral mounting of single-orifice fuel injectors to enable optical access through the large window with 90 mm diameter. This will allow for visualization of potentially increased spray penetration lengths of high boiling point synthetic/biogenic fuels or downstream ignition locations e.g. due to prolonged ignition delays of alternative fuels/blends. Measurements are subsequently carried out in **WP4**, first for the Diesel surrogates and in a second step for the synthetic/biogenic fuels.

Model developments for the biogenic/synthetic are performed in **WP2**, starting from a literature survey and screening of existing kinetics in view of their tractability, followed by stand-alone testing. Based on the findings, a selection of fuels will be defined in close collaboration with the funding agency which constitutes a first milestone. Measurements will then be performed for the defined synthetic/biogenic fuels in **WP4**, while the implementation and validation proceeds in parallel in **WP2**.

**WP5** comprises technology transfer of the developed platform, including code documentation and establishment of best practice guidelines.

**WP6** concerns reporting activities to the funding agency as well as dissemination of results throughout the entire project duration by means of publications in journals as well as peer reviewed conferences and workshops.

**Table 1 – work package summary and deliverables**

| **Work package and task descriptions** | **Duration** | **Deliverables** |
|---|---|---|
| AP1 – Diesel surrogate:<br>• Mechanism selection<br>• Stand-alone testing<br>• Application to generic experiments (HTDZ)<br>• Assessment of existing soot models/precursor sensitivity study | PM 1 – 24 | 1. Validated model for Diesel surrogates<br>2. sensitivity study concerning choice of soot precursor species |
| AP2 – Biogenic/synthetic fuels:<br>• Screening<br>• Stand-alone testing<br>• Selection of appropriate mechanisms<br>• Application to HTDZ data/ model validation | PM 12 – 36 | 1. Validated model for synthetic fuels<br>2. Validated model for selected biogenic fuels |
| AP3 – HTDZ test rig modifications | PM 1 – 8 | Lateral injector location for biogenic fuels with high boiling temperatures and long penetration length |
| AP4 – HTDZ experiments:<br>• Diesel surrogates (corresp. AP1)<br>• Biogenic/synthetic fuels (for AP2) | PM 9 – 20<br>PM 21 – 34 | Database with optical data for spray and combustion model validation |
| AP5 – Technology transfer | PM 25 – 38 | Application to engine data to demonstrate predictive capabilities for engine development |
| AP6 – Documentation | PM 1 – 40 | 1. Reporting to funding agency<br>2. Dissemination of results in journals, conferences and workshops<br>3. Best practices guidelines and documentation |

# Model developments for Diesel surrogates (WP1)

In this work package, further validation of the Conditional Moment Closure (CMC) combustion model is performed for by two different optically accessible test rigs, namely the Sandia constant volume combustion chamber ("spray H") and the large marine engine reference experiment Spray Combustion Chamber (SCC). Subsequently the model has been applied to the optically accessible heavy-duty engine installed at Sandia National Laboratories to investigate the impact of changes in operating conditions for variations in Exhaust Gas Recirculation (EGR) rate, Start Of Injection (SOI) timing and Top Dead Centre (TDC) temperature. Finally, post injections are studied for the same engine to further improve the understanding with respect to mechanistics of late soot oxidation. All investigations are carried out using *n-heptane* as a fuel, since this constitutes a well-recognised surrogate for Diesel due to comparable cetane numbers resulting in similar ignition properties.

### *CMC compared to "direct integration" for n-heptane "spray H"*

The well-established CMC model has been compared to a combustion model which does not account for turbulence chemistry interaction. It is also known as "direct integration" (DI) approach, the name originates from the fact, that the Favre averaged temperature and species mass fraction vector are used to calculate the Favre averaged chemical source term. Although this latter approach neglects fluctuations at the subgrid scale, which can be expected to lead to substantial errors especially due to the exponential temperature dependence of the Arrhenius expression in the rate evaluation, this approach has seen successful application to many Diesel engine combustion studies. The goal of this investigation was to elucidate why omitting such apparently important physics, good results can nonetheless be obtained and to identify where the approach has limitations compared to CMC.

**Table 2: Experimental test cases considered with reference case in bold.**

| **Case** | **Gas temperature** (K) | **Gas density** (kg/m$^3$) | **$O_2$** (% vol.) | **Injection duration** (ms) |
|---|---|---|---|---|
| A1 | 1000 | 14.8 | 21 | 6 |
| A2 | 1000 | 14.8 | 15 | 6 |
| A3 | 1000 | 14.8 | 12 | 6 |
| A4 | 1000 | 14.8 | 10 | 6 |
| A5 | 1000 | 14.8 | 8 | 6 |
| B2 | 1000 | 30 | 15 | 6 |
| B3 | 1000 | 30 | 12 | 6 |
| B4 | 1000 | 30 | 10 | 6 |
| B5 | 1000 | 30 | 8 | 6 |
| C1 | 900 | 14.8 | 21 | 6 |
| C2 | 900 | 14.8 | 15 | 6 |
| C4 | 900 | 14.8 | 10 | 6 |
| S3 | 1000 | 14.8 | 12 | 1.8 |

*N-heptane* fuel spray measurements carried out in the Sandia Bomb in [11] have been modelled for a total of 13 different test cases, cf. Table 2. The last operating configuration considered (S3), employs a shorter injection duration to study the spray jet transient after end of injection.

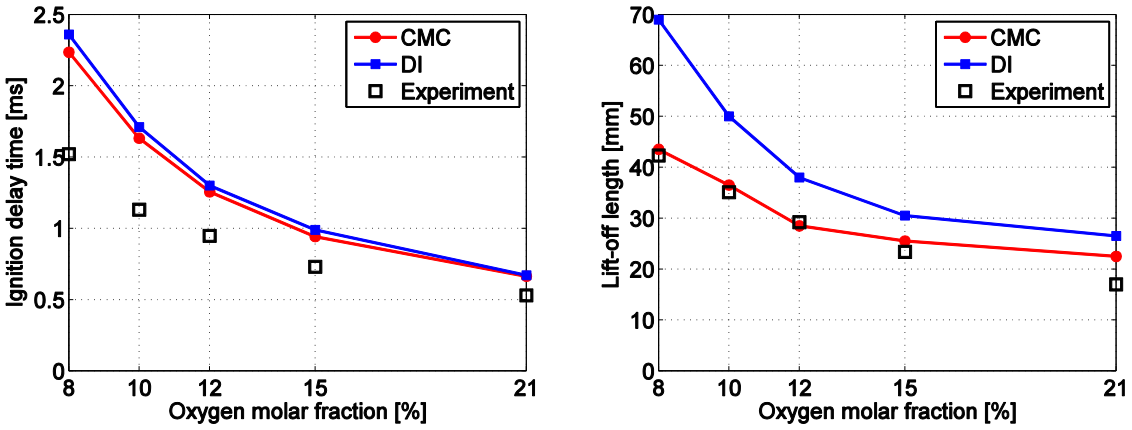


(a) 14.8 kg/m³ and 1000 K

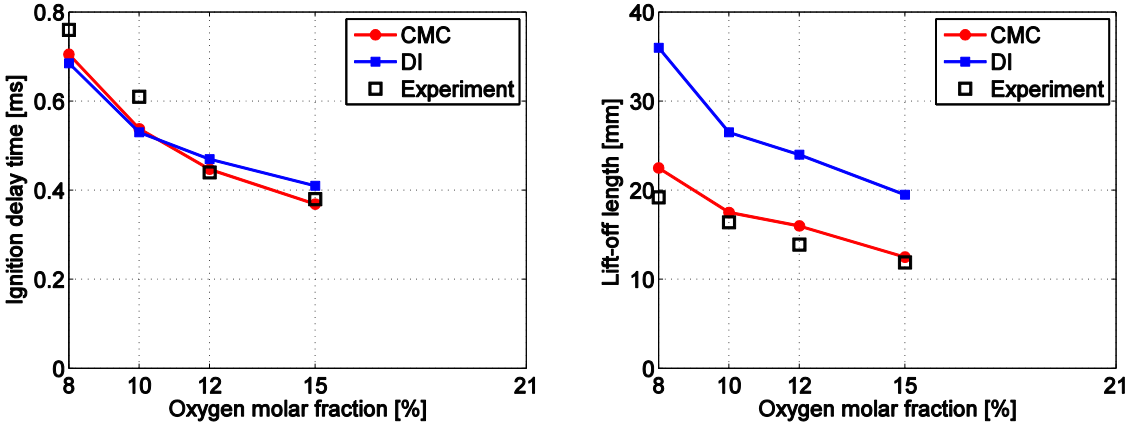


(b) 30 kg/m³ and 1000 K

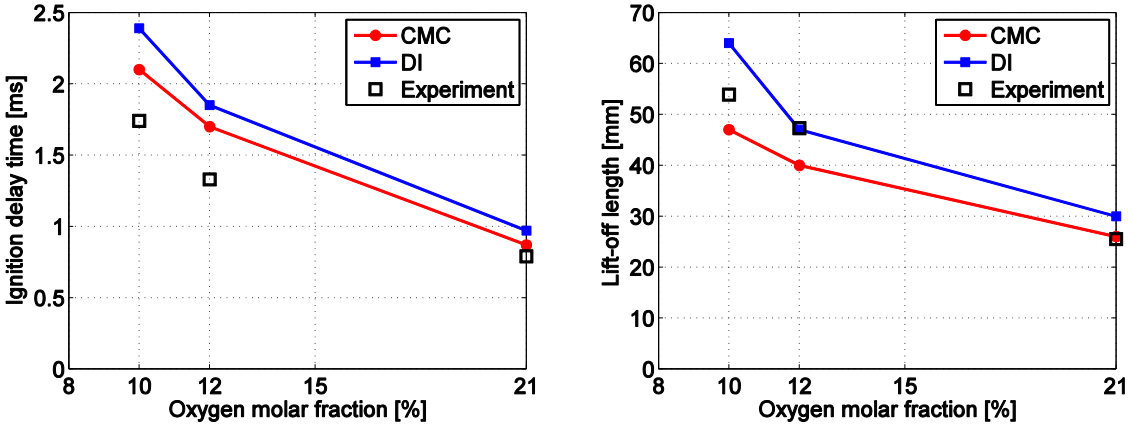


(c) 14.8 kg/m³ and 900 K

**Figure 1: Ignition delay (left) and flame lift-off length (right) as a function of oxygen content for different ambient densities and ambient temperatures.**

In a first step, ignition delays and lift-off lengths have been compared in Figure 1. It is evident, that the direct integration approach and the CMC model predict very similar ignition delays for most conditions. At the higher pressure, which is more relevant to engine conditions, excellent agreement can be observed for the ignition delays for both models. At the lower density, ignition delays are increasingly over-predicted for lower oxygen concentrations (consistently for both models) which can be attributed to the chemical kinetics used; consistent with former studies employing the same chemical kinetics [12].

Overall, both models showed comparable results and more detailed investigations (not shown here) revealed, that auto-ignition under diesel engine conditions occurs prevalently at low values of the scalar dissipation rate. These values are considerably lower than the critical values, and hence turbulence-chemistry interaction plays a minor role because the molecular mixing delaying effects are small. These findings explain why good *ignition delay* predictions can be achieved using direct integration which completely neglects of the turbulent fluctuations.

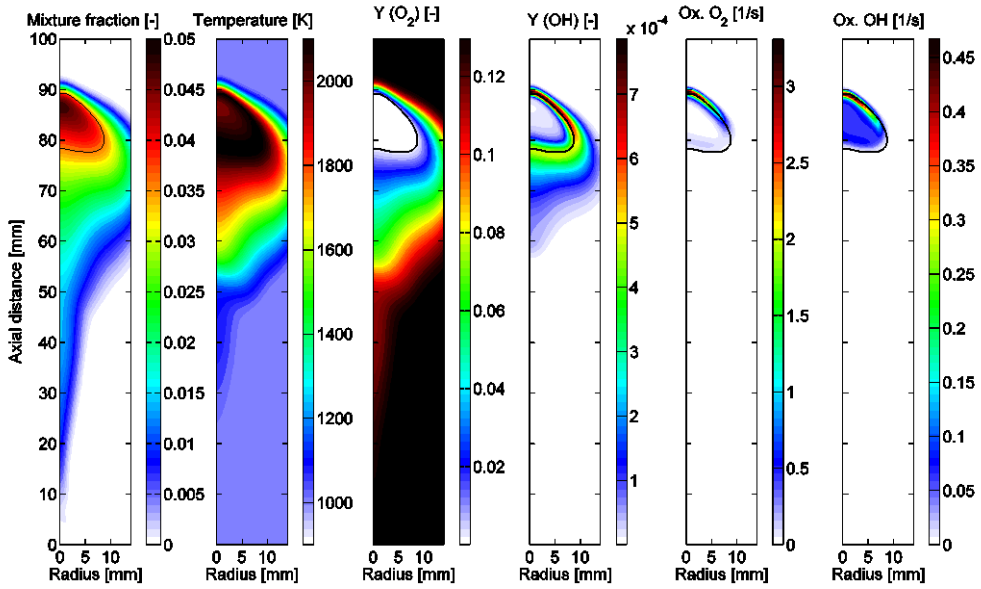


(a) DI

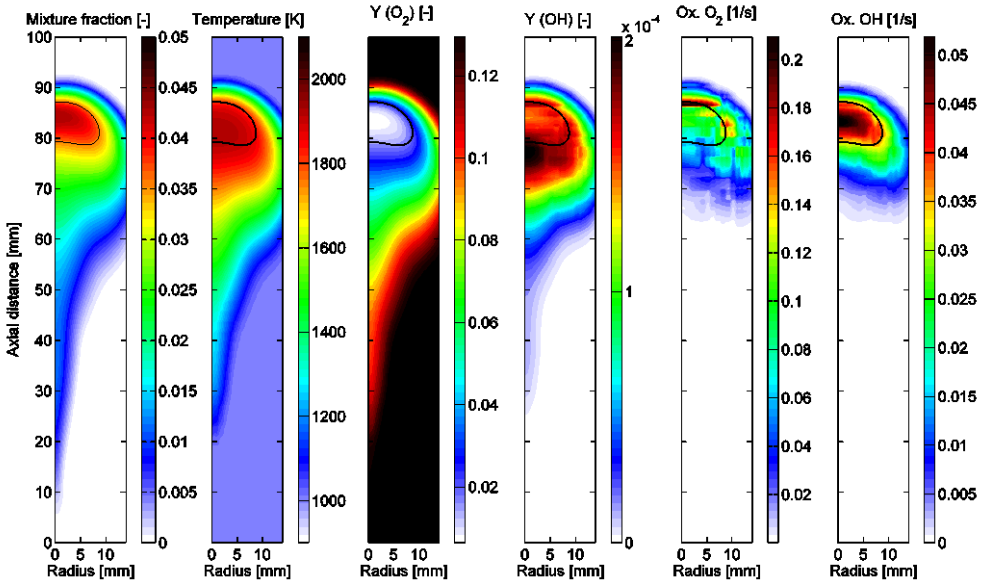


(b) CMC

**Figure 2: Spatial distribution of relevant quantities for flame characterization 3 ms after start of injection for case S3 with DI (a) and CMC (b). From left to right: mean mixture fraction, temperature, mass fractions of oxygen, OH and soot oxidation rate by $O_2$ and OH, respectively. The black line denotes the location of the stoichiometric mixture fraction, $\xi_{ST}$.**

For what concerns flame lift-off lengths, both models capture the correct trend which shows an increase in the lift-off length when decreasing the oxygen content. It is obvious, that for the *lift-off length* the influence of the combustion model is far more prominent: The direct integration approach clearly over-predicts the lift-off length for the majority of cases considered, especially at the lower density and low

oxygen concentrations. The discrepancies are due to the fact, that upstream of the flame stabilisation point, high levels of mixture fraction variance are present, causing a large difference between the mean temperature and the conditional temperature. At the lift-off length itself, the mean value is comparable, but the spread in the mixture fraction PDF is considerably larger, due to the large variance present locally. In such situations, i.e. when high values of variance are present, the evaluation of the non-linear chemical source terms by the DI method using only the mean value and not accounting for these substantial fluctuations leads to large errors.

Soot and related quantities as well as the formation and oxidation rates of soot by OH and $O_2$ have also been investigated to understand the impact of the combustion model; Figure 2 displays iso-contours thereof for the short injection case at 3 ms, i.e. 1.2 ms after the end of injection.

It is evident that the oxidation rate by $O_2$ is higher by an over an order of magnitude compared to CMC. As long as there is separation between the region of soot existence (on the rich side of the stoichiometric iso-line drawn in black) and the availability of oxygen (located exclusively on the side for DI), the soot fields nonetheless remain comparable. Following the end of injection however, air is entrained and with it oxygen, leading to a strong overprediction of the soot oxidation as can be seen in the spatially integrated values in Figure 3.

Figure 4 further evidences this behaviour by means of distributions of spatial natural luminosity illustrating clearly the over-oxidation in the case of direct integration compared. Contrarily, CMC qualitatively shows very good agreement with the experimental distributions, especially at the late stages.

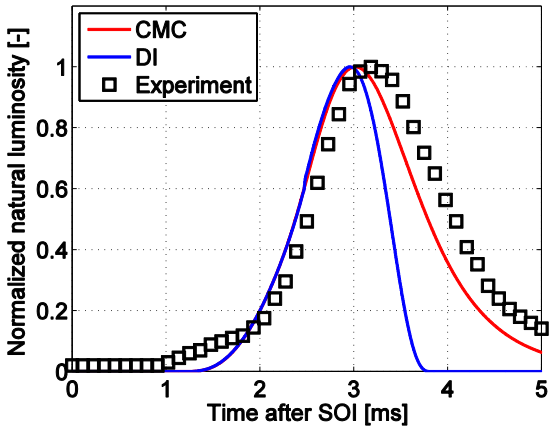


**Figure 3: Temporal evolution of normalized spatially integrated natural luminosity for the S3 case. CMC (red), DI (blue) and experiment (squares).**

It can be concluded, that for the prediction of ignition delay and location, both the direct integration approach as well as CMC provide good results. For the lift-off lengths, accounting for turbulence-chemistry interaction was seen to be important in order to obtain accurate predictions; consequently the CMC model showed considerably better agreement with the experimental data compared to direct integration. Similar findings have also been reported for “Spray A” from the Sandia Engine Combustion Network, e.g. in [13] for a multiple Representative Interactive Flamelet (mRIF) combustion model compared to direct integration, and in [14] where results from a variety of different combustion models are compared against experiments. While quasi-steady soot distributions could be accurately modelled using both approaches, effects due to oxygen entrainment after the end of injection lead to considerably overestimated soot oxidation using direct integration. CMC, which accurately accounts for the co-existence of oxygen and soot in mixture fraction space, showed very good agreement with the experimental data concerning the evolutions of the spatially integrated soot natural luminosity signal as well as the spatial distributions thereof after the end of injection.

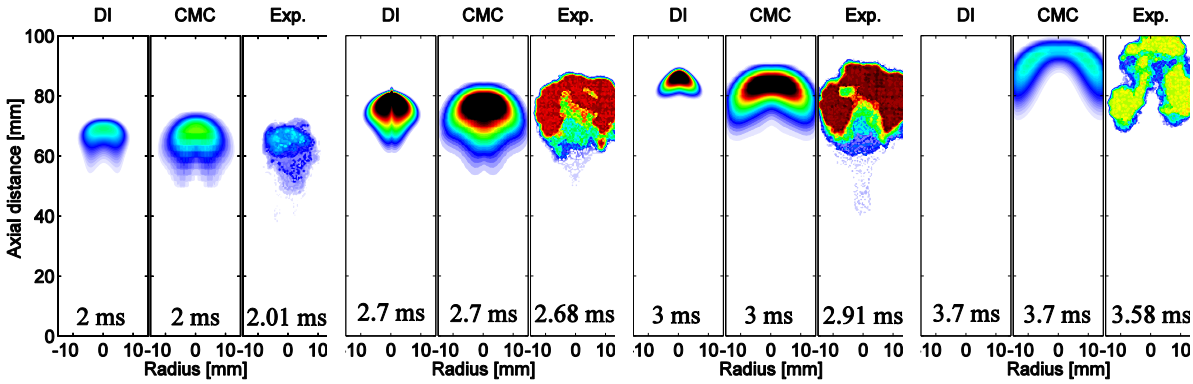


**Figure 4: Evolution of spatial natural luminosity for the S3 case. Simulations (DI and CMC) show soot volume fraction with fixed scale range 0-0.6 $ppm_v$. Experimental data modified from [15]. Times after SOI are indicated at the bottom of each figure.**

These findings have been published in [16].

## *CMC model validation for marine spray combustion chamber*

### Nozzle diameter variation

Further validation of the developed CMC platform has also been carried out by means of data from the Marine Engine reference experiment spray combustion chamber (SCC) installed at Wärtsilä Switzerland. In a recent measurement campaign, experimental data has been procured for a large range of nozzle orifice diameters. In addition to former studies in the literature [17], which covered the range from 50 to 636 µm, in the SCC this range could be expanded up to 1.2 mm, i.e. typical orifice diameters of large two-stroke marine injectors. A total of 5 diameters were investigated, namely 0.2, 0.3, 0.6, 0.875 and 1.2 mm, at two temperatures, a “colder” case at 800 K and a “hotter” one at 900 K; all conditions are summarised in Table 3 below. The density was kept constant to ensure similar momentum transfer conditions in an effort to minimise effects from two-phase related processes. While the facility is capable of heavy fuel oil, in the experiments low sulphur Diesel was used to I) reduce fuel related modelling uncertainties and II) to enable further testing of the developed platform using the same chemical kinetics already proven for smaller configurations.

**Table 3: List of test cases considered for the SCC**

| Case | Nozzle diameter $d_0$ [mm] | Gas pressure [bar] | Gas temperature [K] | Gas density [kg/m$^3$] |
|---|---|---|---|---|
| 1 | 0.2 | 80 | 800 | 33 |
| 2 | 0.2 | 90 | 900 | 33 |
| 3 | 0.3 | 80 | 800 | 33 |
| 4 | 0.3 | 90 | 900 | 33 |
| 5 | 0.6 | 80 | 800 | 33 |
| 6 | 0.6 | 90 | 900 | 33 |
| 7 | 0.875 | 80 | 800 | 33 |
| 8 | 0.875 | 90 | 900 | 33 |
| 9 | 1.2 | 80 | 800 | 33 |
| 10 | 1.2 | 90 | 900 | 33 |

A constant injection duration of roughly 25 ms has been used for all diameters. Depending on the nozzle orifice diameter, the fuel pressure pipe diameter (connecting the common rail to the fuel injector) and the injection pressure (between 650 and 1200 bar) have been varied simultaneously in order to achieve similar pressure evolutions (measured at the injector body upstream of the needle). As a consequence of the large variation in nozzle diameters, naturally very different mass flow rates results.

First ignition delay (ID) times and flame lift off lengths (LOL) predictions are compared to the experimental data. The lift-off length is the distance between the stabilisation point of the quasi-steady burning spray flame closest to the injector and the nozzle exit itself. Subsequently, the early stage flame development is analysed and the influence of the orifice diameter is evaluated by means of ignition behaviour and quasi-steady flame structure. Due to the good agreement and to enable comparisons with former studies presented in [12] for smaller injector diameters, the *n-heptane* chemistry from [18] has been used in this study, also.

Figure 5 shows ID (left) and flame LOL (right) for all orifice diameters. In red are results at 900 K and in blue at 800 K ambient temperature. For the experiment, mean values and standard deviations have been calculated from the 10 injection events, whereas the simulation provides a mean value only as a RANS technique was employed. In terms of ignition delays, the measurements show a clear separation between the two ambient temperatures, where the ignition delays at 800 K are roughly twice the values at 900 K. The standard deviation of the ignition delay showed a larger variability for the lower ambient temperature indicating a larger sensitivity of the ignition delay with respect to temperature at 800 K. The direct influence of the orifice diameter was observed to be less pronounced with a slight increase in ID for larger nozzles at 900 K while at 800 K, ID peaks for the intermediate diameter. Both trends could be qualitatively captured by the simulation.

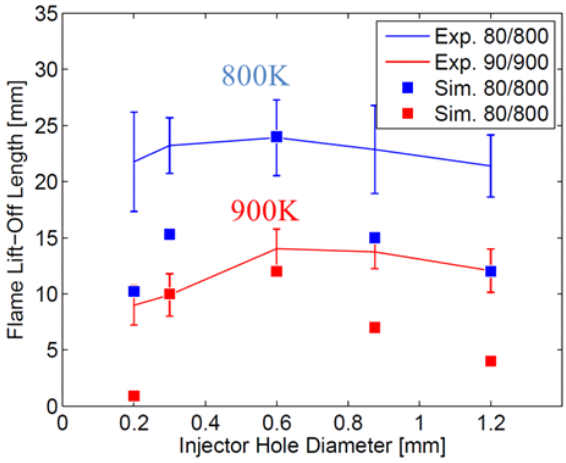


**Figure 5: Comparison of experimental (solid lines) and simulated (squares) ignition delay (left) and flame lift-off length (right)**

For the LOL there is no clear trend. According to [17] a power law of LOL ~ $d^{0.34}$ was proposed for nozzles in the range of 50 to 363 microns. Looking at the 900 K line there is an initial increase in LOL between 0.2 and 0.6 mm and a slight decrease in LOL for larger nozzles. For the colder cases the LOL is roughly twice the values of the warm case and an analogous dependency on $d_0$ was found although less pronounced. Also for LOL the standard deviation for colder conditions is considerably higher.

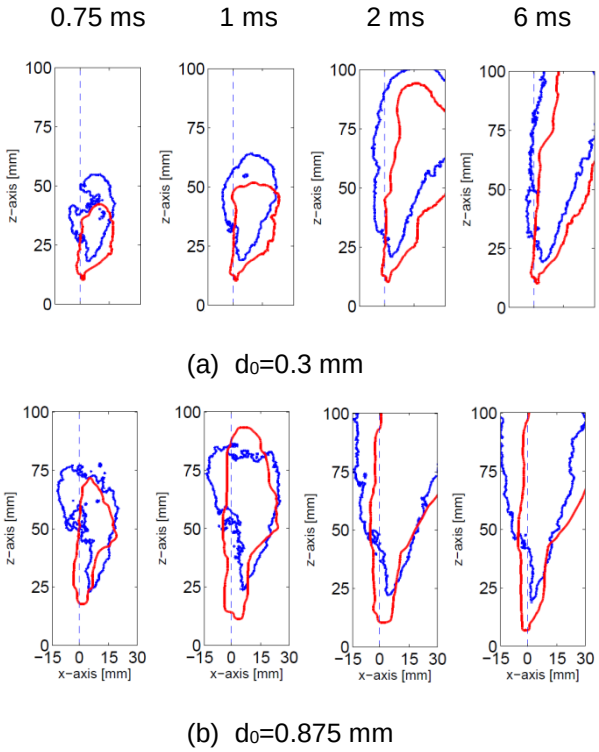


**Figure 6: Temporal evolution of flame region for 0.3 mm (upper) and 0.875 mm (lower) orifice diameter at 900 K. Blue lines experiment, red lines simulation; dashed vertical line denotes spray axis**

In the following the influence of the orifice diameter is studied on the flame region development for two different injector sizes (0.3 and 0.875 mm) at 900 K as displayed in Figure 6 at four different time instants. The experimental flame contours are drawn in blue and the simulation results in red. As a first note, the lateral deviation of the flame by the swirl motion is clearly visible and therefore also the ignition location is shifted in the direction of the swirl where the evaporated fuel is entrained and at later stages a quasi-steady lifted spray flame is established. With the larger injector the ID as well as the LOL are not considerably influenced. On the other hand, the spray penetration is larger and the lateral spray deviation is reduced due to the increased spray momentum generated by the larger fuel mass flow rate. The projected flame area is increased essentially because of the considerably larger amount of fuel injected (factor of 8). The simulation is in qualitative agreement with experimental data although for both cases the LOL is underestimated (cf. Figure 5). The computed spray tip penetrations in the first millisecond for the smaller injector case (upper) is slightly lower than the experiment and the lateral deviation is slightly higher; the overall spray spread is however well described. For the larger injector configuration (bottom) the tip penetration is well reproduced but the lateral deviation of the spray is also overestimated. A possible explanation for this trend is the prediction of a smaller liquid droplet size compared to the experiment and therefore a more pronounced deviation of the spray is observed.

The structure of the flame for the larger injector is shown more in detail in Figure 7 by means of a cut-plane on the injector axis showing from left to right: mean mixture fraction, temperature, mass fractions of OH and $O_2$ and volumetric chemical heat release rate (the latter is drawn in logarithmic scale). Note that the axial extent of the images is 250 mm, i.e. larger than in the former visualizations. The strong evaporation region at around 130 to 150 mm corresponds to the high levels of mixture fraction. Downstream from the LOL a typical diffusion flame is established with high temperature and OH mass fractions are found along the stoichiometric iso-contour.

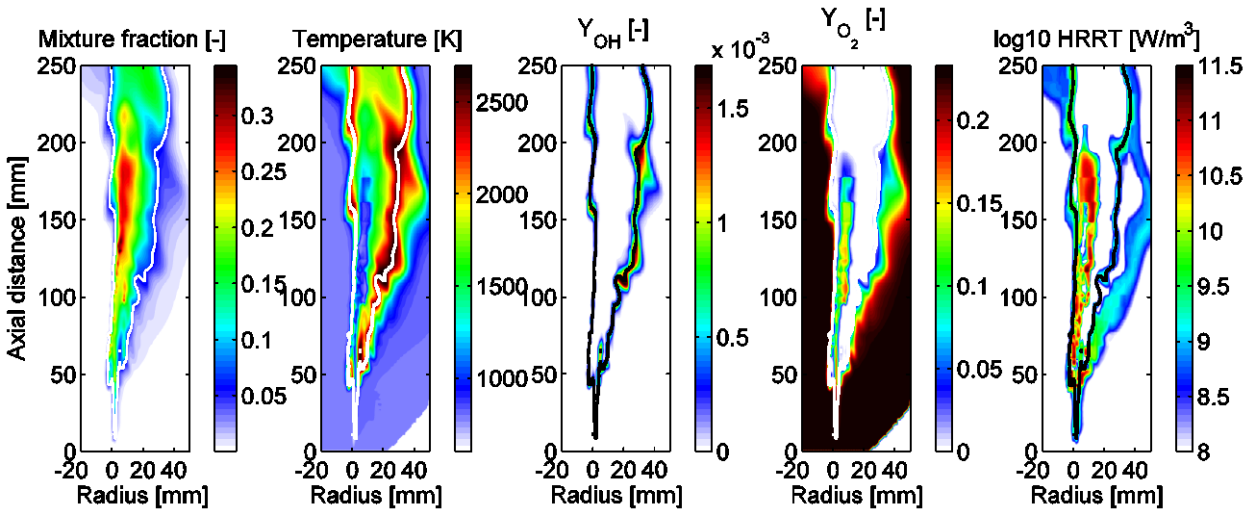


**Figure 7: Isocontours of mixture fraction, temperature, OH, $O_2$ species mass fractions and heat release rate in logarithmic scale. Isolines of the stoichiometric mixture fraction $\xi_{st}$ are superimposed in white or black**

Due to the strong swirling motion, the flame burns more vigorously in the swirl direction side of the spray as recognizable from the temperature distribution. The oxygen is completely consumed in the fuel rich region apart from the region of strong fuel evaporation. This behaviour is characteristic for large injectors with a considerable liquid-flame overlap. The fuel rich region at low temperatures with oxygen remaining is surrounded by a high heat release rate indicating an energetic balance between evaporation and chemical activity. In the strong evaporation region the oxygen is not completely consumed because the heat released by the chemical reaction is counteracted by the heat of evaporation of the fuel. Further downstream (160 to 180 mm) rich combustion takes place and the oxygen is rapidly consumed.

Overall, these findings suggest that CMC is a suitable tool also at nozzle diameters typical of marine engines in the millimetre range, although some discrepancies exist, especially concerning the lift-off length predictions. The findings suggest that for marine injectors, additional effects specific to the nozzle dimensions affecting the two-phase flow field may play an important role, which in the present model are not sufficiently accounted for. Further investigations are currently underway to investigate this matter.

These results were published in the *September 2013 issue of the ERCOFTAC bulletin*, presented at the SAE world congress 2014 and correspondingly published in [19].

## Influence of evaporation terms for large bore nozzle diameters

Substantial overlap between the dense fuel spray and flame area is encountered for sprays in typical large two-stroke marine diesel engines which employ fuel injectors with orifice diameters of the order of one millimeter motivating further research into the effect of evaporation. In a first step, the simulation results are validated by means of experimental data from the Wärtsilä optically accessible marine spray combustion chamber, in terms of non-reactive macroscopic spray development. Subsequently, reactive calculations are carried out and validated in terms of ignition delay time, ignition location, flame lift-off length and temporal evolution of the flame region. Finally, the influence of droplet terms on spray combustion is analyzed in detail. Accounting for evaporation effects into the mixture fraction variance transport equation was seen to play a prominent role concerning auto-ignition and flame stabilization: both ignition delay and flame lift-off length are considerably increased when evaporation effects are included. This was found to be attributed to the strong spatial overlap between evaporation and combustion – typical for marine sprays – leading to an increase in the local scalar dissipation rate in the evaporating region. The droplet term in the mixture fraction variance equation was found to be the main source of mixture fraction variance, suggesting that the scalar dissipation rate induced by evaporation

is most prominent mechanism controlling auto-ignition and flame stabilization for the large injectors utilized in marine diesel applications. The influence of these droplet terms by comparing reactive simulations with and without droplet terms. An idealized rectangular injection rate profile with injection velocity of 380 m/s (corresponding to injection pressure of 600 bar) has been used in order to minimize effects related to the injection profile. Ignition delay, lift-off length and ignition location are compared with experimental values for both simulations in Table 4.

**Table 4: Influence of droplet term on ignition delay, lift-off length and ignition location.**

| Property | Experiment | Droplet terms included | Droplet terms excluded |
|---|---|---|---|
| Ignition delay [ms] | 0.50 | 0.49 | 0.40 |
| Axial ignition location [mm] | 30 | 38 | 48 |
| Radial ignition location [mm] | 4 | 5 | 4 |
| Flame lift-off [mm] | 14 | 17 | 2 |

As seen in Figure 8, autoignition for both cases occurs on the swirl-leeward side of the spray. The simulation with droplet terms results in 1 to 2 orders of magnitude higher local scalar dissipation rate. At the time of autoignition, scalar dissipation rate without droplet terms does not exceed values of 40 $s^{-1}$, whereas with droplet terms scalar dissipation rate is of the order of several hundreds. Inclusion of droplet terms results in a retarded ignition delay by approximately 90 µs, the ignition spot is shifted towards more favorable conditions side- and downwards closer to the stoichiometric contour, being closer to experimentally observed values.

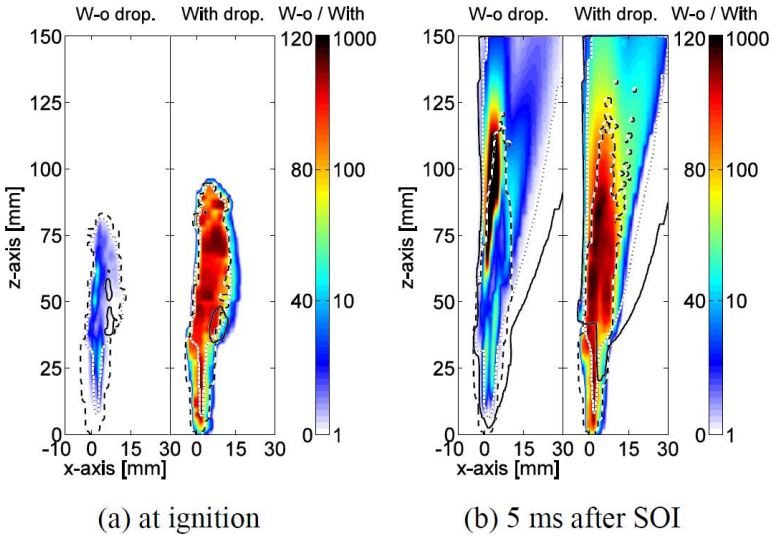


**Figure 8: Distribution of the scalar dissipation rate at 100 µs after start of combustion (a) and at 5 ms after SOI (b). The figure pairs compare simulation results without droplet terms (left halves) and with droplet term (right halves); the corresponding scales are 0-120 $s^{-1}$ (linear scale) and 0-1000 $s^{-1}$ (logarithmic scale). Overlaid contours: liquid b/w dotted, stoichiometry b/w dashed, flame black solid.**

Concerning the quasi-steady flame: the main difference between the two models, apart from the scalar dissipation rate and lift-off length, is the Heat Release Rate (HRRT) and consequent $O_2$ distribution in the centre of the spray. Without droplet terms, some oxygen still persist until approximately 125 mm in concomitance with HRRT. The diffusion flame along the stoichiometric condition is comparable, as shown in Figure 9.

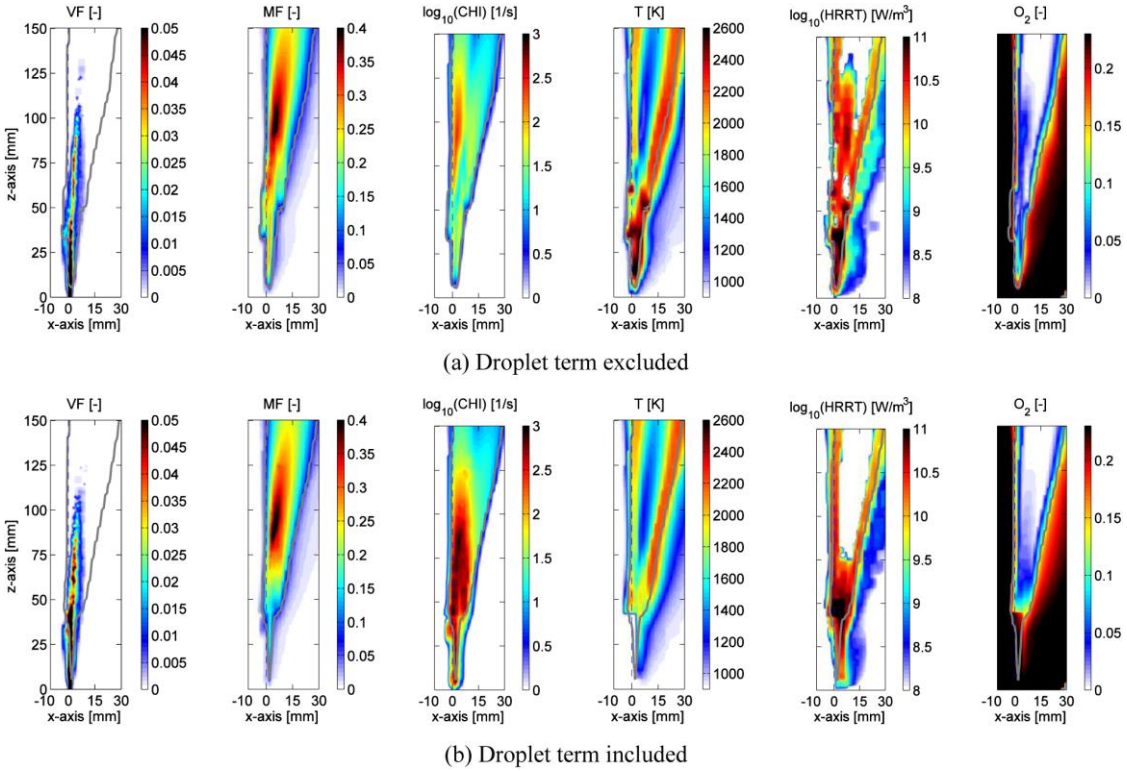


**Figure 9: Isocontours of scalar distributions 5 ms after SOI in a vertical cut-plane through the injector axis for simulation with excluded droplet term (upper) and simulation with included droplet term (lower) in the mixture fraction variance equation. From left to right: liquid void fraction, mean mixture fraction, scalar dissipation rate (logarithmic scale), temperature, OH mass fraction and heat release rate (logarithmic scale). Isolines of the stoichiometric mixture fraction $\xi_{ST}$ are superimposed in grey.**

In summary, inclusion of evaporation terms resulted in improved agreement with experimental data. These findings are contrary to previous investigations for typical automotive diesel sprays reporting only a minor influence of evaporation. Consequently, this study constitutes an extension of former analyses to large marine fuel injection configurations and emphasizes the importance of such effects particularly for the simulation of marine diesel sprays.

These results have been successfully presented/published at the SAE Powertrains, Fuels and Lubricants conference in Birmingham, UK, October 2014 [20].

## *CMC model validation for Sandia heavy-duty Diesel engine*

### Sweeps in Top Dead Centre (TDC) temperature and Start Of Injection (SOI)

Following successful application of the CMC combustion model with embedded soot model to *n-heptane* in [5], the same model has been used to study engine combustion. Validation has been performed with data from the Sandia heavy-duty optically accessible engine for a broad range of operating conditions. The findings were presented at the *SAE 11th International Conference on Engines and Vehicles* in September 2013 and chosen for inclusion in the *International Journal of Engines* [21]; a selection of results are presented in the following.

The following range of operating conditions has been studied: a sweep in start of injection (SOI) at unchanged top dead center (TDC) ambient conditions and a sweep in TDC temperature at an ambient oxygen volume fraction of 12.7 percent, corresponding to a high level of exhaust gas recirculation (EGR) as are summarised in Table 5.

**Table 5: List of test cases considered for the Sandia heavy-duty engine. Reprinted from [21]**

| Case | Speed [rpm] | $O_2$ [%-vol] | $T_{TDC}$ [K] | SOI [°CA] | DOI [°CA] |
|---|---|---|---|---|---|
| S1 | 1200 | 21 | 900 | -12 | 10 |
| S2 | 1200 | 21 | 900 | -7 | 10 |
| S3 | 1200 | 21 | 900 | -2 | 10 |
| S4 | 1200 | 21 | 900 | 3 | 10 |
| S5 | 1200 | 21 | 900 | 8 | 10 |
| S6 | 1200 | 21 | 900 | 13 | 10 |
| S7 | 1200 | 21 | 900 | 15 | 10 |
| S8 | 1200 | 21 | 900 | 15.5 | 10 |
| T1 | 1200 | 12.7 | 1000 | -5 | 10 |
| T2 | 1200 | 12.7 | 950 | -5 | 10 |
| T3 | 1200 | 12.7 | 850 | -5 | 10 |
| T4 | 1200 | 12.7 | 800 | -5 | 10 |

Ignition delays were captured very well for the SOI sweep, as can be seen in Figure 10, using unaltered model constants and kinetic parameters:

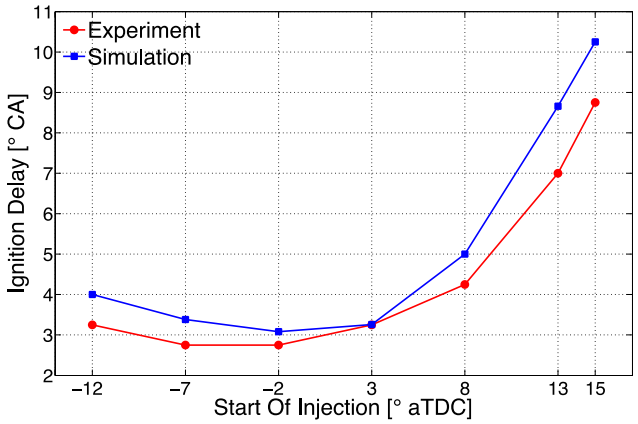


**Figure 10:** ***Ignition delay for a SOI sweep with 900 K nominal TDC temperature: experiment (red line) and simulation (blue line)*****. Reprinted from [21].**

The model was found to reproduce pressure and apparent heat release rate (AHRR) traces fairly well, although the premixed portion of combustion was in general slightly underpredicted, cf. Figure 11 and Figure 12 below.

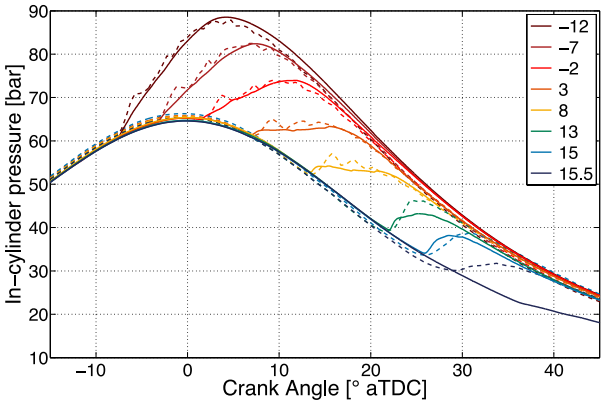


**Figure 11: In-cylinder pressure evolution for a SOI sweep with 900 K nominal TDC temperature: experiment (dashed lines) and simulation (solid lines). SOI are listed in the legend in °CA aTDC. Reprinted from [21].**

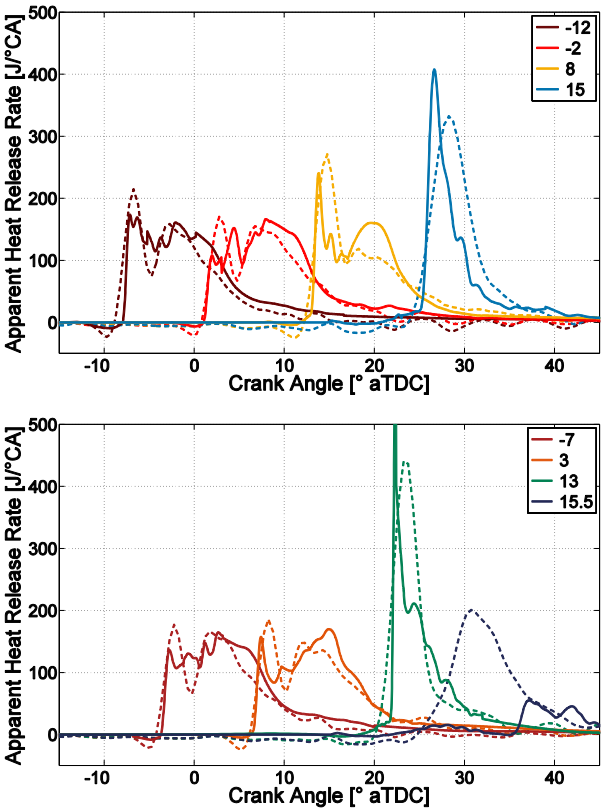


**Figure 12: AHRR evolution for a SOI sweep with 900 K nominal TDC temperature: experiment (dashed lines) and simulation (solid lines). SOI are listed in the legends in °CA aTDC; for improved readability, values are plotted alternating in the upper and lower figure. Reprinted from [21].**

Concerning emissions, a quantitative comparison of soot mass evolution is presented exemplarily for the SOI sweep in Figure 13 by means of the Spatially Integrated Natural Luminosity (SINL) in arbitrary units. Considering the broad range of conditions the model was capable to reproduce the soot trends well; the predicted peak soot mass agreed within a factor of approximately two for almost all operating conditions considered.

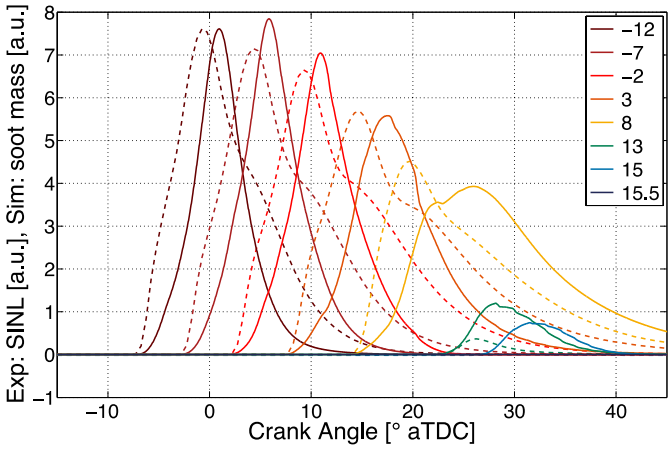


**Figure 13: Experimental SINL (dashed lines) and computed normalized soot mass evolution (solid lines) for the SOI sweep with 900 K nominal TDC temperature. SOI are listed in the legend in °CA aTDC; from [21].**

The findings were presented at the *SAE 11th International Conference on Engines* 2013 and nominated for inclusion in the *SAE International Journal of Engines* [21].

## Sandia engine: Sweeps in Exhaust Gas Recirculation Rate (EGR)

Sweeps in Exhaust Gas Recirculation Rate (EGR) have been studied for data reported in [22] from the optically accessible Sandia heavy-duty engine. The range covers from technical air (no dilution) all the way up to the misfire limit at a constant engine speed, injection timing and TDC temperature; the corresponding oxygen contents range from 21 to 8 %, cf. Table 6. As in previous studies the reduced n-heptane chemical kinetics from [18] which have seen successful application to the same engine in previous studies [23] have been employed to represent the df2 Diesel used in the experiments due to its similarity in terms of ignition characteristics; droplet thermo-physical properties have been represented by n-dodecane.

***Table 6: Engine operating conditions considered.***

| Case | Speed [RPM] | $O_2$ $[\%]_{vol}$ | $T_{TDC}$ [K] | SOI [°CA] |
|---|---|---|---|---|
| 1 | 1200 | 21 | 950 | -5 |
| 2 | 1200 | 15 | 950 | -5 |
| 3 | 1200 | 12 | 950 | -5 |
| 4 | 1200 | 10 | 950 | -5 |
| 5 | 1200 | 9 | 950 | -5 |
| 6 | 1200 | 8 | 950 | -5 |

Figure 14 displays the apparent heat release rates (AHRR) evolutions of the experiment (dashed lines) and the simulation (solid lines) for different ambient oxygen volume fractions, representing different levels of EGR. In order to facilitate readability, the curves have been deliberately split into two diagrams, displaying pairwise the predictions and measurements.

As is evident from Figure 14, the onset of combustion is significantly delayed as the oxygen volume fraction is decreased, as a direct consequence of the reduced mixture reactivity. The shorter ignition delays for the cases with lower oxidizer dilution (21, 15 and 12 % $O_2$) causes the distinct separation between premixed and diffusion burn typical for conventional diesel engines. For the lower oxygen volume fractions, the reduced mixture reactivity leads to larger ignition delays increasing the pre-combustion mixing and resulting in an almost purely premixed energy conversion. Ignition delays are well predicted by the simulation, in particular for the high oxygen contents. The larger discrepancies in

ignition delay observed for the highly diluted cases are attributed to the reduced chemical mechanism adopted.

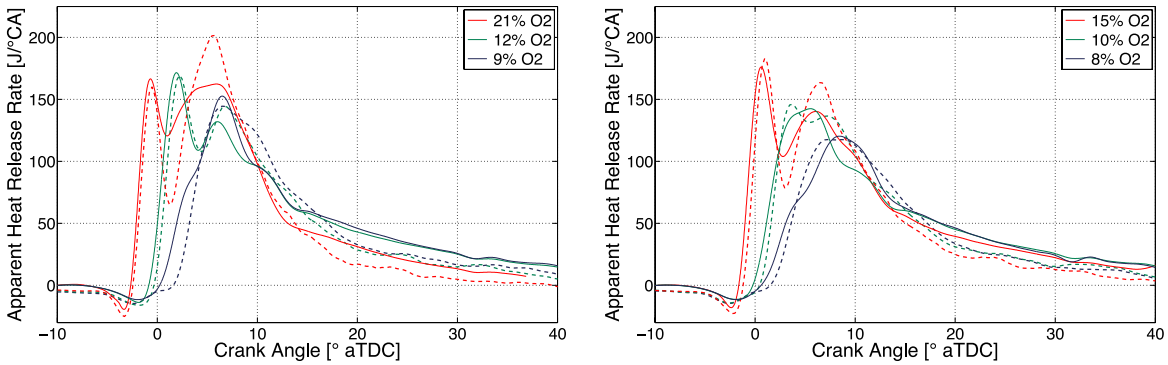


**Figure 14. AHRR evolution for an EGR sweep with 950 K nominal TDC temperature: experiment (dashed lines) and simulation (solid lines). EGRs are listed in the legend as oxygen volume fractions; for improved readability, values are plotted alternating in the left and right sub-figures.**

Figure 15 displays the measured (dashed lines) and simulated (solid lines) quantitative in-cylinder soot mass evolutions. Similarly to the AHRR traces (cf. Figure 14), soot evolutions have been split into two diagrams alternating cases to enhance graph readability. Furthermore, note that the simulation has been multiplied by a factor of two for all cases, as also labelled in the figure legend. This normalization factor has been employed for all subsequent analysis throughout the paper. Overall, the simulation is able to fairly well reproduce the trends of both peak soot mass and its timing when varying oxidizer dilution. Considering that all simulations are normalized by the same factor and that the soot peak values span a factor of about 10 between extremes, and given the semi-empirical nature of the model using only an acetylene inception the overall performance of the model is well demonstrated.

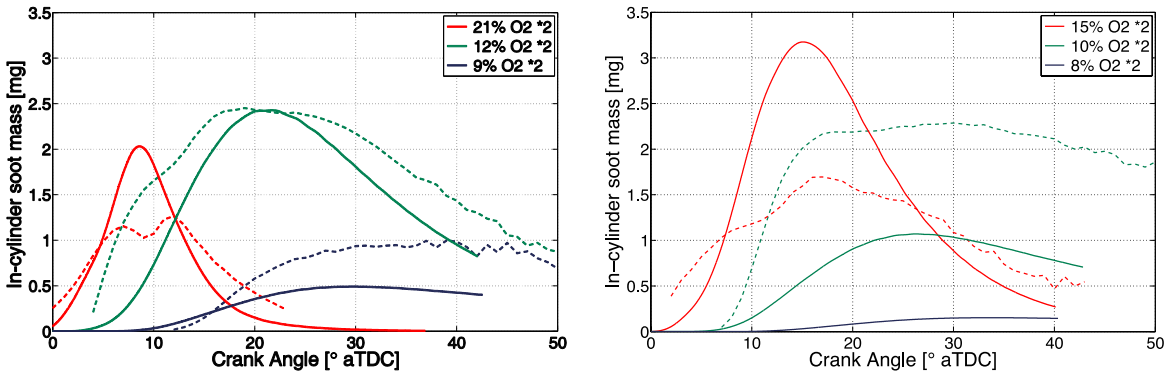


**Figure 15. Comparison of computed soot mass evolution with experimental data for different oxygen volume fractions: experiment (dashed lines) and simulation (solid lines). For improved readability, values are plotted alternating in the left and right sub-figures. Note that simulation is multiplied by a factor of two for all cases.**

These findings were published in [24], where an in-depth study of the oxygen level is further presented, separating the influence on soot formation and oxidation processes. In addition, scatterplots of temperature und flame as well as soot formation/oxidation relevant species as a function of mixture fraction are studied, revealing the impact of diminishing oxygen content on flame and soot structure.

## Post-injections in the Sandia heavy-duty Diesel engine

All Diesel engine related studies employing CMC reported in the literature so far were performed for single injection events, ranging from heavy-duty engines all the way to marine engine dimensions for a wide range of conditions, viz. pressure/temperature levels and oxygen availability. Newer engine operating concepts readily employ multiple injection events, in particular pilot injections towards reducing the pressure rate of change induced from the main injection or post injections for soot reduction. For the latter, validation has been carried out in this reporting period following substantial code development to account for multiple injections. The methodology adopted employs a re-initialization of the individual CMC cell following the appearance of mixture fraction originating from the second fuel stream. Unlike previous concepts which use conditioning on two mixture fractions, here a total mixture fraction approach is adopted which can conceptually be extended to an arbitrary number of injection events and to account for spatial transport between CMC nodes. The methodology was presented first at the International Multidimensional Engine Modelling workshop 2014 [25], prior to the SAE world congress in Detroit.

Two further studies investigating A) the impact of of injection timing using data from [26] at Low Temperature Combustion (LTC) conditions of 12.7% oxygen content as well as B) the effect of varying EGR levels in conjunction with post-injections, validated by measurements obtained in [27] were presented at the SAE Powertrains, Fuels and Lubricants meeting in Birmingham, October 2014, and accepted for publication in [28] and [29], respectively.

For the injection timing study, the main goal was to evaluate the impact of main together with post-injection scheduling on soot reduction through post-injection. Twenty-eight different cases were considered: ten different post-injections timing for command start of main injection cSOI1=-18° ATDC, ten different post-injection timing for cSOI1=-8° ATDC and eight cases for cSOI1=2° ATDC. These cases include the three cycles operated without post-injection for reference. In all cases the duration of main injection was kept constant at 16.5° CA and that of the post injection at 4.5° CA. The main operating conditions are reported in Table 7: engine speed was kept constant at 1200 RPM, with a TDC nominal motored density of about 27.7 kg/m$^3$ and an oxygen volume fraction of 12.7 %, corresponding to an EGR rate of about 55 %. The engine load range is between 9 and 10 bar gIMEP. The rail pressure was set to 1600 bar and the masses injected during main and post-injections amount to 115 and 25 mg, respectively.

***Table 7: Engine operating conditions considered in the simulations. For cSOI2 times are indicated as (from left to right) first time, interval between post-injections and the latest time.***

| **Cases** | **Speed** [RPM] | **$O_2$** [%-vol] | **$T_{TDC}$** [K] | **$P_{TDC}$** [bar] | **cSOI1** [° ATDC] | **cSOI2** [° ATDC] |
|---|---|---|---|---|---|---|
| 1-10 | 1200 | 12.7 | 914 | 74.3 | -18 | 8:4:44 |
| 11-20 | | | | | -8 | 12:4:44 |
| 21-28 | | | | | 2 | 24:4:48 |

Figure 16 provides an overview of the good predictive capabilities w.r.t. heat release rate for 14 of the 28 cases studied. The impact on in-cylinder soot evolutions was further examined for a selection of cases. The numerical model enables deep insights into to driving mechanisms since the soot formation and oxidation from the individual injection events can readily be separated which is experimentally very challenging. It was found that oxidation of main soot cloud is enhanced by post-injection, due to mixing increased by the high velocities of the post-spray. In particular, the combination of increased velocities and turbulence, even if with low intensity and only locally, increases the probability that particles of soot and molecules of oxygen and OH radicals encounter; this is fundamental for the oxidation of soot at LTC conditions, where oxygen is scarce. The findings suggest that in cylinder soot reduction by post-injection

at LTC conditions is dictated by 1) increased soot oxidation due to the post injection and, 2) more importantly, low additional soot production by the post injection due to the “non-sooting conditions” in the combustion chamber at the time of post injection, especially for larger dwell times.

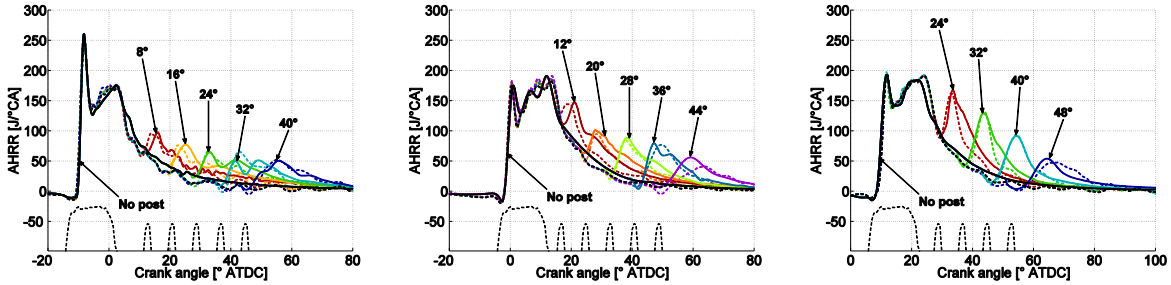


***Figure 16: Apparent heat release rate for three start of main injection: -18° (left), -8° (middle) and 2° ATDC (right). Experiment dashed and simulation solid lines. Injection rate profiles are indicated below by the black dotted lines.***

Concerning the EGR influence in the presence of post-injections, data from the experimental dataset reported in [27] has been modelled. Eight cases have been considered for this study: four levels of EGR resulting in initial ambient oxygen concentrations of 21, 18, 15 and 12.6%, each with and without a post-injection. The main injection is the same as the single injection; the post-injection therefore adds more fuel mass to the combustion. The cases are summarised in Table 8:

***Table 8. Operating conditions considered for simulation.***

| | |
|---|---|
| Engine speed | 1200 RPM |
| TDC temperature, motored | 900 K |
| Ambient oxygen volume fraction | 12.6%, 15%, 18%, 21% |
| Injection configuration | Main only, Main + post |
| Injection durations | Main 1950 µs, post 500 µs |
| Commanded start of injection (main) | 347° |
| Commanded start of injection (post) | 366° |

Figure 17 presents the validation of the heat release rate predictions. For the main injection cases, an excellent agreement for the 21% $O_2$ is observed for the AHRR evolution, with both the premixed as well as diffusion combustion modes being captured very well.

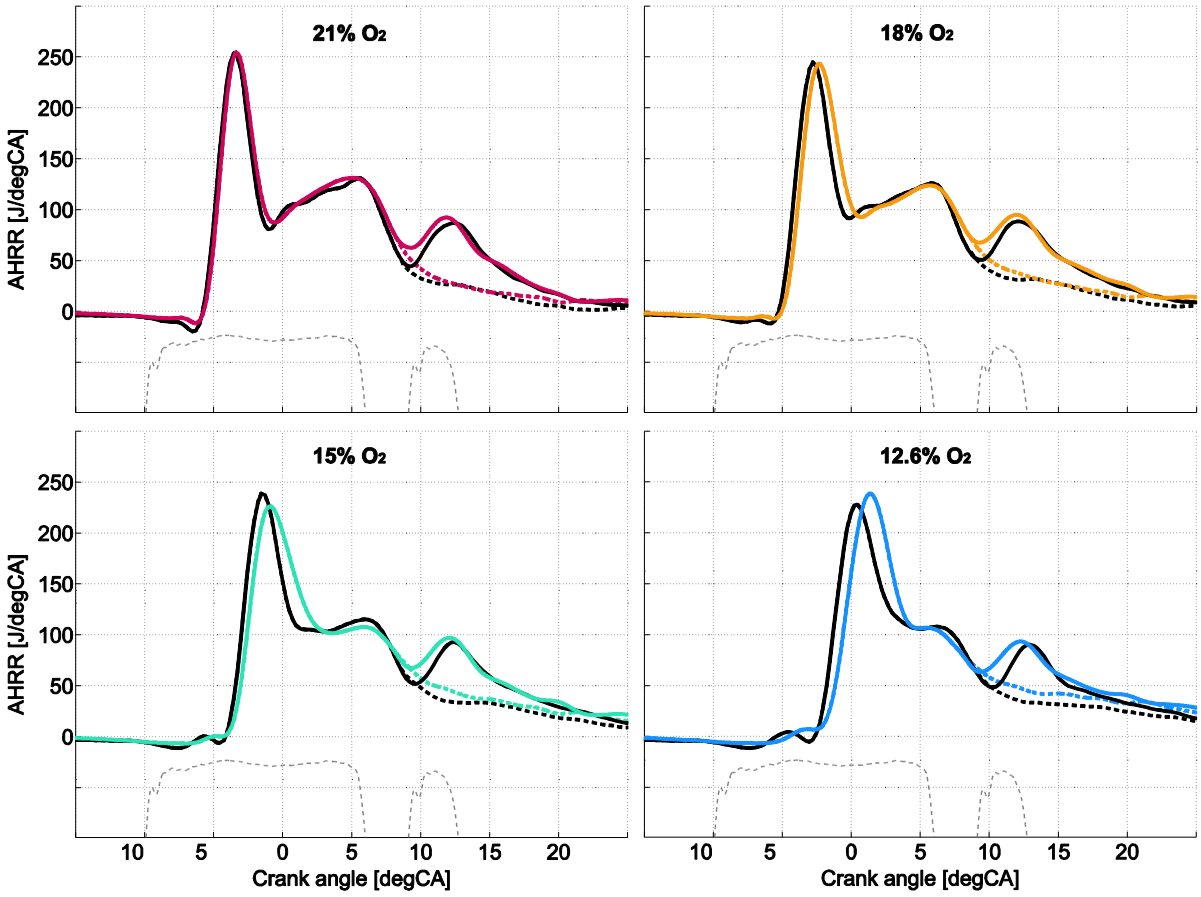


***Figure 17. Validation of apparent heat release rate (AHRR) for varying degrees of EGR: Black lines: experimental AHRR curves; coloured lines: simulation AHRR curves for the respective EGR level. Dotted lines represent single-injection cases while solid lines represent cases with post-injection. Injection rate profiles are drawn in dashed lines below the AHRR profiles.***

Model predictions gradually worsen for increasing oxidiser levels, maintaining however good accuracy considering the large spread in dilution considered. In the measurement, as expected, the peak of the premixed combustion mode decreases monotonically with dilution due to the lowered mixture reactivity. The simulation reproduces the correct trend except for the lowest oxygen (12.6%) where the premixed peak becomes higher. This is attributed to the slight over-prediction of the ignition delay in this case due to limitations of the chemical mechanism at less reactive conditions. For the post-injection cases, from the experimental AHRR it is observed that the EGR level has a minimal influence on the ignition delay of the second injection except for the 12.6% $O_2$ case. The increase of AHRR induced by the post-injection is also comparable along different ambient dilutions. Concerning the simulation it is first important to note that the effect of the post-injection on the AHRR is the difference between AHRR with and without post-injection. At the time of start of post-injection the simulation overestimates the AHRR for the case with main injection only. This offset is reflected in the AHRR with post-injection. For all cases apart from the 12.6% $O_2$ the time when the AHRR curves with and without post separate is consistent with the experimental observation. The same applies for the AHRR magnitude as well as the timing of the peak. On the contrary, for the 12.6% $O_2$ case the simulation shows a faster ignition and conversion of the post fuel.

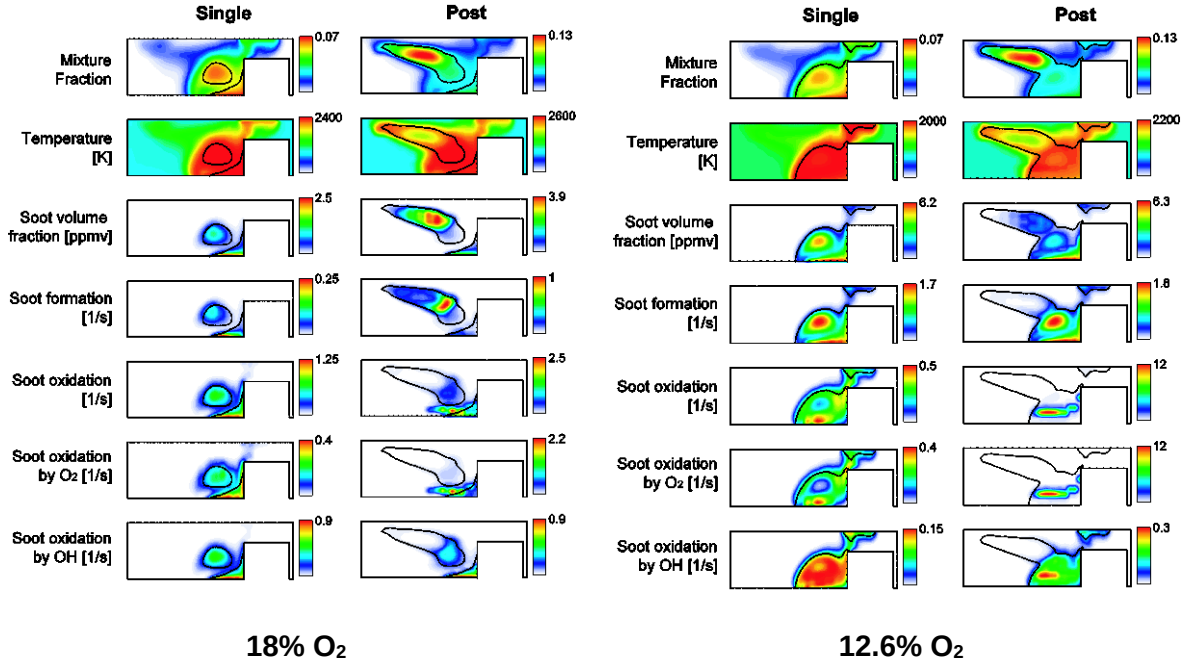


***Figure 18. Contours of selected fields at 13° CA (corresponding to the time instant of interaction between the post and main injection) on a vertical slice through the injector axis for the case with 18% oxygen (left sub-figure) and 12.6% oxygen (right sub-figure). Left columns denote single injection events, right columns with post-injection. The minimum for all colour scales is zero.***

Contours of important soot-relevant quantities are examined in Figure 18 for the cases with 18% (left) and 12.6% $O_2$ (right). Quantities from top to bottom are: total mixture fraction, temperature, soot volume fraction, total soot formation rate, total soot oxidation rate and distinct soot oxidation rate by oxygen and OH. Distributions are drawn at 13° CA, when contact between post- and main-injection regions takes place. To enable a quantitative comparison, the quantities are plotted with their respective local minima and maxima. For the 18% $O_2$ case, the oxidation rate almost doubles following a large increase in the contribution of oxidation caused by $O_2$. While the soot formation rate maximum in the post-injection case increases roughly to four times that of the single injection (due to the added fuel), the oxidation rate due to $O_2$ increases to five times. However the OH-oxidation rate is unchanged, limiting the overall oxidation rate increase to a factor of two, since the OH-contribution is much more significant at this low EGR. More importantly, the increased $O_2$ driven oxidation shows a localised character, appearing slightly downstream of the maximum relative oxygen enhancement location. These observations are similarly investigated at the high-EGR level in the lower half of the same figure. Here, the soot oxidation rate due to $O_2$ increases by over an order of magnitude due to the post-injection. OH-oxidation offers a much smaller contribution to the total oxidation, relative to the reference case discussed previously. The OH-oxidation rate is also locally enhanced in a small region, but overall the oxidation rate increases mainly due to $O_2$ contribution and reaches the same order of enhancement. As before, the spots of soot oxidation by $O_2$ are highly localised. At this EGR level, the soot formation rate is strongly suppressed so that any increase from the post-injection is marginal, and the change in the overall soot volume fraction is minor. This strong inhibition of the formation rate is in agreement with the findings of [24] at a similar level of ambient $O_2$. It is observed that at low $O_2$ levels (high-EGR case), the $O_2$-oxidation plays a higher role in the overall oxidation, whereas OH-oxidation is predominant at high $O_2$-levels (reference case) due to the high temperature, and correspondingly high OH levels.

As discussed in further detail in [29], the local oxidation and formation rates for the post-injection case were found to show ‘spotty’ regions of surge due to mixing of the post jet with the pre-existing soot from the main injection. The surge in oxidation rate, which is caused by additional momentum imparted by the jet to the immediate vicinity, and the consequent entrainment of oxygen, can overwhelm the additional formation rate which results from the small further enrichment (at the head of the post-jet) of

the already fuel-rich regions present from the main injection. This results in faster oxidation, specifically $O_2$-oxidation, compared to the baseline single-injection case, especially at high EGR. At the time of main- and post-jet interaction, it can be seen that the contribution of $O_2$-oxidation towards the total oxidation rate remarkably increases with the addition of the post-injection, and that it occurs in spots of high intensity. Overall, the proposed extended CMC model along with integrated soot modelling appears to be a very promising framework for the study of close-coupled post-injection soot dynamics.

These findings were presented at the SAE Powertrains, Fuels and Lubricants meeting in Birmingham, UK, October 2014, and accepted for publication in [28] and [29], the latter of which was nominated for inclusion in the *SAE International Journal of Engines*.

## Influence of dwell time and injection duration on soot-reduction effectiveness of post-injections

This validated model was subsequently used as a basis to conduct a series of numerical experiments for extended operating conditions, although no validation data is available at present. The investigation comprises three different start-of-injection timings (-15°, -10° and -5° CA, all ending at +5° CA aTDC) each performed at two different background oxygen contents (12% and 18%). To each of these six conditions, a corresponding case with a post injection is added. Further, for one of the conditions (15° DOI) a sweep in post injection dwell (2°, 4°, 6°) has been applied. Results are first presented for different main injections with a constant post injection, followed by results for a constant main injection with different post injections.

Figure 19 shows three operating conditions (three different durations of main injection) at (a) 18% and (b) 12% background oxygen, as well as the single-injection case. The figure top left shows the spatially integrated soot mass over time, the top right the formation rate, the bottom left the oxidation rate by oxygen and the bottom right the oxidation rate by the hydroxyl radical (OH). Formation and oxidation rates are normalized by the soot mass (existing in the cylinder at the corresponding time) and thus have the unit of inverse time only. Solid lines indicate the cases without post injection while dashed lines indicate cases where a post-injection is added. Common to both ambient oxygen conditions displayed, the post injection enhances the oxidation rate by $O_2$, visible as a rapid and short surge in the bottom left figure. The accelerated $O_2$-oxidation is brought about by incoming fresh oxygen forced in by the post-jet momentum, in agreement with conclusions also reached in [29]. The overall soot mass (top left) increases as expected for longer injection duration due to the higher mass of fuel from the main injection.

The analysis of the heat release rates (not shown) reveals that the portion of energy converted in premixed mode remains roughly the same (with small differences due to different pressure and temperature levels at SOI), therefore longer injection durations lead to increased conversion in a diffusion controlled combustion mode. With earlier onset of soot, sustained combustion allows the formation (top right) and oxidation (bottom) rates of main injection soot to have a higher peak. From the soot mass evolution, a phase of dominant formation can be recognized until the time of reaching peak soot mass, followed by a period of dominant oxidation.

At 18% ambient oxygen, for the post-injection soot, the peaks of formation and OH-oxidation rates are largely similar across the cases shown. With lower reactivity at 12% $O_2$, the overall soot mass evolution is considerably retarded in time compared to the 18% $O_2$. Unlike the latter where the effect of post-injection on the soot formation rate begins in the already oxidation-dominated phase, here – due to the delayed soot mass evolution and the unchanged post-injection timing – the effect of post-injection is seen comparatively earlier, when the evolution is formation-dominated. In this situation, the effect of the post-injection is to boost the formation rate further, due to enrichment of the existing soot from the main injection.

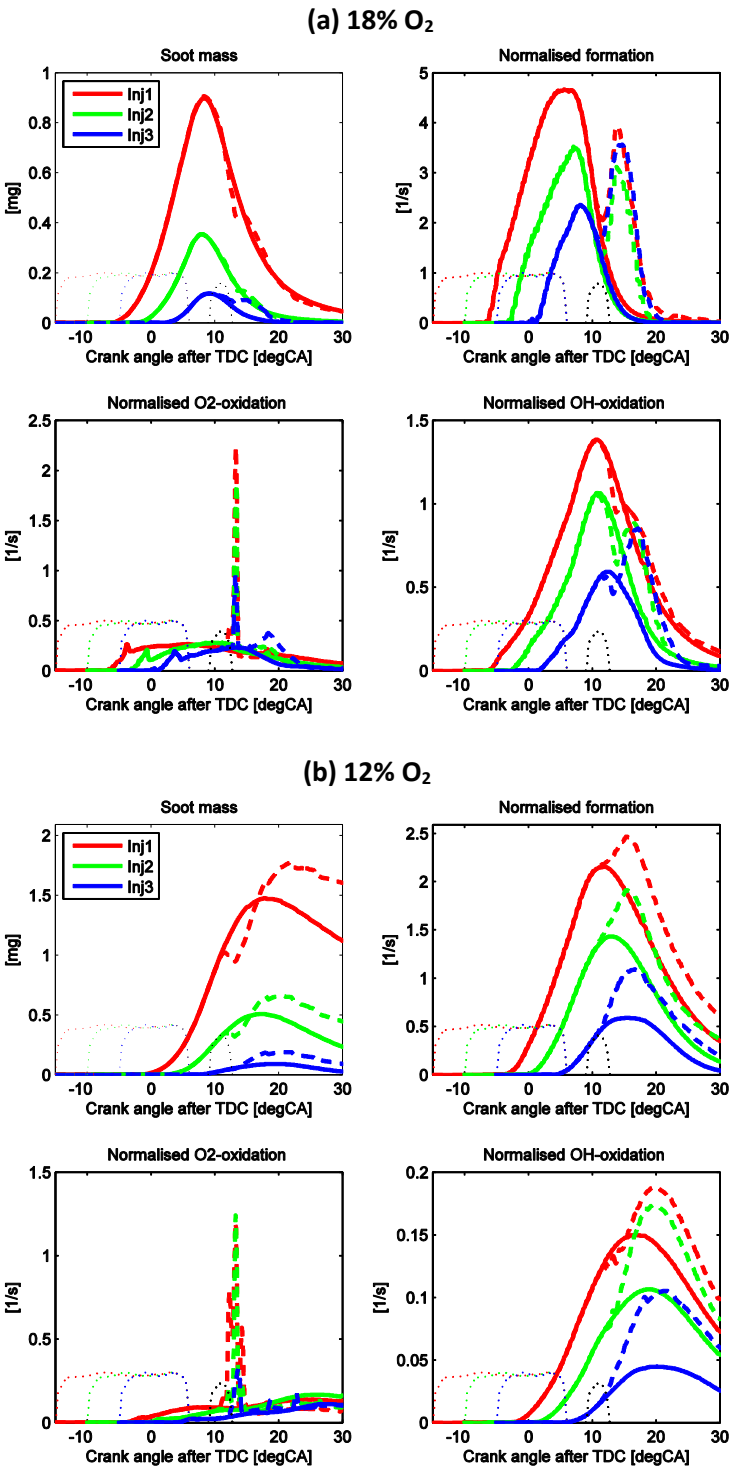


**Figure 19: Soot quantities at 18% (a) and 12% (b) ambient $O_2$. Top left: soot mass, top right: soot formation rate, bottom left: oxidation by $O_2$, bottom right: oxidation by OH. Solid lines: single-injection case, dotted lines: case with post-injection. Three different main injections are presented, injection rates are drawn in dotted lines.**

In the 12% $O_2$ case, the surge in the $O_2$ oxidation rate is quite similar in magnitude to that of the 18% $O_2$ case, differing at most by a factor of two. However, the OH-oxidation is considerably diminished – by an order of magnitude – at the lower oxygen level due to reduction of the flame temperature and thus OH radicals. The contribution of $O_2$ to the overall oxidation is thus higher when ambient $O_2$ content is lower [28, 29], though it must be noted that the total oxidation rate is lower due to the large drop in OH oxidation. Additionally, heat-release rates (not shown for brevity) indicate that the enrichment of the existing main-injection mixture described in the previous paragraph is in fact favourable for accelerating

the combustion that would otherwise have been too lean. This also explains the larger OH oxidation peak of a post-injection case compared to its corresponding single-injection case, for the 12% $O_2$ condition.

From Figure 19 it may be concluded that the overall effectiveness of the post-injection depends upon the time of interaction relative to the soot mass peak for a given operating condition. For lower ambient $O_2$ where the time of contact is before the soot peak, the growing formation rate is enhanced not only by the additional fuel but also by enrichment of existing main-injection rich zones, while any boost in oxidation is overwhelmed after it provides a short and minor decrease in the soot mass. For higher ambient $O_2$ where the time of interaction is later than the soot peak, there is a lack of rich zones by this time to provide for an increase in soot from the main injection due to extra formation by enrichment. Instead, additional formation stems only from the post-injection fuel itself as an almost independent event, and the major effect of the post-injection interaction is the acceleration of $O_2$ oxidation in an already ongoing oxidation phase. This is further significantly assisted by higher OH concentration and thus OH-oxidation, in particular for the shorter injection durations.

In an attempt to decouple the variation in main/post interaction timing from variation in ambient oxygen level, different post-injection dwells are considered while keeping a constant ambient $O_2$. This sweep of three different start-of-post- injections (SOI2) following a constant main injection highlights the trends of soot formation and oxidation rates for different interaction times but the same overall reactivity. Figure 20 shows three operating conditions (three different SOI2s) at (a) 18% and (b) 12% background oxygen, together with the single-injection case (black solid line) as a reference. Similar to the previous discussion, the figure top left shows the spatially integrated soot mass over time, the top right the formation rate, the bottom left the oxidation rate by oxygen and the bottom right the oxidation rate by the hydroxyl radical (OH). Formation and oxidation rates are normalized by the soot mass and thus have the unit of inverse time only. For the higher ambient $O_2$ case (a), all three SOI2s result in interaction with the main soot after the soot mass peak is achieved: in the oxidation-dominant phase. For the close-coupled post injection event, the effectiveness of oxidation improvement is comparatively low, and the soot mass at the end of 30° CA is higher than the single- injection soot mass, unlike the mid- and far-post injections. The effectiveness hence deteriorates with decreasing dwell time.

For the lower ambient $O_2$ case (b), interaction of all three SOI2s with the main-injection soot happens before the soot mass peak, in the formation dominant phase. The earlier the post-injection interaction, the higher the enrichment of the main- injection rich region leading to an increase in formation rate. Additional soot is therefore formed not only due to the post-injection itself but also due to this interaction enriching the main soot cloud due to temporal proximity. Further plagued by the lack of any significant OH-oxidation at low ambient oxygen levels, the overall soot mass can increase considerably in the presence of post-injection where the dwell time is short. It is also seen that for the three different SOI2 considered, a spike in $O_2$ oxidation rate – although different in peak magnitude – is present at a very similar time around 13° aTDC. This is a geometrical effect of having hit the cylinder wall (as discussed in [29]) after which the oxidation rate drops, and is therefore not an easily generalizable observation.

The oxygen forced in the main soot cloud due to post-jet momentum – the driving agent for the $O_2$-oxidation rate surge – can be represented as a relative $O_2$ distribution (i.e. difference of $O_2$ spatial distribution in the post-injection and main-injection case, normalized by that of the main-injection case). This is shown in Figure 21 illustratively for the mid-dwell post-injection. A relative $O_2$ of zero indicates equal local oxygen between post-and main cases and can be seen e.g. in areas far from the flame, before the post- injection has caused any influence. Inside the post- injection envelope, the limit of relative $O_2$ is -100%, indicating that all of the oxygen otherwise present in the single-injection case has been consumed in the post-injection case. Values above zero indicate that the post-injection causes a local increase in the oxygen content by forced transport due to its momentum. In the 18% $O_2$ $O_2$ case, a blob of nearly +160% more $O_2$ is seen being pushed into the main soot cloud. For the 12% $O_2$ case the relative increase is clipped to +300% in the figure, although actual values reach +2500%. A very early (extremely close-coupled) post-injection is ineffective from this point of view since there is little to

no spatial separation – and thus no intermediate region of oxygen which can be forced into the main soot cloud.

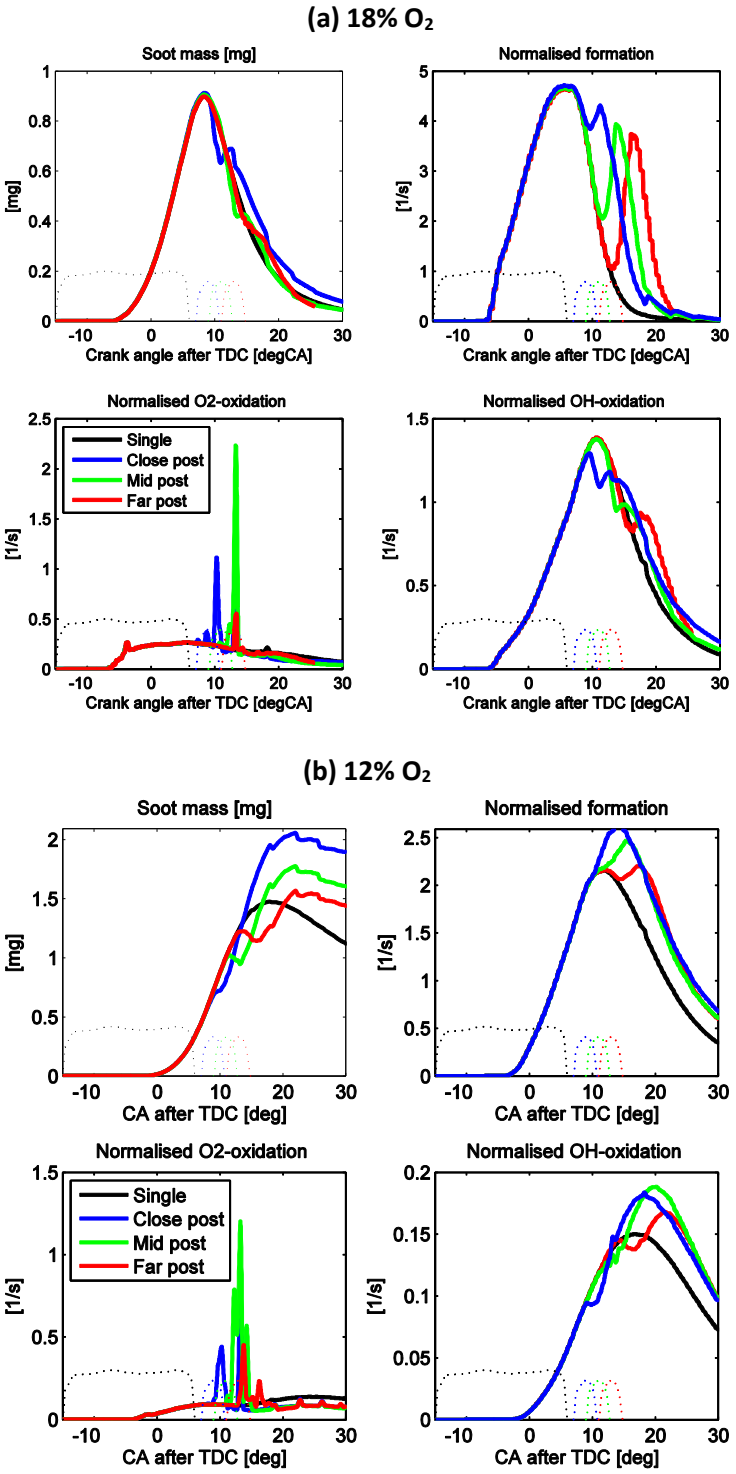


**Figure 20: Soot quantities at 18% (a) and 12% (b) ambient $O_2$. Top left: soot mass, top right: soot formation rate, bottom left: oxidation by $O_2$, bottom right: oxidation by OH. Three different post-injection dwells are presented, injection rates are drawn in dotted lines with the same colour of the corresponding dwell case.**

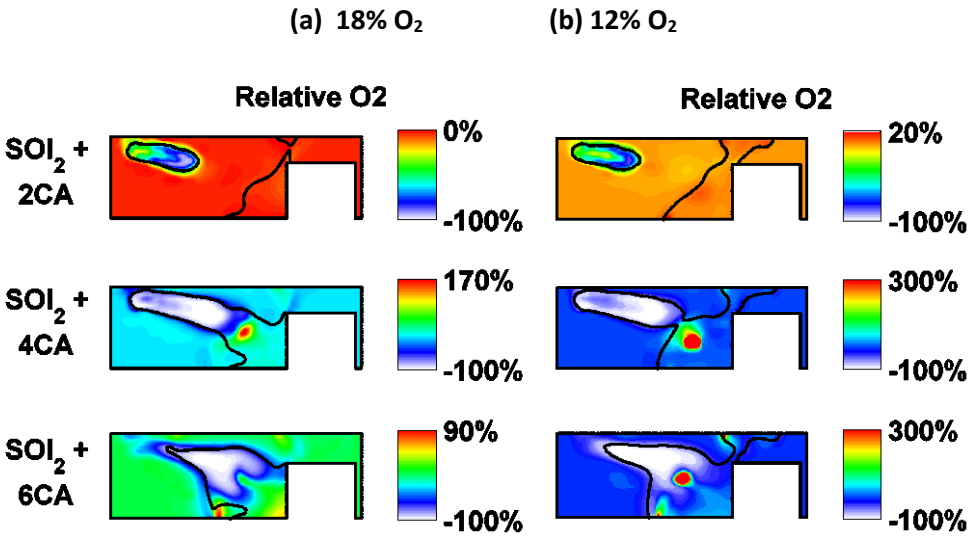


**Figure 21: Relative $O_2$ distribution in a side-view of the engine combustion volume. (a) 18% and (b) 12% ambient $O_2$ content.**

In summary, the use of CFD-CMC simulations provides considerable insight into soot formation processes: effectiveness of a post-injection requires a fluid-mechanical interaction, and depends on the time of interaction relative to the time of soot mass peak for a given operating condition. Higher ambient oxygen levels result in higher oxidation rates overall: $O_2$ oxidation is higher by factor of 2, but OH oxidation is higher by order of magnitude, being thus more significant. Shorter dwells are less effective, due to absence of spatial separation and consequent lack of a region of intermediate oxygen, to force into an existing main-injection soot cloud.

The findings were accepted for presentation at the *SAE 12th International Conference on Engines* in September 2015 and published in [30].

### *Soot precursor sensitivity analysis*

No clear consensus exists in the literature as to whether using acetylene as the unique precursor species for soot modelling is sufficient at diesel engine relevant conditions. A variety of other species have also been proposed, in particular polycyclic aromatic hydrocarbons (PAH), namely naphthalene (A2), phenanthrene (A3) and pyrene (A4). Various studies for Diesel engines and sprays can be found which use acetylene alone or in combination with one of these PAH species. To gain understanding concerning the conditional distributions of these four species in conserved scalar space, stand-alone CMC calculations have been performed using an n-heptane chemistry [31] which includes PAH precursors up to A4.

The normalised conditional mass fractions shown in Figure 22 reveal that for this specific kinetic mechanism, the different potential soot precursors qualitatively show similar distributions. I.e. the peak values are located at rich conditions, at roughly twice the stoichiometric mixture fraction for A1, A3, A4, and roughly three times $\xi_{ST}$ for $C_2H_2$ and A2. These results suggest that any of these species may be used as a precursor, provided the soot model constants are adjusted accordingly. A comparison presented in [14], where different combustion and soot models with various precursors were employed for “Spray A” from the Engine Combustion Network support these findings, i.e. comparable soot predictions can be achieved using different precursors and the differences arising due to different combustion models may be more dominant than the choice of the soot precursor. Nonetheless, future studies are needed to assess the impact of soot precursor choice on A) distributions of conditional soot mass fraction and conditional soot number density using stand-alone calculations and, B) the spatial distributions of soot for autoigniting sprays over wide ranges of conditions, i.e. temperature, density and oxygen content as well as injection strategies for different fuel types.

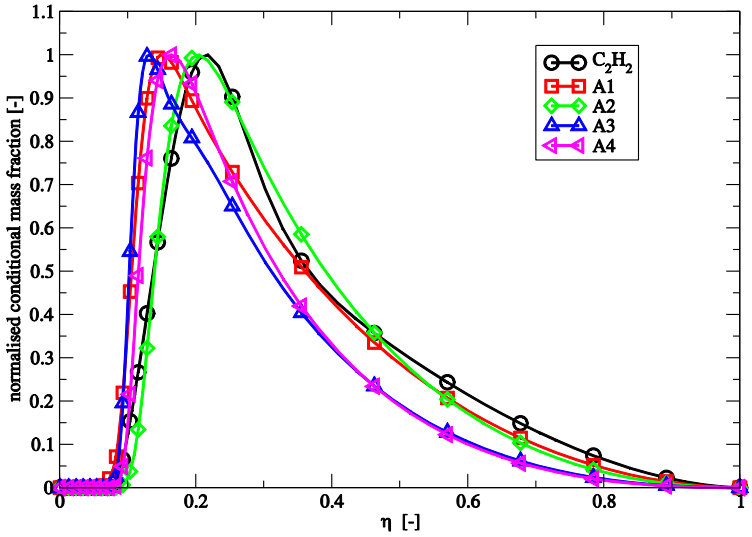


**Figure 22: Comparison of various conditional soot precursors after 5 ms for an auto igniting flamelet calculation at Sandia spray H conditions with $T_{air}$ = 1000 K (21% $O_2$), $T_{fuel}$=373 K, pressure = 42.5 bar and conditional scalar dissipation rate <N|η=0.5>=25 $s^{-1}$ using the chemical kinetics from [31]. The peak values have been normalised to one for comparison (factors are 5.342e-2, 3.952e-3, 1.175e-3, 2.144e-4 and 6.844e-4 for $C_2H_2$ and A1 to A4, respectively).**

# Model development for biogenic and synthetic fuels (WP2)

In terms of synthetic fuels, the long-chain ***n-dodecane*** has been selected as a representative **XTL fuel**. The main motivation is the emergence of a vast database in the context of the Engine Combustion Network (ECN). This further enables focussing on the remaining biogenic fuels in the experimental campaign, cf. **WP4**.

Three classes of oxygenated fuels, namely ***alcohols, ethers*** and ***esters***, are therefore proposed for investigation both numerically and experimentally in the remainder of this project. For the alcohol, the choice is an *n-heptane*/*n-butanol* blend, motivated by synergies with the Swiss Federal Office of Energy project "Kraftstoffkennzahlen II" [32], where different different ***n-heptane/n-butanol blends*** are investigated under Homogeneous Charge Compression Ignition conditions using detailed chemical kinetics. Here, the focus is on spray auto-ignition and only the blend with 9.1 percent *n-butanol* by volume is investigated due to its cetane number (CN) of roughly 55, similar to Diesel fuel. Furthermore, kinetics are readily available which have already seen application in the IC engine context, using however alternative combustion models [33]. Preliminary calculations for auto-igniting flamelets at different strain rates have therefore been carried out as discussed below.

From lipid sources such as rape seed, soy bean or palm oil, long-chain fatty acid methyl esters (FAME) can be procured. The chain length is in the range of 20 C-atoms, leading to very large detailed chemical kinetics which are presently intractable in the 3D-CRFD context. To study nonetheless the impact of methyl ***ester*** groups on combustion, ***methyl decanoate (MD)*** constitutes a promising ***surrogate***, for which a reduced and a skeletal chemical kinetic mechanism have been identified (77 species/209 reactions [34] and 115 species/460 reactions [35], respectively); developed based on the detailed kinetics proposed by LLNL with roughly 3,300 species and close to eleven thousand reactions [36]. In addition to the skeletal and reduced chemical kinetics, thermochemical properties of the liquid (density, viscosity, surface tension, vapour pressure, latent heat, heat capacity and conductivity as functions of temperature), have further been identified and implemented in the CFD code.

Concerning ethers, ***dimethyl ether*** (DME) presents an interesting candidate due to the cetane number of roughly 55 and the availability of chemical kinetics with various degrees of detail. Preliminary measurements were carried out in the HTDZ, however using a multi-stream injector and reporting the necessity to maintaining the fuel return line at elevated pressure due to the low boiling temperature. Due to these difficulties, experiments were carried out for two different ***oxy-methyl ether*** (OME) blends using single-orifice measurements cf. **WP4** below. On the numerical side, the availability of chemical kinetics as well as difficulties in procuring thermophyiscal droplet properties however continue to present a substantial challenge for both DME as well as OME.

### *n-dodecane*

### Chemical mechanism testing

To model XTL fuels with cetane numbers of roughly 70, *n-dodecane* has been used as a surrogate on the one hand due to the well-known thermo-physical properties (needed for spray calculations) and secondly due to the existence of chemical kinetics mechanisms (most often developed by means of shock-tube data).

In a first step, two different *n-dodecane* chemistries, namely the one from Luo et al. [37] and the one from Narayanaswamy et al. [38] have been tested using a perfectly stirred reactor configuration by means of the SENKIN/CHEMKIN package. Validation is performed with shock tube data from Vasu et al. [39] for a range of temperatures at two equivalence ratios at a single pressure of 20 bar.

As can be seen in Figure 23, considerable differences exist between the two mechanisms. At the lower and intermediate temperatures, the Luo et al. chemistry predictions show better agreement with the measured data, while at high temperature, the mechanism from Narayanaswamy et al. reproduces more accurately the experimental values. Since spray autoignition in engines usually occurs at the lower to intermediate temperature range, the mechanism of Luo et al. [37] has been chosen to carry out further studies. With 106 species and 420 reactions this mechanism is also considerably smaller and hence computationally more affordable, compared to 255 species and 1,509 reactions the Narayanaswamy et al.

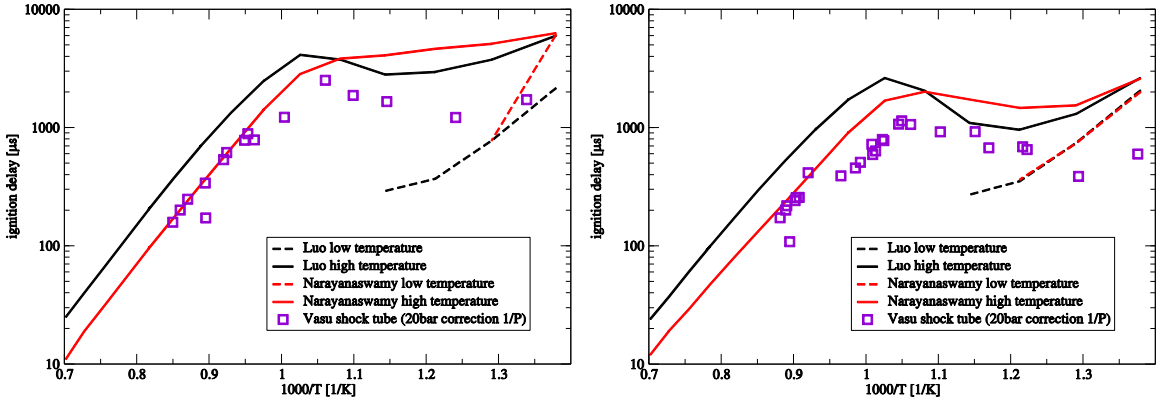


**Figure 23: comparison of predicted ignition delays from two different chemical kinetic mechanisms to shock tube data [39] for a range of temperatures. Pressure 20 bar, equivalence ratio 0.5 (left) and 1.0 (right)**

### Time-resolved soot investigations on *n-dodecane* "Spray A"

Following previous investigations on soot formation in the Sandia constant-volume combustion chamber where quasi-steady soot profiles were studied for an extensive operating range relevant to diesel combustion for both *n-heptane* [5] and n-dodecane, the present study focuses on transient evolution of soot. Past data available from the engine combustion network (ECN) was limited to the quasi-steady

period, however the availability of new data with n-dodecane allows time-resolved investigation of soot-relevant processes as also reported in [40] .

The reference case for this study corresponds to 900 K ambient temperature and 15% ambient $O_2$ by volume. Further, parametric variations are considered in temperature and ambient oxygen as summarized in Table 9. For all cases, n-dodecane is injected into a constant-volume combustion chamber at 6 MPa pressure (leading to a density of 22.8 kg/m$^3$). The actual injection duration is 6.0 ms.

**Table 9. Nominal ambient experimental conditions used in this study.**

| **Temperature** | **[K]** | 850 | 900 | 1000 | 1100 | 1200 |
|---|---|---|---|---|---|---|
| **Ambient $O_2$** | **[vol%]** | 15 | 13/15/21 | 15 | 15 | 15 |

***Soot mass evolution***

Figure 24 shows the temporal evolution of total soot mass for different ambient oxygen concentrations (left) and temperatures (right). Solid lines show the soot mass from simulation while measurements are denoted by dotted lines. The reference case (900K, 15% $O_2$) is shown in green in both plots.

For the reference case, measured soot onset time is at 0.73 ms with a subsequent strong increase of the soot mass culminating into a soot bump at around 1.8 ms and later the total soot mass stabilizes at approximately 15 µg. The effect of a change in ambient oxygen on the soot mass during the quasi-steady state period is relatively insignificant, despite a change in the soot onset time due to changed reactivity. On the other hand, increasing ambient temperature results in strongly increased quasi-steady soot mass, owing to the strong temperature dependence of the formation rate. For all cases, a first soot peak and a subsequent quasi-steady plateau are observed. The simulation shows the qualitative trends very well and provides an order-of-magnitude-accurate quantitative prediction.

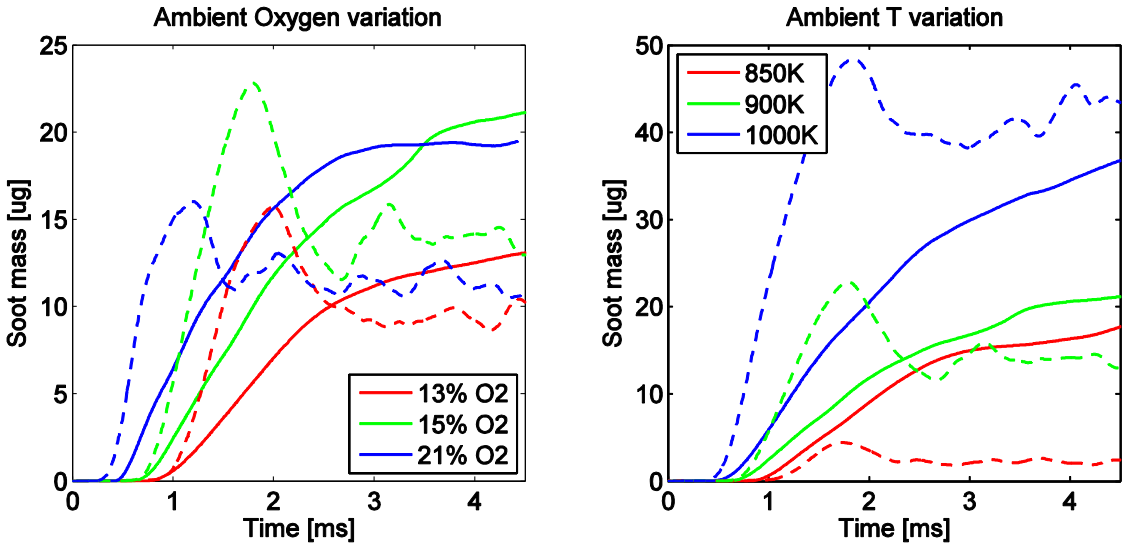


**Figure 24. Evolution of total soot mass from simulation (solid) compared to experiment (dashed) for different conditions: 13, 15, 21% $O_2$ (left); 850, 900, 1000 K (right).**

### *Soot spatial distribution*

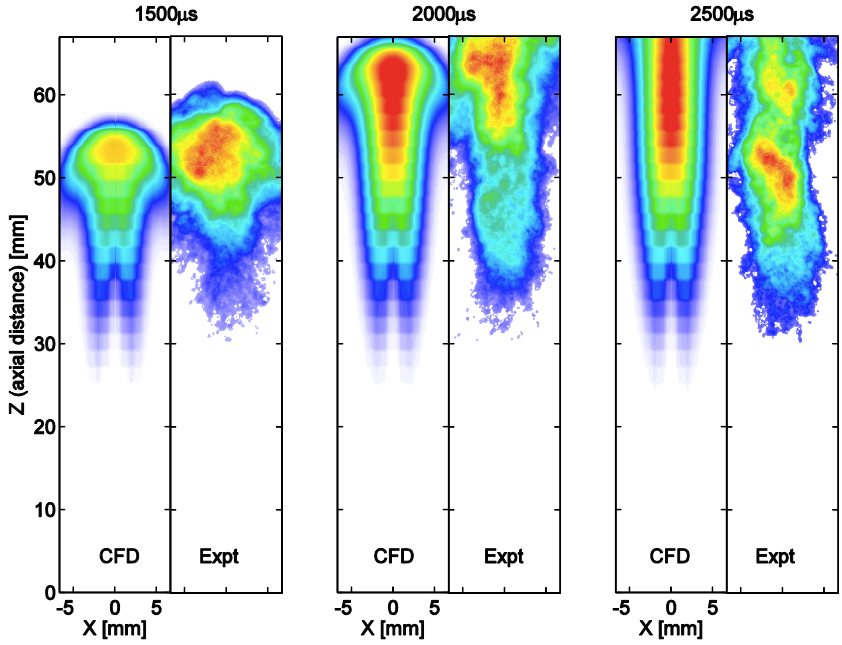


**Figure 25. Comparison of soot volume fraction (from CFD) with measured kL distribution. The quantities are normalised for a qualitative comparison and colour palettes are identical across the time instants shown.**

Figure 25 shows a comparison of the spatial distribution of the simulated soot volume fraction (SVF) region with the ensemble-averaged optical thickness (KL) from experimental data at three different time instants (1500, 2000 and 2500 µs) for the long injection duration (6000 µs). The simulation agrees well with experiment not only with respect to the soot cloud penetration, but also with respect to extent in both axial and radial coordinates. The tail of the predicted soot cloud also stabilizes in agreement with the experiment, and the evolution of the SVF core location agrees well overall with the KL distribution. While the good agreement of soot distribution in space is partly a consequence of correct jet penetration and good prediction of combustion characteristics (since these precede soot processes in the chain-of-events), validation of the evolving soot region in this study provides additional credit to the employed model and enables its use for extracting further insight into the underlying physical phenomena.

### *Soot onset and latency*

Figure 26 shows the comparison of soot onset as well as auto-ignition from simulation and experiment, and emphasizes the latency between ignition and the beginning of soot formation. The upper and lower rows in the figure show the comparison for different oxygen levels and different temperatures respectively. Values from the experiment are shown using dotted lines, and those from simulation are shown as solid lines. Blue lines denote the latency (i.e. the difference) between the ignition time/location and that of soot onset. Circular markers show ignition and squares show soot onset, while triangles show the difference.

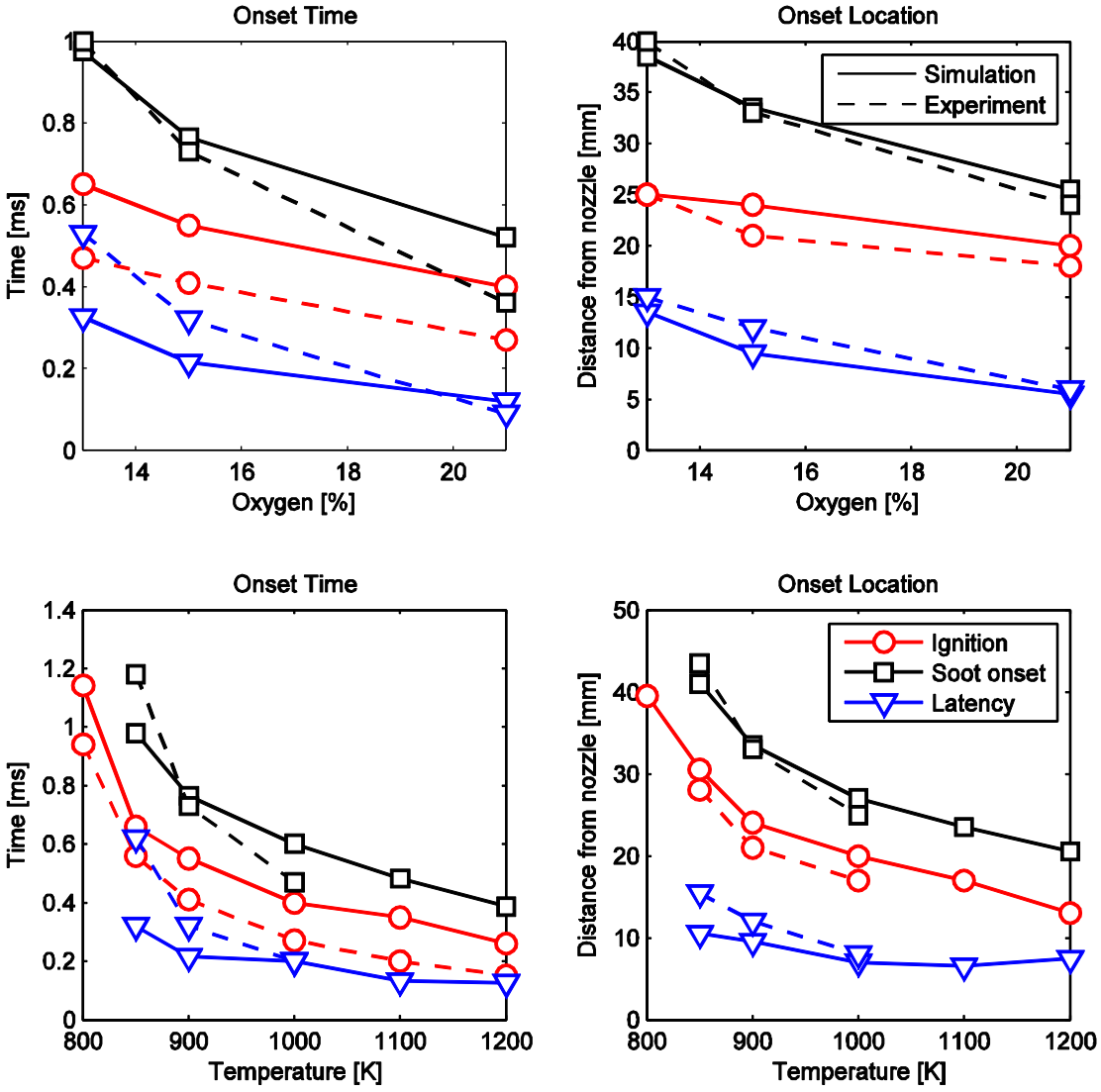


**Figure 26. Soot indicators for a variation in ambient oxygen (top) and temperature (bottom). Columns from left to right show soot onset time and soot onset location. Dotted lines: experiment; solid lines: simulation. Circles: ignition, squares: soot onset, triangles: latency.**

Ignition delays are defined as the time difference from start of injection until high-temperature ignition and combustion, indicated by luminosity reaching 50% of steady high-temperature chemiluminescence. The strong exponential influence of ambient temperature on the chemical kinetics leads to a large spread in the ignition delays between 800-1200K; on the other hand, the ignition delay is nearly linear for the three different oxygen contents shown. In the simulation, high-temperature ignition is defined to occur when the Favre-averaged OH mass fraction reaches 2% of its stable value; the location of ignition is where maximum local OH is found at ignition time. The simulations show a correct reproduction of the ignition delay trends although a consistent over-estimation of the ignition time is seen.

The soot onset time is defined as the earliest time after SOI when the total soot mass exceeds 0.5 µg. For the simulation, the soot onset location is taken as the axial distance to the point where the maximal SVF is present, at the soot onset time. Analogously, in the experiment it is defined as the axial location where the maximal soot mass across 0.1 mm cross-sectional slices is observed. The latency between high-temperature ignition and soot onset shows a predictable trend. Changing the ambient $O_2$ has a moderate influence on the ignition time and position, but the soot onset latency in both time and distance is considerably increased when decreasing the $O_2$ content. The lower reactivity and flame temperature with low oxygen availability also affects soot formation kinetics (in addition to combustion kinetics) leading to the delayed onset observed. For the ambient temperature variation, the trend is reversed: the

ignition time and distance are themselves strongly influenced but the soot onset latencies are relatively less affected, apart from the 850K case. Across the variations of oxygen and temperature presented, the soot onset time and location from simulation show generally good agreement with the measured values. Latency is slightly under-estimated for low reactivity cases but agrees very well at higher reactivity.

### *Soot mass distribution*

Figure 27 presents the soot mass distribution in 0.1 mm slices along the injector axis from the simulation (solid lines) and experiment (dashed lines). For visualisation, the simulated soot mass has been multiplied by a factor of 2 as indicated in the figure caption. Soot begins with the aforementioned latency after the ignition and has a peak around the onset location (approx. 32 mm). With time, the peak location advances further downstream and the soot mass grows considerably. The rise in soot mass distribution from simulation at earlier time instants after ignition is much more rapid in comparison to measurements. Peak locations are generally in good agreement over the entire duration shown.

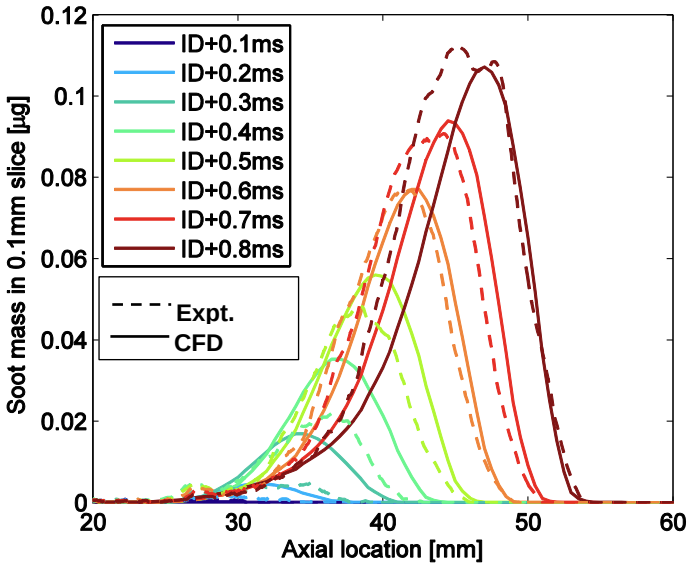


**Figure 27. Soot mass in 0.1mm cross-sectional slices along the axis for the reference case. Time instants have been sorted as time after ignition. Note that the simulation curves are multiplied by a factor of two.**

Following extensive validation of the several distinct indicators of combustion and soot with experimental data, the next sections discuss important quantities obtained from the simulation in order to obtain further insight.

### *Evolution of centreline equivalence ratio, temperature, $C_2H_2$ and SVF*

Figure 28 shows the evolution of important computed quantities along the jet centreline, after the time of ignition. The top two plots show equivalence ratio and temperature. Overall, the equivalence ratio upstream of the burned region is practically unaffected by the flame establishing downstream. Later, the head of the jet develops with marginal influence upstream and eventually the quasi-steady mixture distribution is reached as denoted by the dashed line, where a continuous leaning of the mixture with axial distance is observed. In terms of temperature, the downstream-wise leaning of the jet results into an increase of the temperature. The time sequence of temperature downstream follows the quasi-steady solution, except for the head of the jet where a thin region of higher temperature is observed, due to the further leaning that occurs at the tip of the jet. Further downstream, temperature coincides with the ambient at 900 K. Although the flame exists at the lift-off length, it is offset from the axis, where temperature is still low.

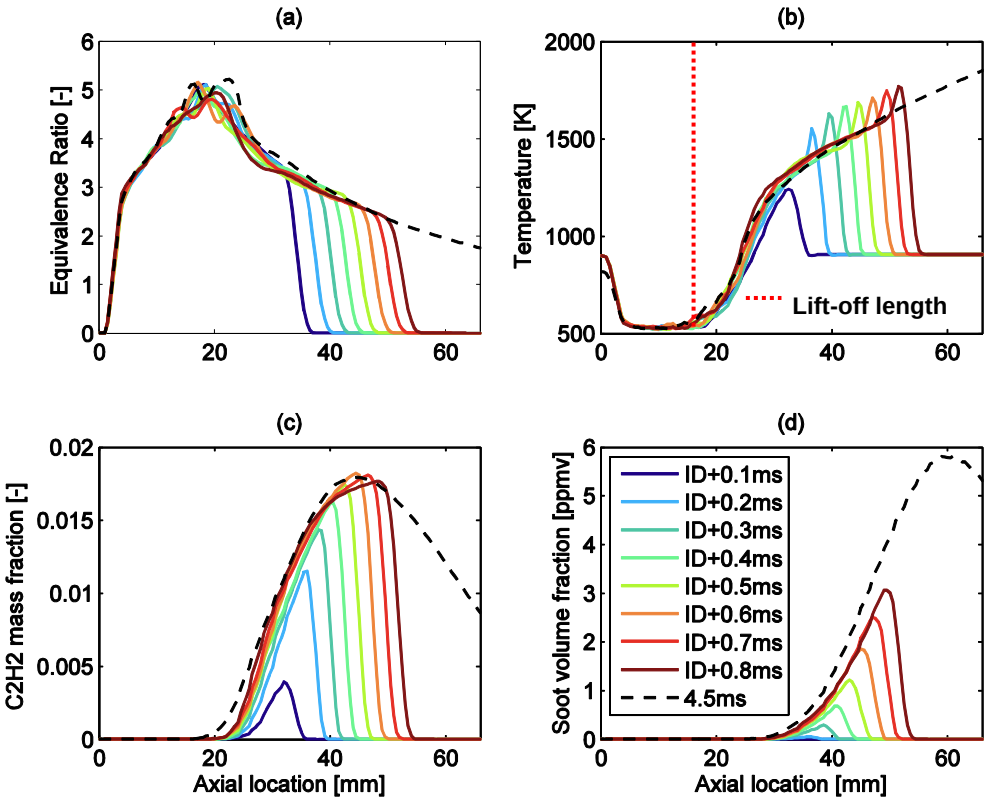


**Figure 28. Simulation results of combustion and soot-relevant quantities along the spray axis, at different time instants as denoted in the legend. Shown are (a) equivalence ratio, red dotted line denotes liquid length; (b) temperature, red dotted line denotes lift-off length; (c) mass fraction of the soot precursor $C_2H_2$; and (d) soot volume fraction. The dashed black line denotes the quasi-steady state profiles at 4.5ms for comparison.**

For $C_2H_2$ the first appearance is at the ignition location, coincident with high-temperature reactions. High levels of $C_2H_2$ are formed within 0.2 ms after ignition and a flame front is clearly visible, as in the temperature time sequence. $C_2H_2$ develops downstream-wise nearly along the quasi-steady solution. The simulation shows that the axial difference between the temperature profiles immediately after ignition and in quasi-steady state (at 4.5 ms) is less than 5 mm. The time sequence of SVF is analogous to the other quantities, particularly $C_2H_2$. It is seen developing in analogous fashion to a flame-front, however it lags behind the temperature front in the same figure (b) due to soot oxidation at the tip.

***Flame structure for reference case at the time of auto-ignition***

Figure 29 shows various combustion-relevant quantities for the reference case at the time of ignition. From left to right are equivalence ratio, temperature, scalar dissipation rate (SDR) (in logarithmic scale), OH, $CH_2O$ and $C_2H_2$ mass fraction distributions. A typical mushroom shape of the jet is identified in the equivalence ratio plot as well as the stoichiometry region in each plot denoted by a solid black line. The temperature plot identifies the ignition region, although the ignition spot is more distinct in the OH distribution. The point of ignition is sufficiently far downstream (and off-axis) from the nozzle, where ignition can no longer be suppressed by high scalar dissipation rate. The evolving mushroom shape of the jet provides a sufficiently low scalar dissipation rate for ignition at this off-axis location, much lower than the on-axis SDR. Importantly, the point of ignition lies very close to the stoichiometric line.

As expected, $CH_2O$ is nearly depleted with the presence of high-temperature reactions, resulting in a complementary distribution of OH and $CH_2O$, although there is a brief persistence of the latter. Acetylene ($C_2H_2$) starts to form in the high-temperature, fuel-rich region. While not shown here, it is observed (in agreement with [5]) that the flame structure in subsequent time follows the stoichiometric line upstream,

to stabilize at the lift off length. These findings are consistent with previous investigations on the n-heptane *Spray H* [41].

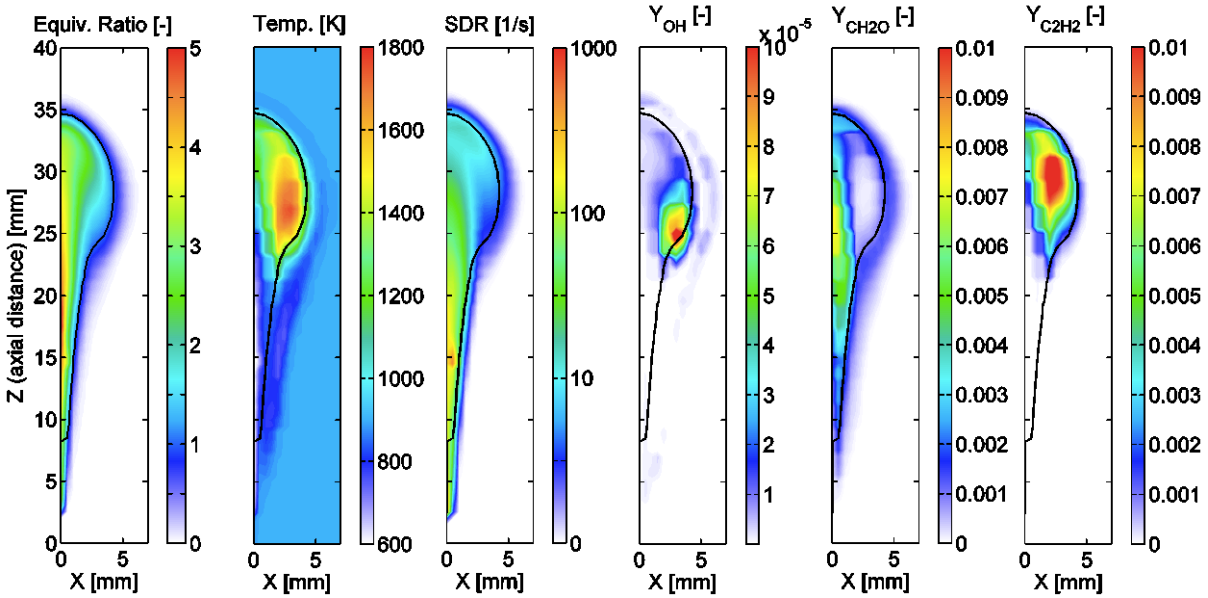


**Figure 29. Simulation results for flame structure for the reference case at 0.6ms (following ignition). From left to right: equivalence ratio, temperature, scalar dissipation rate, OH, $CH_2O$ and $C_2H_2$ mass fraction distributions at auto-ignition.**

After the soot onset, the soot enters quasi-steady-state for which the first and peak soot locations are shown in column 3 of the figure. The first soot is the first axial location where the soot volume fraction (SVF) exceeds one percent of the local maximum. The peak soot location is the location of the maximum. The reference case reproduces both locations with relatively very low error. With a change in oxygen the soot cloud is longer than measured, possibly due to inadequate prediction of oxidation rate towards the tip, which may be mixing-rate controlled. Overall, the peak SVF values show reasonable agreement and the near-linear trends over the oxygen and temperature sweeps are well captured.

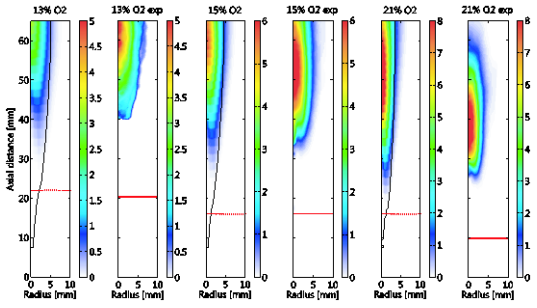


**Figure 30: Soot volume fraction for various ambient $O_2$.**

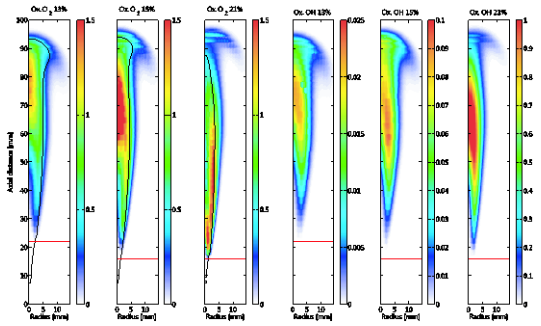

**Figure 31: Soot oxidation by OH and by $O_2$.**

As the ambient oxygen content is reduced, the oxidation due to $O_2$ moves inward from its location along stoichiometry at the 21% $O_2$ case. While the rates of oxidation by OH are comparable to those by $O_2$ at 21% oxygen, there is a stark reduction in the former when the oxygen content is reduced, since the decrease in reactivity and in the flame temperature leads to a lower OH radical presence. Overall the oxidation rate predicted by CMC is limited by the predicted mixing rate and is expected to be underestimated in the simulations presently shown.

These findings have been published in a special issue on “soot dynamics in IC engines” of the *International Journal of Engine research* [42].

### *n-heptane/n-butanol*

#### Standalone mechanism testing for flamelet auto-ignition

First calculations for an n-heptane/n-butanol blend with a volume percentage of 9.1 of butanol have been carried out using chemical kinetics from [33]. The configuration studied is a counterflow auto-igniting flamelet starting from inert mixing. Fuel and oxidiser temperatures are set to 823 and 300 K, respectively at a pressure of 50 bar; these conditions are relevant to Diesel engine operation at start of injection.

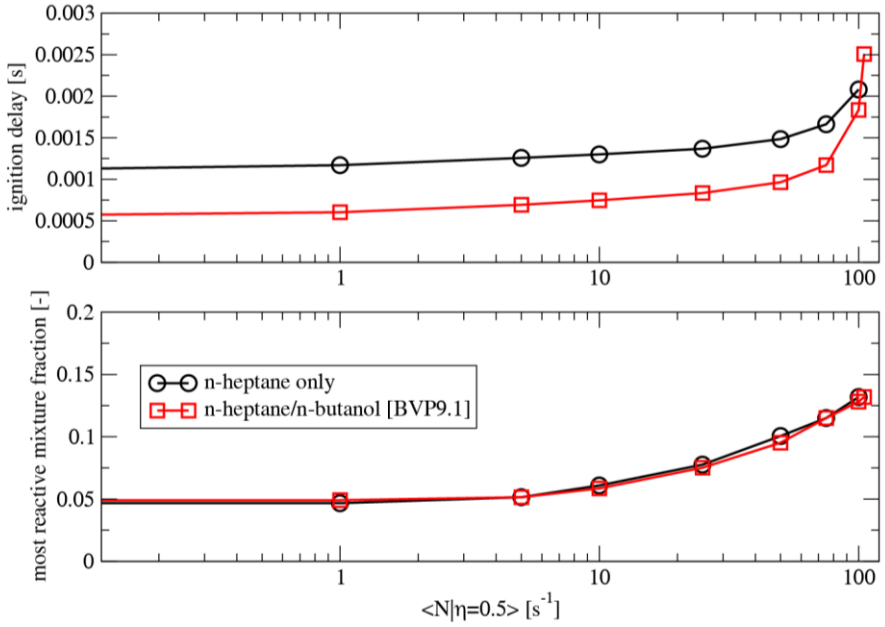


**Figure 32: Auto-igniting flamelet calculations for n-heptane (black) and n-heptane/n-butanol blend (9.1%$_V$ n-butanol, red) for different scalar dissipation rates using chemical kinetics from [33]: ignition delay (upper) and most reactive mixture fraction (lower).**

The impact of straining due to molecular mixing has been investigated for both pure *n-heptane* and the 9.1%$_V$ *n-butanol* plus *n-heptane* blend. Ignition appears to be strongly dominated by *n-heptane* as expected, since the most reactive mixture fraction (the state of mixing at which the maximum conditional temperature first exceeds 1600 K) is unaffected by the addition of *n-butanol*, cf. Figure 32. The ignition delay however is significantly prolonged in the presence of the oxygenated fuel. For *n-heptane*, the ignition delays and scalar dissipation at which ignition no longer can occur are similar to those reported for other *n-heptane* kinetics at the same conditions, cf. e.g. [43, 44].

Findings reported in [45] for HCCI engine measurements and corresponding numerical calculations suggest, that differences in high temperature ignition delays can be linked to the amount of heat released during the low- and intermediate temperature period.

## *Methyl Decanoate*

### Standalone mechanism testing for flamelet auto-ignition

Standalone calculations for Methyl decanoate have been performed using chemical kinetics from [35]. The configuration studied is a counterflow auto-igniting flamelet starting from inert mixing. Fuel and oxidiser temperatures are set to 900 and 350 K, respectively at a pressure of 60 bar and oxygen content of 15%. These conditions correspond to the Spray A reference condition and are compared to previous n-dodecane calculations performed using chemical kinetics from [37] at these conditions in Figure 33.

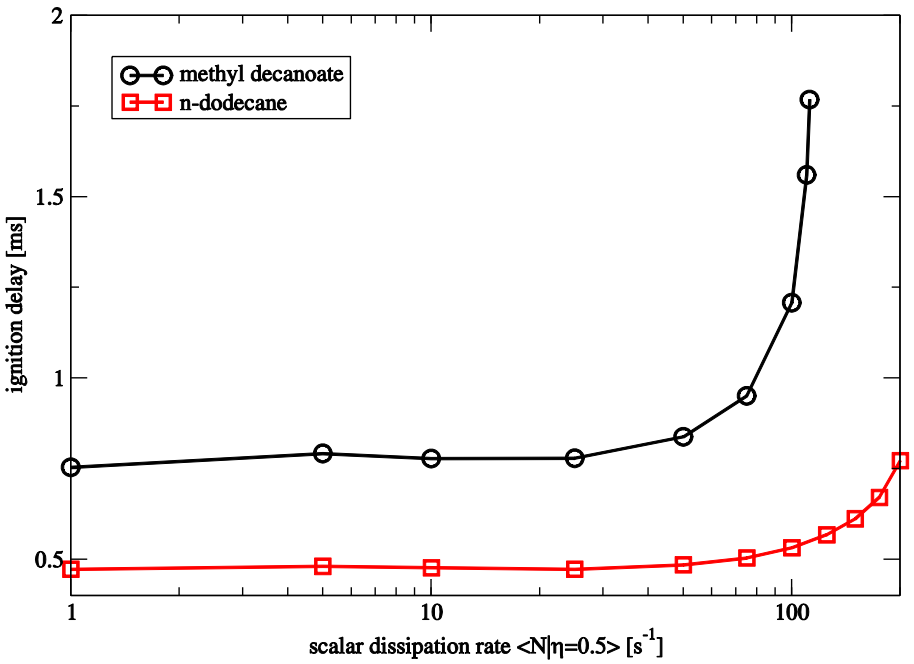


**Figure 33: Auto-igniting flamelet calculations: ignition delay vs. scalar dissipation rate for methyl decanoate (black) compared to *n*-dodecane (red). Chemical kinetics from [35] and [37], respectively.**

Validation data concerning ignition delay and lift-off lengths for methyl decanoate is reported in [46] and contact was established with one of the authors (Dr. Lyle Pickett) to ensure access to further information beyond what is reported in the paper. However, chemical kinetic mechanisms for methyl decanoate discovered in literature, were seen to be developed specifically for methyl decanoate/*n*-heptane blends. While successful application had been reported for instance for 50%-50% (by mole) blends in [35], preliminary application of such kinetics for the pure methyl decanoate cases of [46] showed significant under-prediction of ignition delays, despite accurate liquid properties for methyl decanoate and good agreement in terms of spray morphologies and was attributed to the irrelevant fast-igniting alkane pathways in the mechanism.

Here, the absence of validated chemical kinetics for methyl decanoate at tractable computational cost – ca. 100 species – severely limits further investigations in this direction especially in conjunction with multidimensional engine-relevant models. Cost generally increases with the square of the number of species, leaving detailed kinetic mechanisms with 1000+ species well beyond application in reactive CFD methods resolved in space and time.

# Modifications of high pressure/temperature test rig (WP3)

The optically accessible High Pressure, High Temperature rig at ETH has undergone a number of changes during the course of the project which are summarized in the following.

### *Completion of the HTDZ relocation and control system change*

The relocation of the High Pressure and High Temperature Cell and the commissioning of the new cell control system have been completed in Summer 2013. The 20 year old control system, based on custom made electronics, could not be maintained any longer because replacements for many of the electrical components used therein were simply not available anymore.

The new control system is based on a PLC controller, for such industry standard systems the availability of spare parts is guaranteed for a much longer time. Almost the whole electrical wiring of the cell had to be replaced due to the exchange of the control system.

During the relocation of the HTDZ lab many other parts of the cell that caused problems in the past have been replaced as well, for example most of the cooling water system including the water conditioner (heater/cooler).


**Figure 34: A view of the new HTDZ lab facility with the new control system**

### *Lateral mounting of the fuel injector*

To get a longer free and observable penetration length of the fuel spray of fuel injectors with central, axial nozzle holes it was decided to design a new injector mounting system that can be installed in place of one of the side windows in the cell.

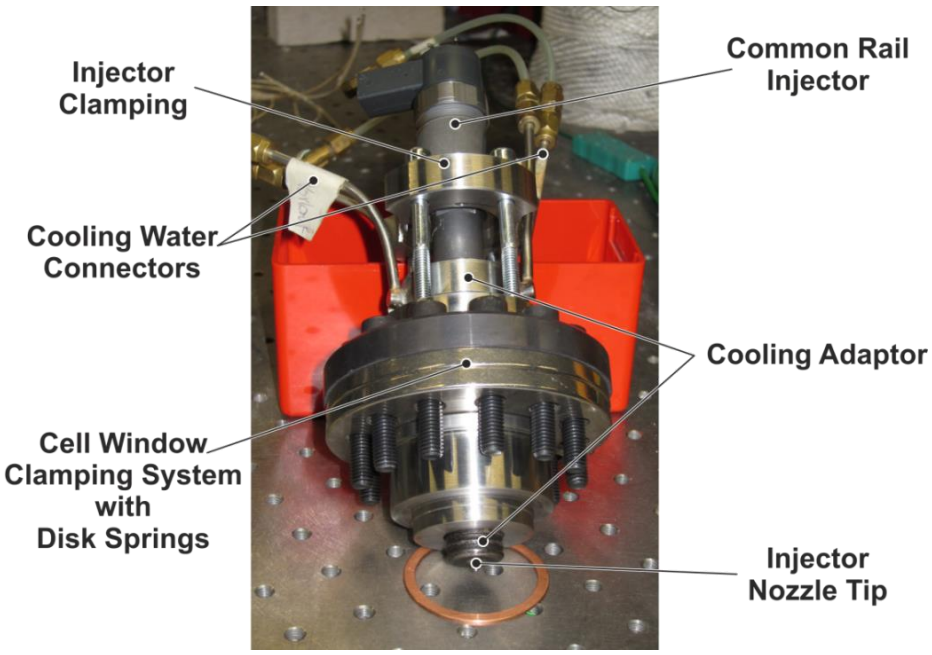


**Figure 35: Common Rail injector ready to be mounted in place of one of the side windows of the cell.**

To ensure tight sealing of the cell (pressure in excess of 100 bar) and compensation for thermal expansion (cell temperatures above 500 °C) the same disk spring clamping system is used as in the window mounts. Nonetheless the injector mounting system is able to provide the same installation space as the “standard” injector mounting hole of the cell, so any injector or injector and cooling system designed for the cell in the past can be mounted sideways in the current setup. The mounting system has been manufactured and has been used during the experimental campaigns. A view of the system can be found in Figure 35 above.

### *Schlieren double-pass setup*

In order to apply double-pass Schlieren in the HTDZ at LAV a set of new components have been designed:

- A high temperature mirror to be put in the cell during the experiments (provided by the company LaserOptik AG)
- A mirror holder
- A new injector holder to accommodate the injector in the new configuration of the chamber

The latter two components have been designed and manufactured in-house. A sketch of the chamber with the new components is presented in Figure 36.

The Double-pass Schlieren imaging has been combined with a high speed OH* chemiluminescence setup to perform simultaneous measurements. The combination of these two measurement techniques can provide precious information about the spray formation and the different phases of the combustion.

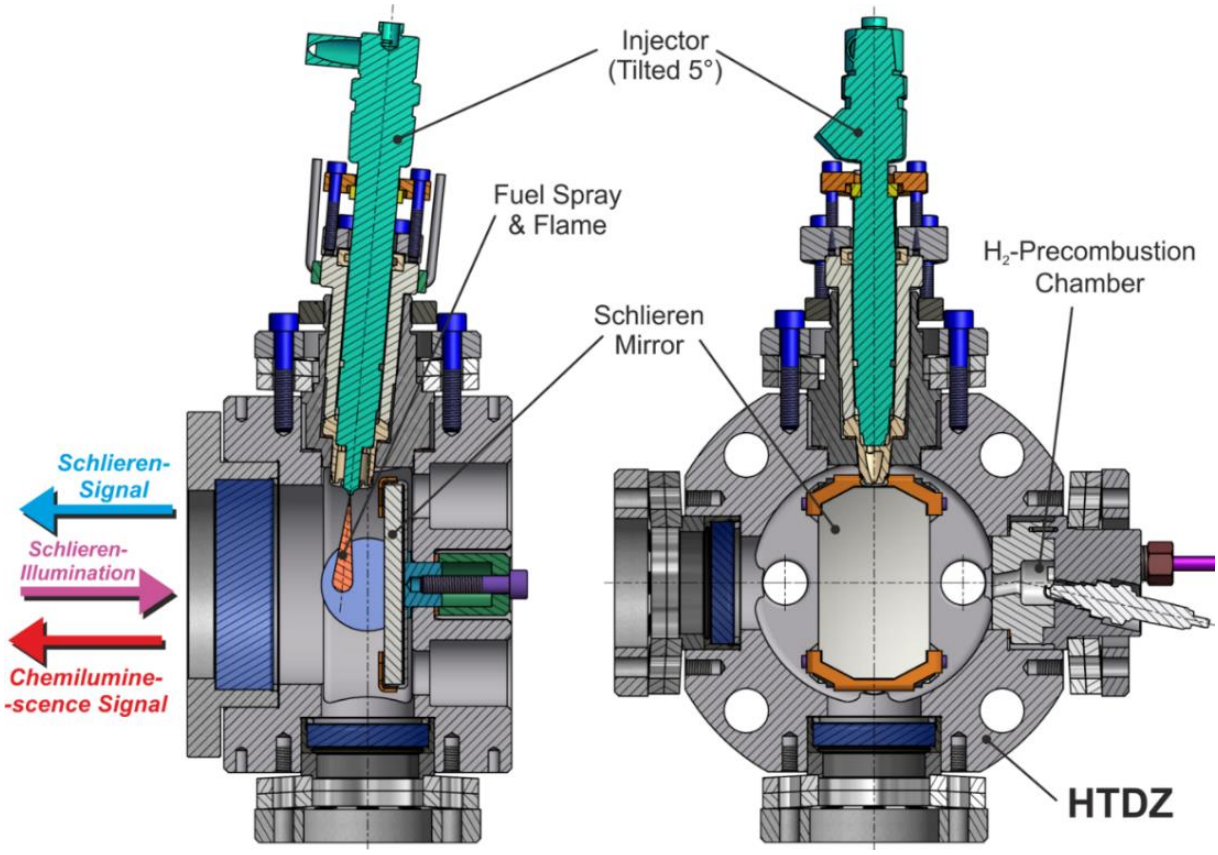


***Figure 36. Double pass Schlieren setup. The sketch shows the high-temperature mirror mounted in the vessel and the new injector holder.***

In Figure 37, a picture of the setup gives an idea of the optical setup employed: in order not to interfere with the Schlieren setup the OH* camera has been mounted under the Schlieren optics using two UV mirrors mounted in a “Z” configuration.

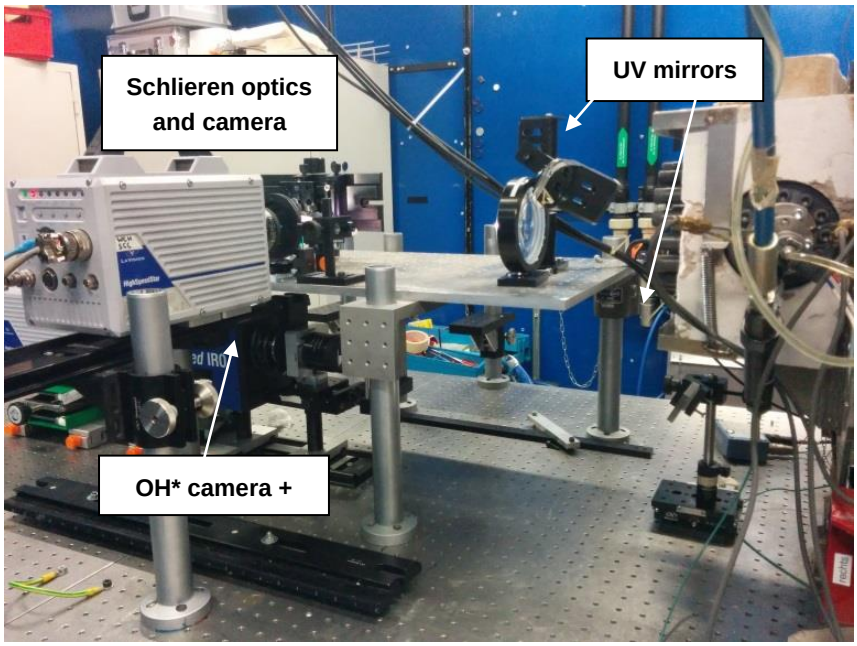


***Figure 37. Schlieren setup combined with the high speed OH* chemiluminescence system. In order not to interfere with each other, the OH* chemiluminescence setup has been mounted under the Schlieren optics, using two UV mirrors mounted in a “Z” configuration.***

### *New injectors with single-orifice coaxial tips*

The main goal of work package 3 (**WP3**) is the modification and preparation of the high pressure/temperature (HTDZ) test rig and of all involved parts. The modified test rig isable to produce a detailed database from experiments based on optical measurements, which can be used for CFD model validation . In that view, single axial-hole injector nozzles have been installed on solenoid BOSCH CRI 2.2 injector bodies. After the characterization of the injector behavior using a Bosch tube injector rate analyzer, it was found that there is a strong influence of cavitation effects on the single-hole injectors.

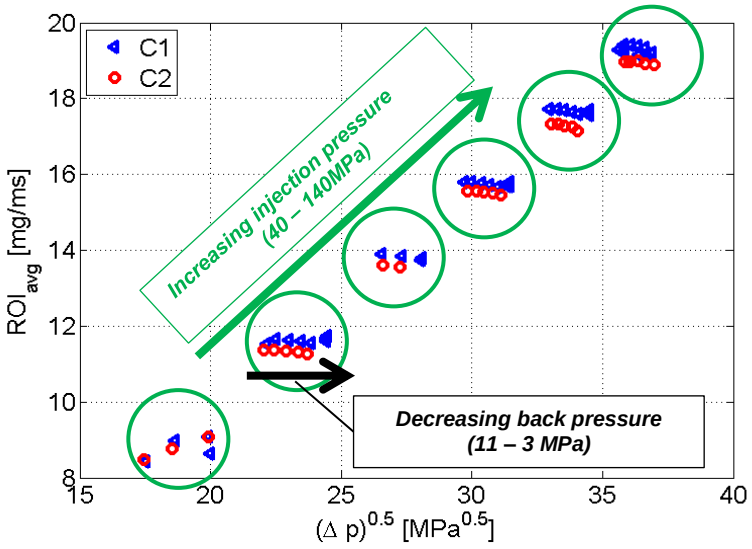


**Figure 38. Average rate of Injection ($ROI_{avg}$) related to the pressure difference (ΔP) obtained at different combinations of injection pressures (40-140 MPa) and back pressures (11-3 MPa) for the nozzles C1 and C2 with orifice diameter 0.240 mm.**

Figure 38 shows that the rate of injection (ROI) depends only on the injection pressure (measured before the nozzle hole) and is almost independent of the back pressure. Normally, it would be expected that the mean rate of injection is proportional to the square root of the pressure drop, as a direct consequence of the following equation:

$$\dot{m}_f = C_v \cdot C_a \cdot A_{geo} \cdot \sqrt{2\rho_f} \cdot \sqrt{\Delta P} \qquad (1)$$

where: $\dot{m}_f$ :mean mass flow, $C_v$: velocity coefficient, $C_a$: area coefficient, $A_{geo}$: geometrical area, $\rho_f$: density of the fuel and $\Delta P$: pressure difference.

But, as can be easily seen from Figure 38, the rate of injection for nozzles C1 and C2 is not affected by the effective pressure difference suggesting that there are strong cavitation effects in the nozzle hole flow of the investigated injectors. Similar behavior is observed also for the rest of the employed injectors (Appendix A).

However, modern Diesel fuel injectors eliminate (or greatly reduce) the cavitation in the nozzle hole flow by replacing the cylindrical holes with conical ones. The conical holes have highly rounded inlet hole edges and are larger towards the inside. This geometry prevents the separation of the boundary layer from the hole wall and the creation of the so-called “vena-contracta” which can then lead to the formation of recirculation area between the “vena-contracta” and the orifice wall. Seeing that the already employed injectors are not suitable for comparison with the current state of the art injectors used in automotive applications, there is a clear need for fabrication of improved LAV/PSI standardized single hole injectors.

## New improved LAV/PSI standardized single hole injectors

The new improved injectors bare conical nozzle holes including hydro-erosive grinding of the hole inlets. The nozzle tips (without the holes) were sourced from Bosch directly, while the fabrication of the conical nozzle holes was performed by “Ganser CRS AG”. The hydro-erosive grinding of the edge at the hole inlet was performed by “Sonplas” and the company “UNITS” performed the X-ray tomography of the nozzles. The injector bodies have been replaced by the new modern version of the magnetically control common rail injector: BOSCH CRI2-16.

The manufactured nozzle holes had four different diameters of: 0.090, 0.120, 0.180 and 0.240 mm. Multiple copies of each diameter were manufactured. These copies are going to be employed and tested at the nominally identical facilities at the Laboratory of Aerothermochemistry and Combustion Systems (LAV) and the Paul Scherrer Institute (PSI). The nomenclature of the different nozzles together with their characteristics is listed below in Table 10. After the grinding process and seeing the fact that CFD modeling requires detailed information about the internal geometry of the nozzles, “Units” performed X-ray tomography (Metrotom 1500) of the nozzle tips. In Figure 39, the images from nozzle 2A6 are presented as an example.

**Table 10. Nozzle orifices diameter before and after grinding and related discharge coefficient, $C_D$ values.**

| Nozzle Type | Nozzle Set # | Nominal orifice diameter [mm] | Measurement before grinding | | Measurement after grinding | | |
|---|---|---|---|---|---|---|---|
| | | | Spray hole diameter (outlet) [µm] | Discharge coefficient, $C_D$ | Spray hole diameter (outlet) [µm] | Flow increasing [%] | Discharge coefficient, $C_D$ |
| AA | 1 | 0.090 | 102.89 | 0.70 | 103.37 | 14.08 | 0.79 |
| | 2 | | 101.94 | 0.69 | 103.65 | 19.52 | 0.80 |
| | 3 | | 100.57 | 0.71 | 103.97 | 17.52 | 0.79 |
| | 4 | | 102.36 | 0.70 | 102.85 | 13.42 | 0.79 |
| | 5 | | 100.62 | 0.72 | 103.48 | 15.53 | 0.78 |
| 2A | 1 | 0.120 | 131.39 | 0.76 | 134.81 | 14.46 | 0.83 |
| | 2 | | 131.17 | 0.77 | 134.41 | 13.87 | 0.83 |
| | 3 | | 130.27 | 0.77 | 134.68 | 14.84 | 0.83 |
| 2B | 1 | 0.180 | 189.11 | 0.77 | 190.58 | 14.38 | 0.86 |
| | 2 | | 191.20 | 0.75 | 191.65 | 14.95 | 0.86 |
| | 3 | | 185.33 | 0.80 | 190.47 | 14.57 | 0.87 |
| 2C | 1 | 0.240 | 251.02 | 0.63 | 251.15 | 16.63 | 0.74 |
| | 2 | | 252.90 | 0.62 | 253.03 | 16.16 | 0.72 |

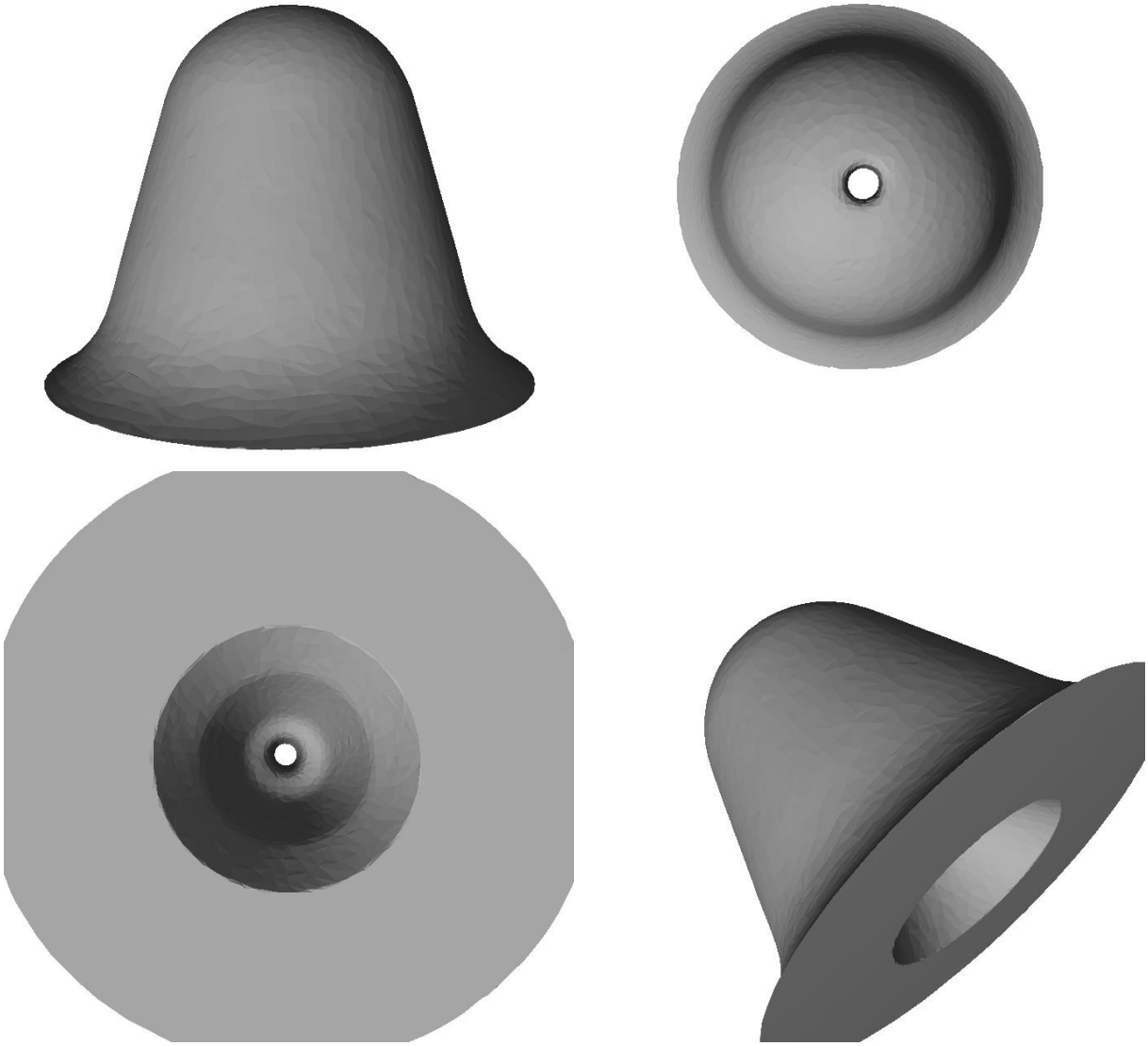

**Figure 39. Images of the nozzle 2A6 at different angles, obtained by "Units" using X-ray tomography. Top left: image from the side, top right: image from the top, bottom left: image from the bottom and bottom right: image from an arbitrary angle.**

## Recommissioning of the $H_2$-Pre-combustion (with spark plug ignition)

In order to perform experiments in conditions similar or close to the real engine applications, an $H_2$ pre-combustion system has been installed in the HTDZ at LAV. The cell itself allows a wide variation of pressure and temperature conditions, which can vary from 0.1-8 MPa and from 300-750 K without $H_2$ pre-combustion. In order to reach higher temperatures in the cell, the $H_2$ pre-combustion system was recommissioned and mounted in the HTDZ. In Figure 40, a sketch of the chamber with the $H_2$ pre-combustion unit, which consists of a mixing prechamber and a spark plug, is presented.

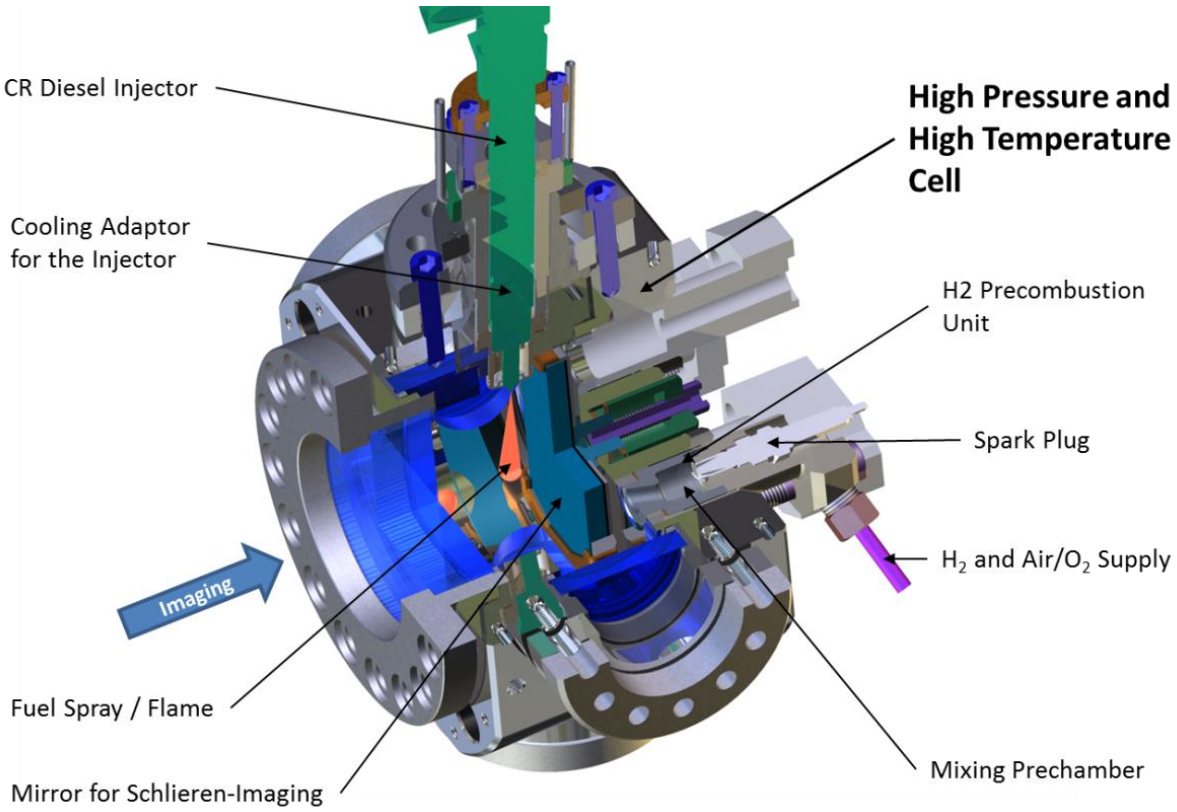


**Figure 40. Sketch of the high pressure/temperature cell (HTDZ) with the $H_2$ pre-combustion unit and the temperature resistive mirror mounted on it for double pass Schlieren measurements.**

# Measurements in high pressure/temperature test rig (WP4)

### *Mass flow rate characterization of new improved LAV/PSI standardized single hole injectors*

The characterization of each of the aforementioned injectors is presented in this section. In order to have a detailed and accurate characterization of each injector, an extensive matrix of operating points was used. The parameters investigated were the Energizing time (ET), Injection pressure ($P_{inj}$) and back pressure ($P_{back}$), while the difference in the rate of injection for single or double injections has been studied, as well. The employed values of each parameter are summarized in Table 11.

**Table 11. Matrix of conditions for single and double injections for the investigation of rate of injection**

| Single Injection | | |
|---|---|---|
| **Back pressure [MPa]** | **Injection pressure [MPa]** | **ET (ms)** |
| 3 | 40 | 0.1 |
| 5 | 60 | 0.2 |
| 7 | 80 | 0.3 |
| 9 | 100 | 0.4 |
| 11 | 120 | 0.5 |
| | 140 | 0.7 |
| | | 1.0 |
| | | 1.5 |
| | | 2.0 |
| | | 2.5 |
| | | 4.0 |

| Double Injection ($P_{back}$=5MPa, $P_{inj}$=60 & 140 MPa) | | |
|---|---|---|
| **Pre injection ET[ms]** | **Time between injections [ms]** | **Post Injection ET [ms]** |
| 300 | 500 | 2000 |
| | 677 | |
| | 833 | |
| | 1000 | |
| | 1333 | |
| 2000 | 1500 | 300 |
| | 1667 | |
| | 1833 | |
| | 2167 | |
| | 2500 | |

### *Profiles of Rate of Injection under different conditions*

The rate of injection of different nozzles with different nozzle tip diameters was measured using Diesel fuel and changing the injection pressure in the range of 40 MPa to 120 MPa, while changing the back pressure in the range of 3-11 MPa. Figure 41shows the effect of the all these parameters on the rate of injection. The top figure indicates that the injection rate increases for bigger diameter nozzles as expected, while the hydraulic opening and closing delay seem to be very steep in all cases. It is clearly observable that the hydraulic opening delay was found to be identical for all nozzles, while in the case of the closing delay it seems that there is a small variation between the different injectors.

As can be also seen from Figure 41 below, the rate of injection depends strongly on the injection pressure as expected. Results show that changes in injection pressure produced significant differences over the curves of injection rate in a monotonic way. However, this was not the case for the closing delay where the maximum closing delay was observed for $P_{rail}$= 80 MPa. The hydraulic opening delay doesn`t seem to be affected at all.

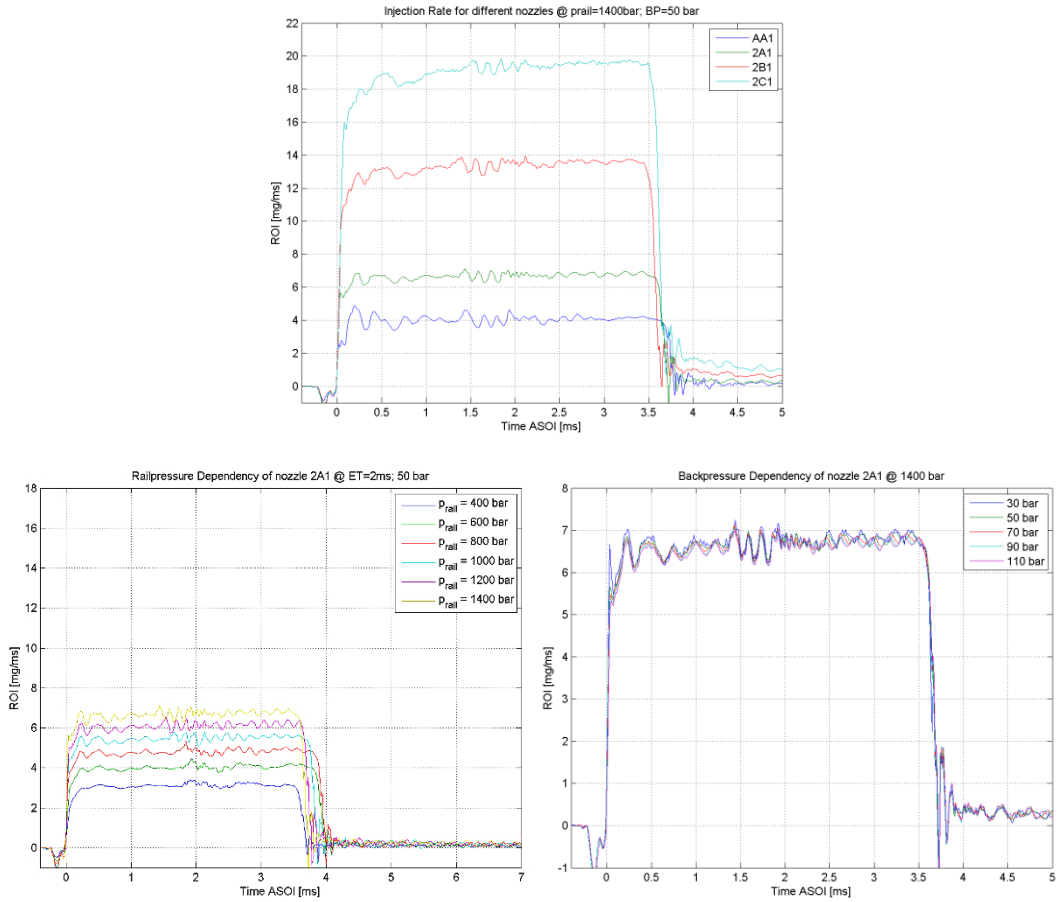


**Figure 41. The temporal profile of rate of injection (ROI) as a function of the nozzle diameter (upper row), injection pressure (lower row, left figure) and back pressure (lower row, right figure).**

## Mean rate of injection and injected amount by all injectors under different experimental conditions

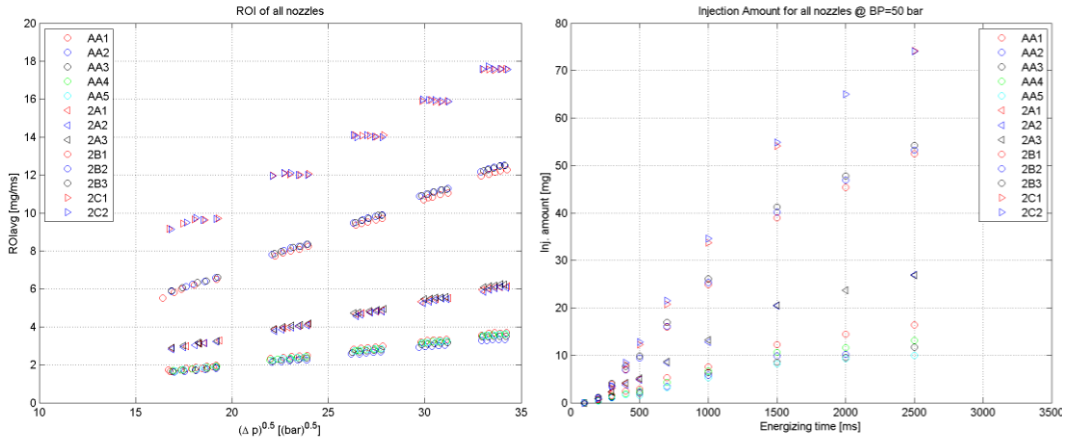


**Figure 42. The mean value of rate of injection (left) and the injected amount (right) as a function of the square root of the pressure difference between the injection pressure and the back pressure for all nozzle diameters.**

The plots presented in Figure 42 indicate that almost all the injectors do not show cavitation thanks to the new geometry of the nozzle tips and the average rate of injection appears to depend in a linear way to the square root of the pressure difference between the injection pressure and the back pressure for most of the cases. Surprisingly, the only injector which deviates from the general trend and shows still strong cavitation is the one with the largest diameter.

From Figure 42 it also becomes clear that the injected amount increases with the energizing time and the nozzle diameter as expected. Moreover the average rate of injection and the injected amount acquired using different nozzle tips of the same diameter appear to be almost identical; this suggests that the results from the optical measurements derived from the two different facilities (LAV and PSI) can be directly compared.

Summarizing the above results one can conclude that all the new modified injectors, except the ones with the largest diameter (Ø 0.240 mm, 2C1-2C3), do not suffer from cavitation effects and they appear to have the desirable performance, while the injected mass can be tuned easily by adjusting either the energizing time or the injection pressure. This renders the new injectors more reliable and more representative of commercial engine injectors.

### *Spray characterization and soot concentration*

The aim of this work is to study the development and evaporation of different fuel sprays and the soot generated by the combustion. This will be done by applying different optical techniques in a high temperature high pressure chamber with optical accesses. Additionaly, the results will be employed as a database to validate different chemical reaction mechanisms for diesel surrogates.

#### *Experimental conditions*

In order to have a good understanding of the effect of the ambient temperature and fuel composition on the spray parameters, soot generation and ignition delay, five fuels and four temperatures were chosen as summarized in Table 12; details on the fuel blends can be found in Table 14 in the appendix. *N*-heptane at 900 K ambient temperature (shown below in blue) has been chosen as the reference point for further comparison among fuels and ambient temperatures.

**Table 12. Matrix of experimental conditions. All points are performed at 1500 bar injection pressure and 22.5 kg/m$^3$ ambient density. *n*-heptane at 900 K was chosen as a reference point.**

| Fuel \ Temperature | 700 K | 800 K | 900 K | 1000 K |
|---|---|---|---|---|
| *n*-heptane | x | x | **x** | x |
| *n*-heptane / Toluene | x | x | x | x |
| *n*-heptane / 1-butanol | x | x | x | x |
| OME234 | x | x | x | x |
| OMEmix | x | x | x | x |

To achieve the desired temperature and pressure of the ambient species in the chamber, the constant volume chamber was filled with air at a certain pressure, then a specific mass of hydrogen and additional air are injected into the chamber air and then ignited via a spark plug. The pre-combustion event of the hydrogen leads to high temperature and pressure conditions at the time of injection, which would not be possible only with the electrical heating. The consumption of oxygen during this pre-combustion event was designed to obtain the oxygen concentration required for the investigations. As the peak is reached and the pressure in the chamber drops to the trigger pressure, the injection is triggered at the right moment. In this investigation, the trigger pressures are 70 bar, 62 bar, 54 bar and 47 bar that represent

gas-averaged temperatures of 1000 K, 900 K, 800 K, and 700 K, respectively. A schematic of such a pre-combustion event is shown in Figure 43 below.

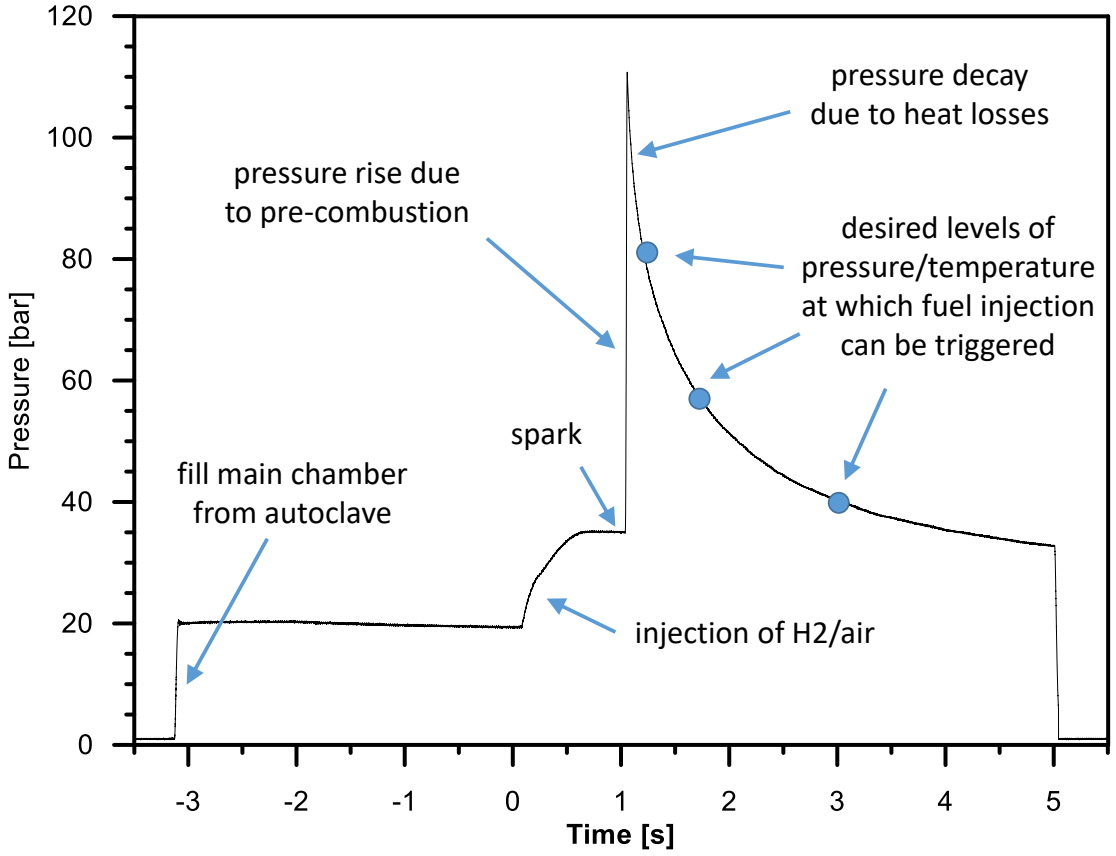


**Figure 43. Schematic of pressure evolution during a pre-combustion event.**

As the fuel injector is triggered with an energizing time of 4500 µs, it takes some time for the injector to actually raise the needle and allow the fuel flow in chamber. This time is in addition to the ignition delay time the fuel until high temperature ignition. The net sum of these times create a time delay between fuel injection trigger and actual auto-ignition event of the fuel. The oxygen concentration can be simply estimated by the consumption of hydrogen combustion. In this investigation, the oxygen concentration is 13% in mass.

### *Experimental setup for spray characterization and optical techniques*

In order to characterize the spray parameters and soot generated, different optical techniques have been applied. The experimental layout can be seen in Figure 44 and the detailed parameters of ech system are show in Table 13.

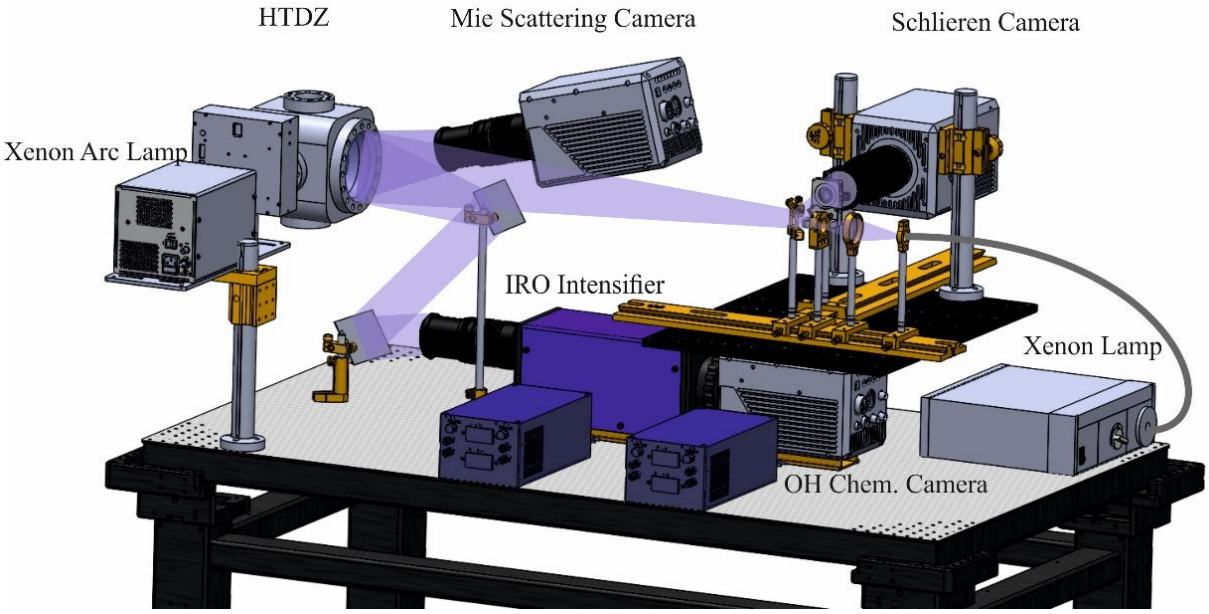


**Figure 44. Experimental layout of the high speed OH* chemiluminescence, Schlieren and Mie-scattering techniques.**

**Table 13. Configuration values for the different imaging systems.**

| Optical technique | OH* chemiluminescence | Schlieren | Mie-scattering |
|---|---|---|---|
| Camera | LaVision HSSX | LaVision HSSX | LaVision HSS5 |
| Intensifier | LaVision IRO | -- | -- |
| Resolution [px] | 768 x 432 | 512 x 320 | 768 x 176 |
| Exposure time [µs] | 165.05 | 5 | 1-54 |
| Speed [FPS] | 6,000 | 60,000 | 20,000 |

The digital images have been analysed by means of purpose-developed processing software, which delivers the spray/flame geometrical parameters.

1. High-speed Schlieren photography was applied to quantify the penetration of the vapour phase of the spray. The extent of penetration of the vapour phase, referred to as “vapour penetration”, can be determined using the first spatial derivative of density within the combustion chamber, which makes it useful to detect spray boundaries [47]. This technique shows the boundary between vaporized liquid and background gas because of the refractive index differences that exist between them [48, 49]. An example of a Schlieren image can be seen in Figure 45. The routine used for the processing was developed by Sandia National Laboratories as part of the Engine Combustion Network and is available on-line [11]. The code is based on the successive calculation of two standard deviation images to remove the Schlieren effect of the hot ambient gases and to detect the spray boundary.

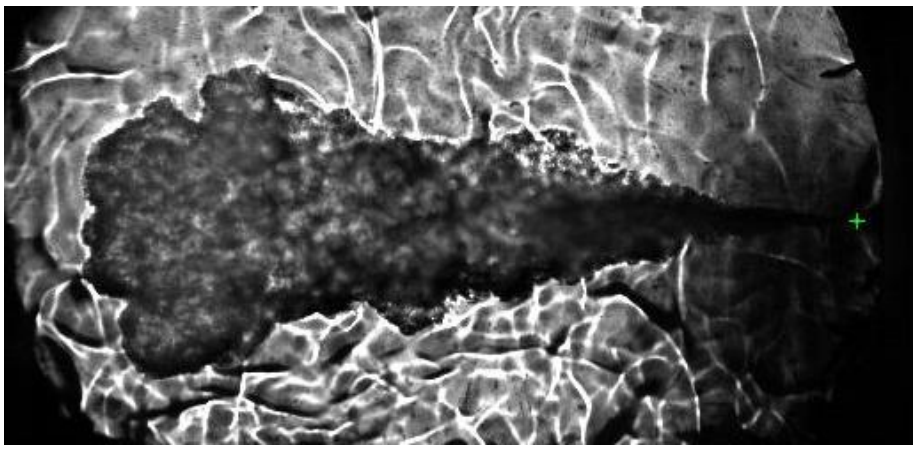

**Figure 45. Sample Schlieren image at 2000 µs after SOE; the green cross marks the nozzle tip.**

2. The distance of the tip of liquid core from the nozzle exit, referred to as “liquid length”, has been captured by Mie-scattering imaging, which relies on the light reflected by liquid droplets. The spherical particles larger than one tenth of the incident wavelength are scattering the light under the hypothesis of kinetic energy conservation, also known as “elastic scattering", and most of it is reflected in the same direction of the incident wavelength. An example of a Mie-scattering image can be seen in Figure 46. The processing routine first subtracts the background, which is calculated by averaging the images taken prior the start of injection. Then, the contour of the liquid core is determined by means of a thresholding algorithm reported in [11, 50]. Finally, the maximum liquid length is obtained by averaging the distance to the nozzle of the contour points that are ±1 mm around the intersection of the liquid spray axis and the calculated contour. No connectivity algorithm has been applied, so some liquid ligaments that sometimes are detached from the continuous liquid core are not accounted for to calculate liquid length.

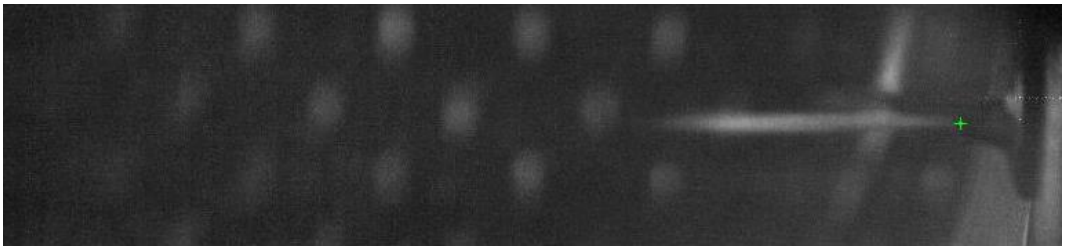

**Figure 46. Sample Mie-scattering image at 2000 µs after SOE; the green cross marks the nozzle tip.**

3. OH* chemiluminescence was used to determine the burning area; from this, two parameters were obtained. One is the distance from the nozzle to the base of the flame, which will be referred to as “lift-off length”; the other is the distance from the nozzle to the tip of the flame, which will be referred as “flame penetration”. This technique records radiation at 310 nm, which is controlled by the OH* radical, being a marker of the diffusion flame limits, and thus of the lift-off length for diesel sprays [51]. The OH* chemiluminescence occurs at stoichiometric conditions and high temperatures, therefore being a good marker of the lift-off length [52]. Additionally, the wavelength band of 310 nm that corresponds to the chemiluminescence of the OH* radical is the strongest one and therefore best for determining the lift-off length [52, 53]. Figure 47 shows an image of OH* radiation. These images are similar in appearance to the broadband ones, but with different spectral information; the lift-off length is calculated as the closest zone to the nozzle where flame can be found [51]. The algorithm adds the values per row so a curve “Digital level vs Axial distance” can be obtained; then, the lift-off length is calculated as the average level between valley and first peak of each curve, as this gives the mean location of the turbulently fluctuating lift-off length [51]. In a very similar way, the flame penetration is calculated as the farthest value from the nozzle tip.

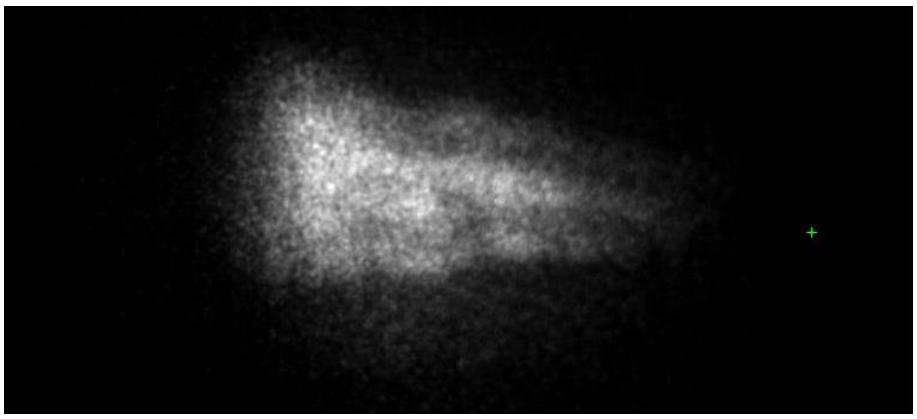

**Figure 47. Sample OH* chemiluminescence image at 2000 µs after SOE; the green cross marks the nozzle tip.**

4. For soot concentration, two different optical techniques were applied:

    a. First, broadband radiation was recorded to compare the luminosity emitted by the flame of all fuels at different conditions. This technique records the flame broadband radiation, which corresponds to the soot thermal luminosity during the diffusion combustion phase. This type of radiation may have to kinds of contributions, chemiluminescence and incandescence. Under most of the operating conditions, the second is the fundamental one as it depends on the amount of soot and its temperature, therefore it will be used for a qualitative analysis of such parameters. Figure 48 shows a sample image of broadband radiation. An average background image is calculated for each repetition and based on that image and a threshold, a mask is generated to define the region of interest. Then, the area of the flame and cumulative digital intensity are computed, and based on those two values the specific intensity is obtained.

**Figure 48. Sample broadband radiation image at 2000 µs after SOE; the green cross marks the nozzle tip.**

    b. Second, spatially integrated (0-diamentional) 3-colour pyrometry was used to quantify the temporally-resolved amount and temperature of soot. This technique was applied exclusively at the conditions which presented significant luminosity.

5. In order to calculate the ignition delay time the following methods were used. According to [54] from Sandia National Laboratories, chemiluminescence high-speed imaging and Schlieren were performed to measure the location and timing of ignition, defined as being the onset of high-temperature heat release. In the literature [55], Schlieren imaging have been used to identify transients in auto-ignition and lift-off length after ignition. OH* chemiluminescence imaging is used to investigate the ignition delay and lift-off length of a three-hole nozzle (Spray B). The experimental conditions in the present investigations are similar to the ones in the abovementioned literature; therefore, the measurement and post-processing methods can be used in a similar way to obtain ignition delay information.

Figure 49 shows a typical temporal evolution of the vapour and flame penetration and the liquid and lift-off length (reference point: n-heptane at 900 K). It can be seen that the penetration of the liquid and vapour phase are the same at the beginning as the fuel is still not fully evaporated. After a certain distance from the nozzle, 7 mm in this case, the liquid length stabilizes, as beyond this point the fuel is fully in vapour phase. However, the vapour phase keeps on growing, as its penetration depends mostly

on the momentum of the spray. It does become flat after 80 mm, but this is only because that is the limit of the chamber; otherwise, it would penetrate further.

As opposed to the aforementioned parameters, the lift-off length and flame penetration do not start from the nozzle tips, as the ignition takes place upstream. It is well established that high temperature reactions are initiated at locations where scalar dissipation rate are low, near the spray tip. In this case, the ignition takes place at around 25 mm from the nozzle tip and that is where both flame-related parameters start to appear on the plot. Analogously to the liquid length, the lift-off length also stabilizes; although there may be some fluctuations due to turbulence, the flame will present a quasi-steady mean value [17, 56]. The flame will stabilise at the location where the spray velocity equals the flame propagation/reactivity velocity. On the other hand, the flame tip keeps on penetrating along with the vapour phase and it stabilizes after the fuel has burnt and only the products are left.

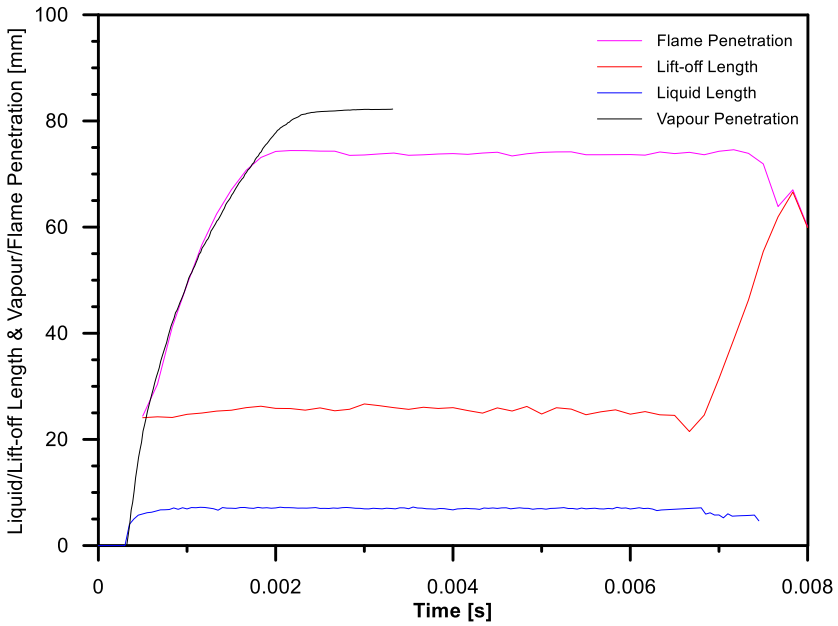


**Figure 49. Evolution of liquid length, vapour penetration, lift-of length and flame penetration, for n-heptane at 900 K ambient temperature.**

### *Liquid penetration*

In this section, the results of the liquid penetration will be discussed for the variation of ambient temperature and fuel composition.

Figure 50 shows the evolution of the liquid length for n-heptane at all four ambient temperatures tested. The results show that the liquid penetration is reduced as the ambient temperature increases. This can be explained by the fact that the higher temperature is causing the fuel to evaporate faster and therefore closer to the nozzle tip, resulting in a shorter liquid length [57-59].

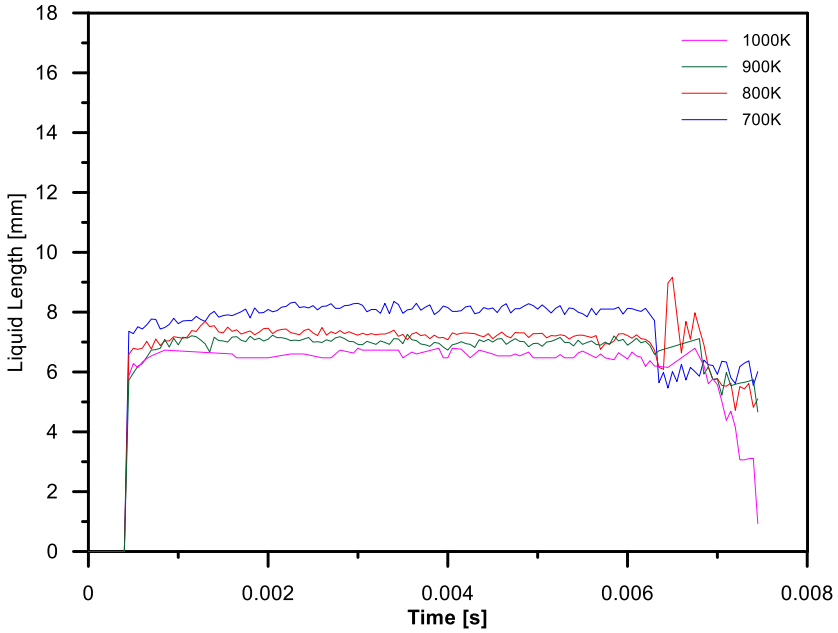


**Figure 50. Evolution of liquid length for *n*-heptane at all ambient temperatures tested (700 K-1000 K).**

Figure 51 presents the evolution of the liquid lengths for all fuels at 900 K of ambient temperature. In this case the trend is not as straight-forward as with a temperature variation; the liquid length depends on the fuel evaporation properties. An obvious stratification is shown, where the OME blends present longer liquid lengths while the *n*-heptane blends have shorter ones. This can be correlated to the evaporation properties of the fuels, where heavier blends like OME will need more energy and take more time to evaporate compared to *n*-heptane [60, 61].

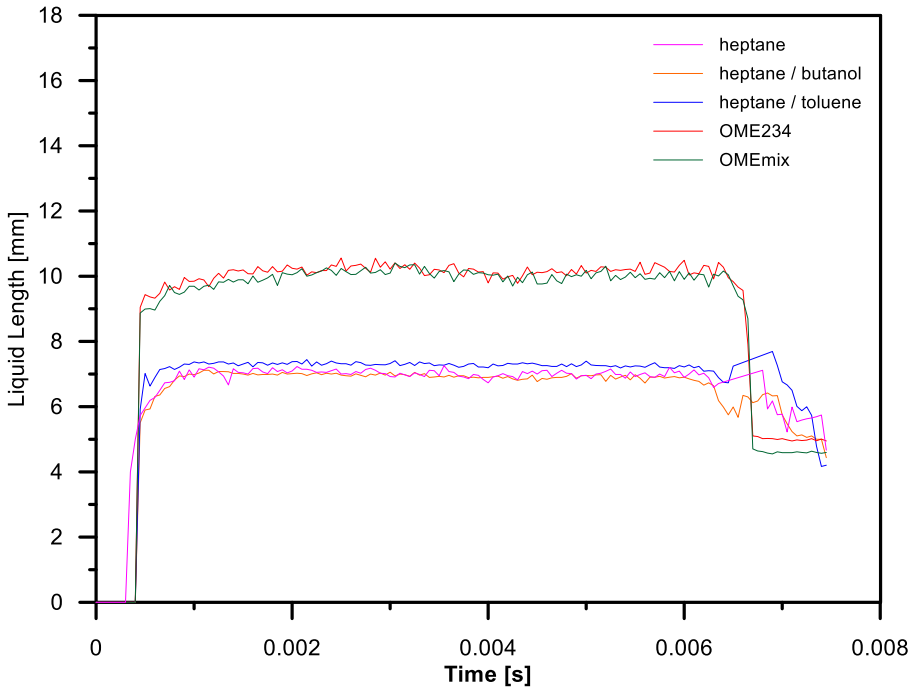


**Figure 51. Temporal evolution of liquid length, for all fuels at 900 K ambient temperature.**

Figure 52 presents a summary of all liquid length across the whole experimental matrix. The same trends that were discussed before can be seen here, where the longer liquid lengths correspond to the lowest temperatures for all fuels.

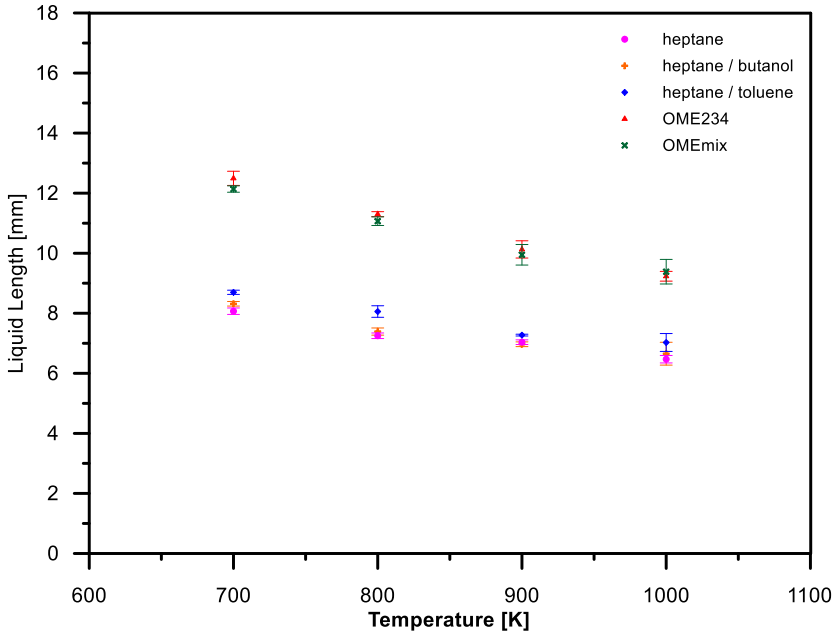


**Figure 52. Average values for liquid length, for all fuels as a function of the ambient temperatures.**

### *Vapour penetration*

In this section, the results of the vapour penetration will be presented. As seen in Figure 49 the penetration of the vapour phase becomes flat as it reaches the end of the combustion chamber, therefore, Figure 53 and Figure 54 present a reduced time range in order to focus on the important part of the curve.

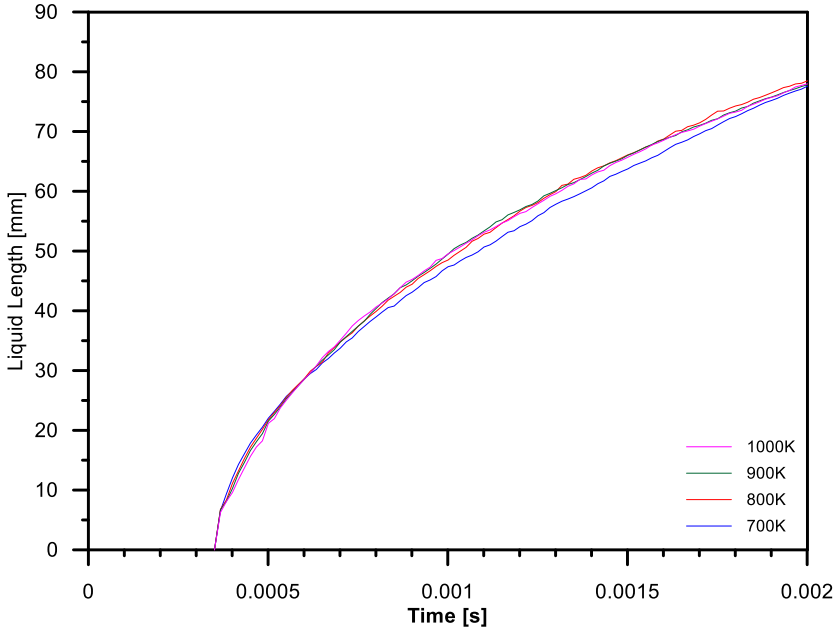


**Figure 53. Evolution of vapour penetration for *n*-heptane at all ambient temperatures tested (700 K-1000 K).**

Figure 53 shows the evolution of the vapour penetration for *n*-heptane at all ambient temperatures. The curve corresponding to 700 K is below the other three as the ignition delay is much longer than in the higher temperatures. For the other cases, the initial part of the penetration is equal before ignition as the penetration rate is only affected by the spray momentum and the ambient density, both of which are the same for all conditions. After ignition, the spray will start accelerating, causing the tip to penetrate

faster, therefore, the curve corresponding to 1000 K will start deviating earlier from the 700 K curve, followed by 900 K and then 800 K.

Figure 54 presents the penetration rate for all fuels at 900 K; a similar grouping between the fuels as seen in Figure 51 can be observed; however, in this case it has to do with the fuel density. As opposed ot the paragraph above, the ambient density is constant between the fuels but the momentum of each fuel is different as it is related to the fuel density (fuel pressure is constant between the fuels). Therefore, fuels with higher density like OME will have a higher momentum and penetrate faster for an equal injection pressure, which is the case here.

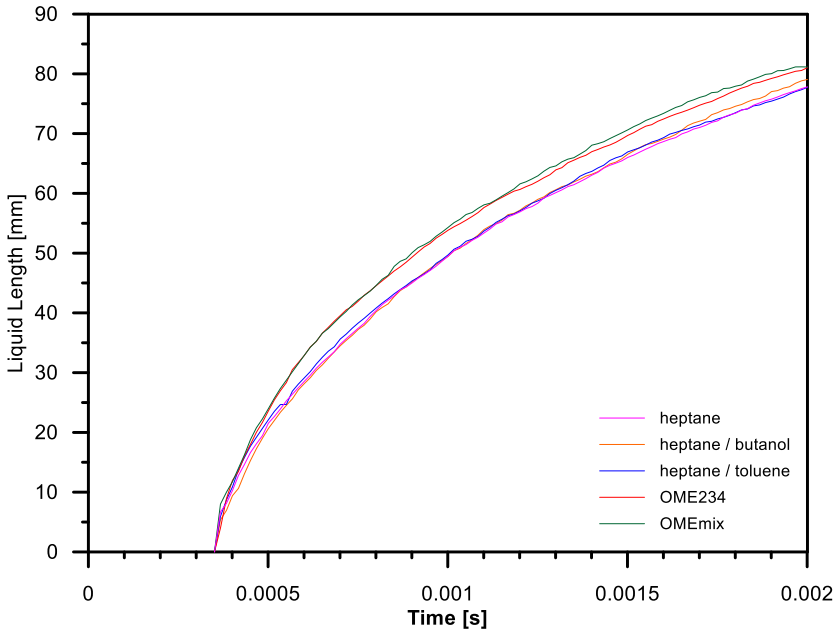


**Figure 54. Temporal evolution of vapour penetration, for all fuels at 900 K of ambient temperatures.**

### *Lift-off length and flame penetration*

The analysis of the flame base stabilization and penetration of the flame tip will be discussed in this section. As seen in Figure 49 the chemiluminescence of the OH* radical will be visible only after ignition. Following ignition, the flame base will stabilize a certain distance from the nozzle while the flame tip will penetrate along with the spray tip up to a distance where no more reactions are taking place.

Figure 55 shows the evolution of the flame penetration and the lift-off length for *n*-heptane at all temperatures. The trend of the lift-off length shows to be shorter as the ambient temperature increases; this is because the higher temperatures affect the flame speed and the thermal diffusivity [17, 51, 62-65]. Therefore, as the spray velocity is higher closer to the nozzle tip, the points at higher temperature and with higher flame speeds will stabilize closer to the nozzle, resulting in shorter lift-off lengths. On the other hand, the stabilized flame penetration seems to not be dependent on the ambient temperature, this is because the flame is defined by a stoichiometric surface, which in this case is constant as the fuel and air compositions are the same for all temperatures.

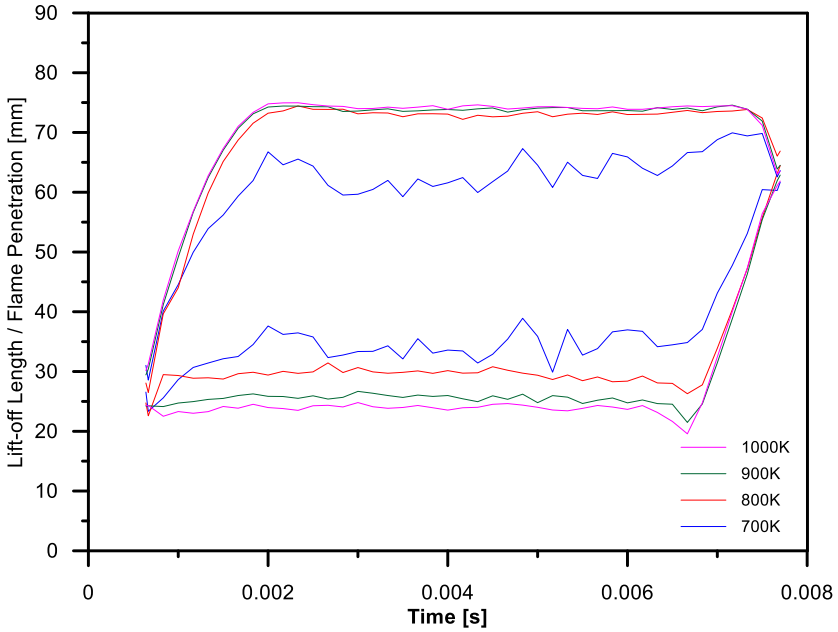


**Figure 55. Temporal evolution of lift-off length and flame penetration, for *n*-heptane at all ambient temperatures tested (700 K-1000 K).**

Figure 56 presents the evolution of the lift-off length and flame penetration for all fuels at 900 K of ambient temperature. In an analogous way as mentioned in the previous paragraph, the stoichiometric surface will define the flame region and stabilized flame penetration. Two trends are observable; one for the OME blends and another for the *n*-heptane blends. Since OME has a lower stoichiometric air-fuel ratio than *n*-heptane, its flame region will be smaller, resulting in shorter flame penetrations. Regarding the lift-off length, focusing for a moment only on the *n*-heptane blends, it can be seen that the addition of toluene makes them stabilize closer to the nozzle, while butanol will have a slightly longer lifted flame; this latter small change is due to the low concentration of butanol in the blend. While the OME blends present also similar lifted flames due to their similar composition, the OMEmix has a flame base that stabilizes closer to the nozzle tip than OME234.

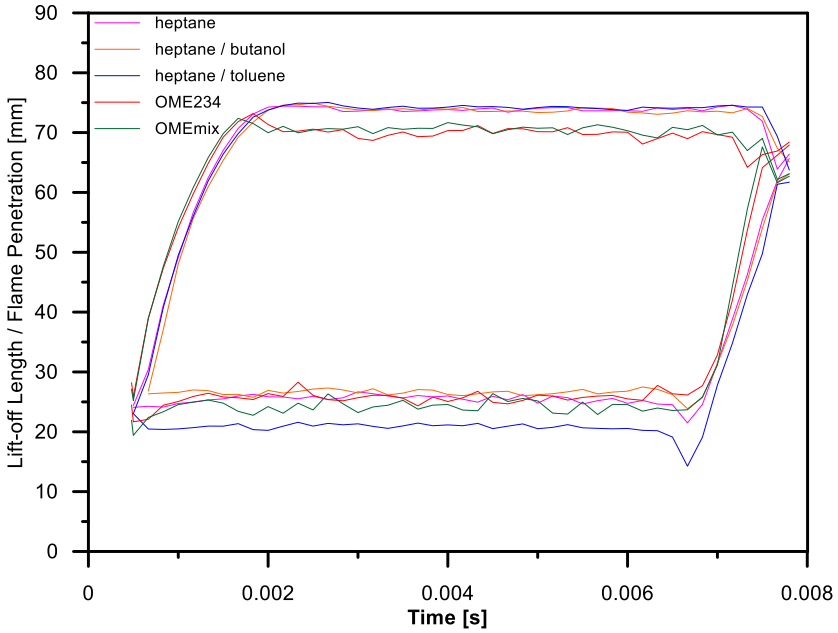


**Figure 56. Evolution of lift-off length and flame penetration for all fuels at 900 K ambient temperature.**

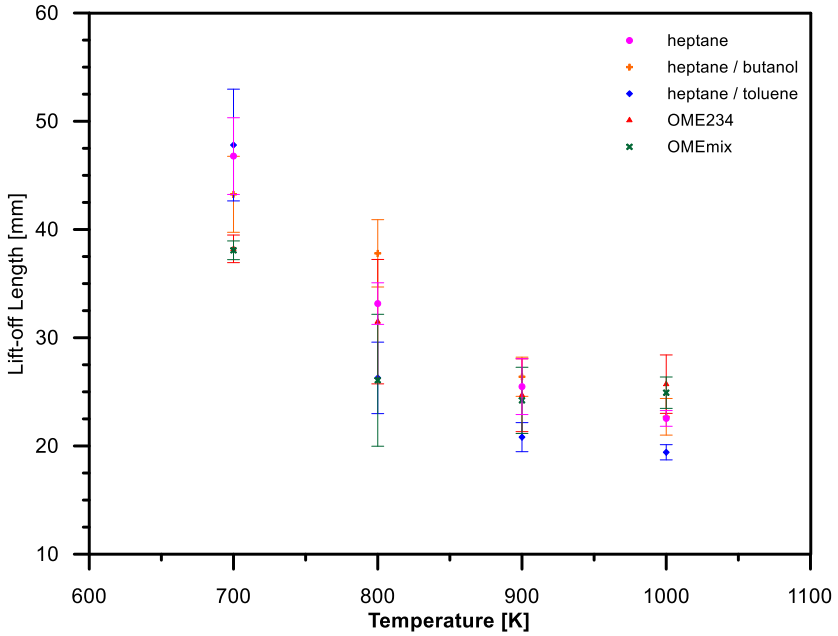


**Figure 57. Average values for lift-off length, for all fuels as a function of the ambient temperature.**

Figure 57 and Figure 58 present a summary of the aforementioned values, were the trends of the lifted flame bases and stabilized flame tips can be confirmed for all fuels and temperature combinations.

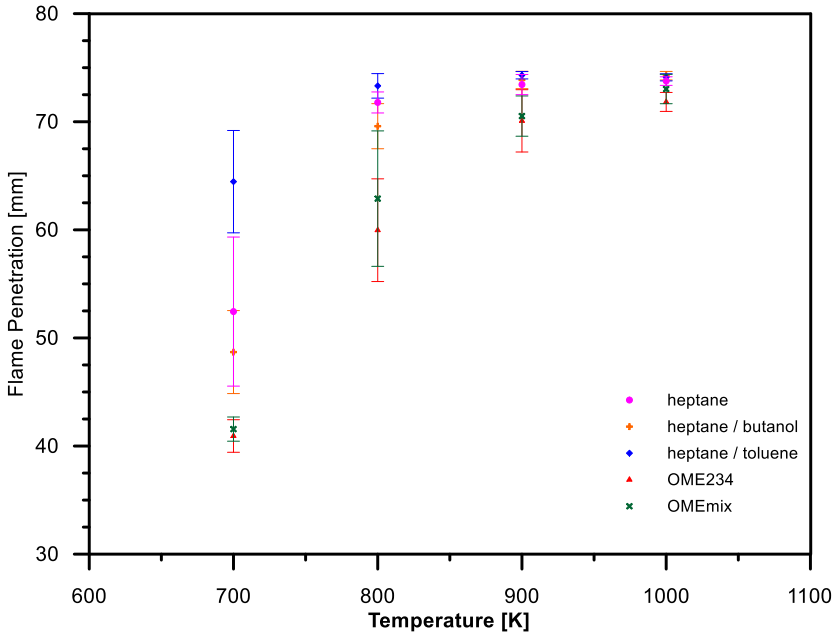


**Figure 58. Average values for flame penetration, for all fuels as a function of the ambient temperature.**

### *Soot concentration*

In this section, the results of the broadband radiation and 3-colour pyrometry measurments are presented. The OME blends generated a negligible amount soot and presented very little luminosity, and have been therefore excluded from the present analysis.

Figure 59 presents the luminosity emitted by the combustion of *n*-heptane at all four temperatures. The trend that can be observed is that a higher temperature resulted in a greater luminosity; this is because higher temperature causes the soot to emit a higher intensity of radiation, which is caused by the increased adiabatic flame temperature as an effect of the higher ambient temperature. However, it cannot be directly correlated to the soot amount, as the broadband radiation also contains light emitted by other

radicals present in the combustion. The amount of luminosity generated at 700 K ambient temperature is so low in comparison with the other three, and as such is excluded from the soot analysis.

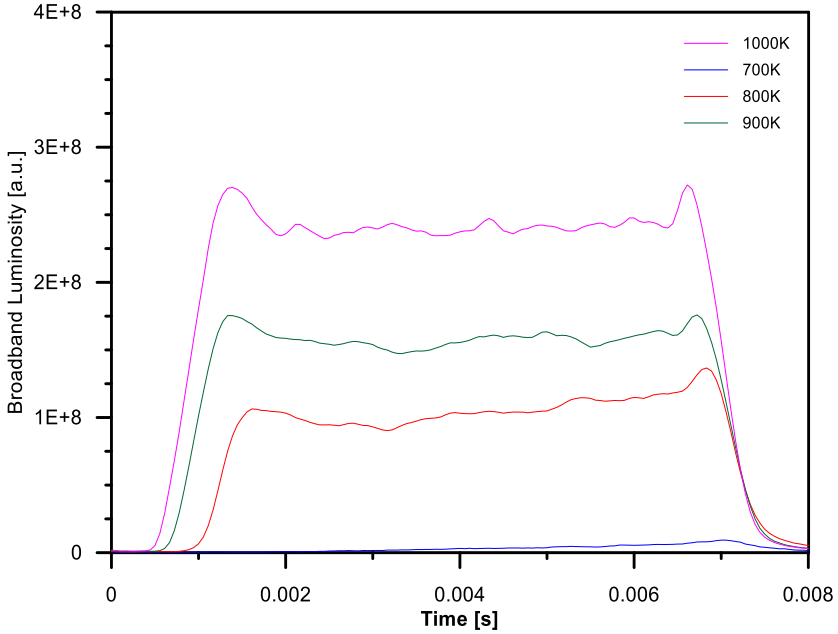


**Figure 59. Evolution of broadband luminosity for *n*-heptane at all ambient temperatures (700 K-1000 K).**

Figure 60 shows a trend that can compared to the lift-off length as shown in Figure 55. A stronger combustion, caused by an increased ambient temperature will result in higher flame speeds, resulting in shorter lifted flames, and brighter soot luminosity, this is the case for the *n*-heptane/toluene blend. The other extreme corresponds to the *n*-heptane/butanol blend, where the weaker combustion caused less luminosity to be emitted and a flame base to stabilize further away from the nozzle. Nevertheless, since the presence of *n*-heptane is so large in the blend, the results are close to the ones obtained with pure *n*-heptane.

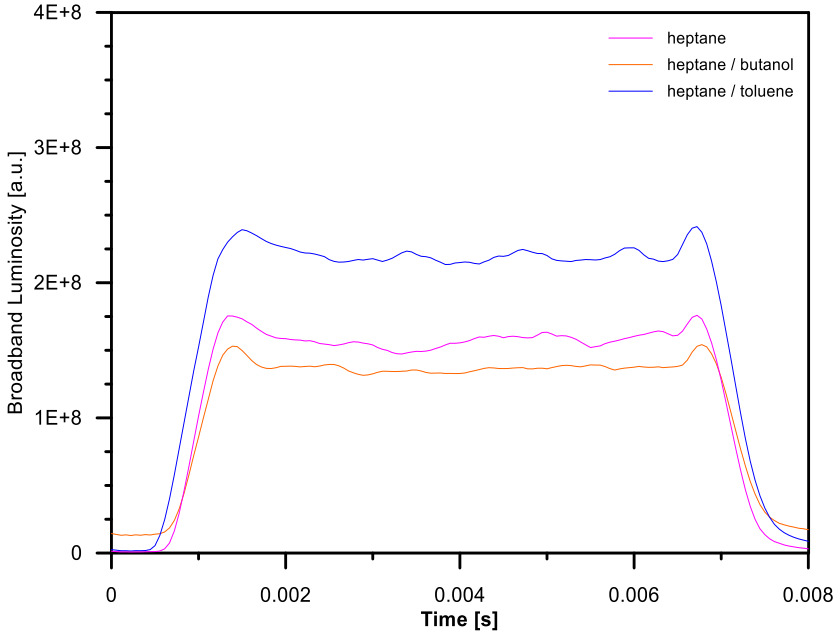


**Figure 60. Temporal evolution of broadband luminosity, for *n*-heptane blends at 900 K of ambient temperature.**

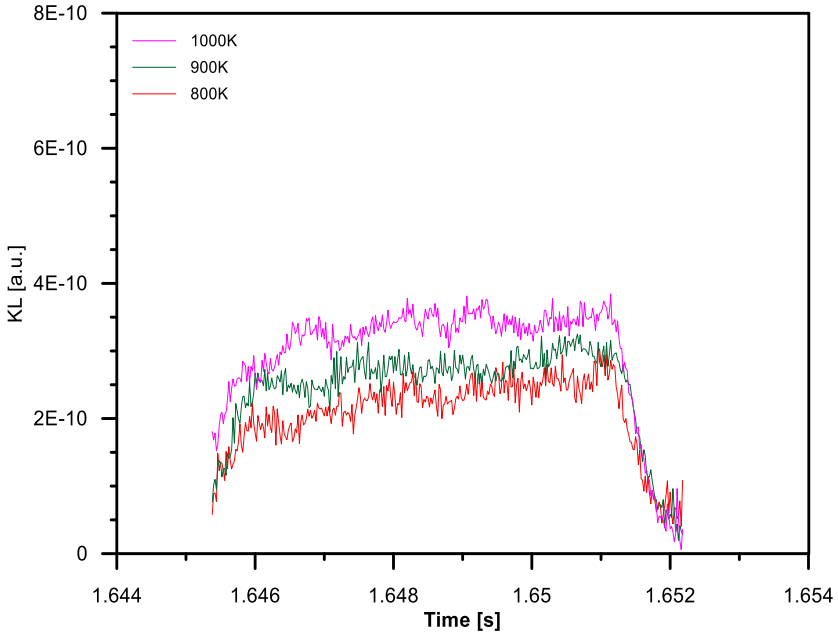


**Figure 61. Evolution of soot concentration (KL) for *n*-heptane at all ambient temperatures (700 K-1000 K).**

Figure 61 shows the amount of soot generated by the combustion of *n*-heptane at the three highest temperatures. As assumed in Figure 59, the points at higher temperatures do generate a higher amount of soot. On the contrary, the trend presented in Figure 62 is not the same as what was seen in Figure 60, where fuel that generated less soot was *n*-heptane instead of *n*-heptane /butanol, but the point with more soot generated does correspond to the point with most luminosity, which is caused by the combustion of the *n*-heptane/toluene blend. The soot luminosity depends on the temperature and the amount of soot within the flame; therefore, the same luminosity can be emitted by high temperature flame with low concentration soot and by a low temperature flame with high amounts of soot; proving that the broadband radiation method is only an indicative of the presence of soot, but not an accurate way to determine its quantity. The discrepancy between the trends seen in in Figure 62 and Figure 60 can be explained with the flame temperatures of each blend, since the toluene blend has a higher flame temperature than *n*-heptane, it will cause the soot to burn brighter and with a greater luminosity. On the other hand, since the butanol blend has a lower flame temperature than *n*-heptane, it will result in a combustion with less light emitted, even if the amount of soot present is higher.

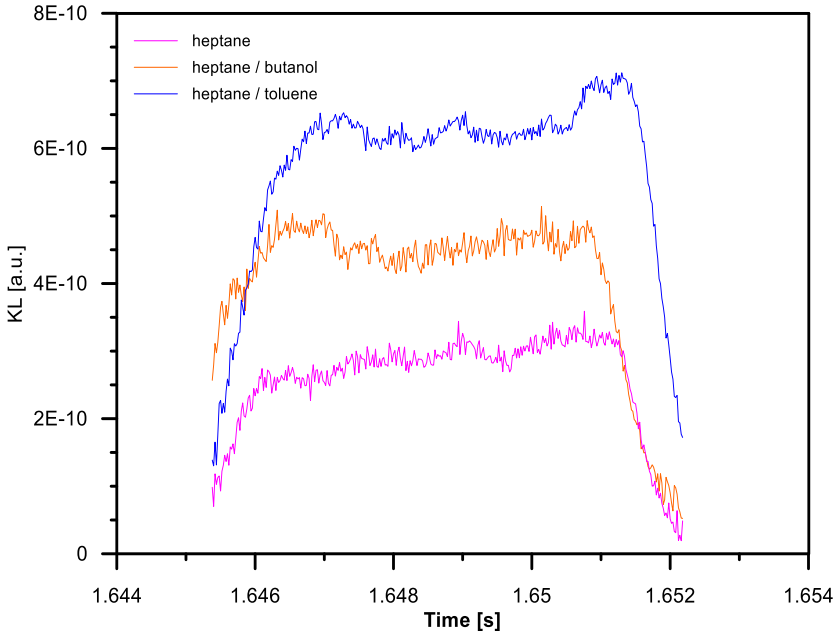


**Figure 62. Evolution of soot concentration (KL) for all fuels at 900 K ambient temperature.**

Figure 63 shows a summary of all the average KL values for the three *n*-heptane blends and the three highest temperatures.

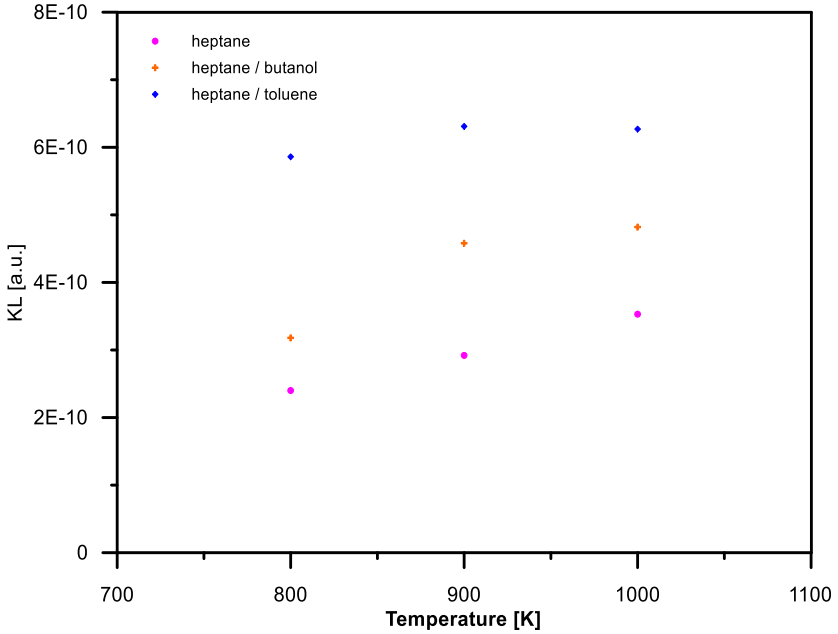


**Figure 63. Average values for soot intensity, for *n*-heptane blends at 900 K ambient temperature.**

### *Ignition delay time*

In order to define the ignition delay, [54] set a threshold value of OH* signal to lower than that of high-temperature chemiluminescence, but safely above that of the cool flame. Hence, an intensity threshold of 200 counts was chosen to define ignition. [66] chose the pixel counts above 300 as the threshold. In the present investigation similar methods for post-processing of OH* chemiluminescence were used. Firstly, a mask to cut the background and noise was defined. Then, the boundary of the mask was found, followed by a calculation of the area of the boundary. We defined the boundary area over 300 pixel as the ignition time in our work. For comparison with the present measurement campaign, the results from [54] and [66] are reproduced in Figure 64 and Figure 65, respectively. However, because different temperatures are investigated, the results cannot be compared directly.

The OH* chemiluminescence images of *n*-heptane acquired at 1000 K in this campaign can be seen in Figure 67. The time shown in Figure 67 is defined from the start of injection trigger. The hydraulic delay of our injector is around 0.35 ms. Therefore, the final ignition delay is around 0.317 ms, which is very close to the literature [54] for similar conditions and cetane number. However, if the area is too small, noise will greatly influence the results; therefore, a larger area is chosen as the start of ignition. The same analysis method is used to carry out the ignition delay with different fuels and different conditions (shown in Table 11). Because at 700 K, the OH* chemiluminescence signal is very weak and the gain of the intensifier is very high, a lot of noise is detected, so we cannot use this method to get the ignition delay correctly. The ignition delay calculated with the abovementioned method from the OH* chemiluminescence images for different fuels plotted vs temperature at constant density can be seen in Figure 66.

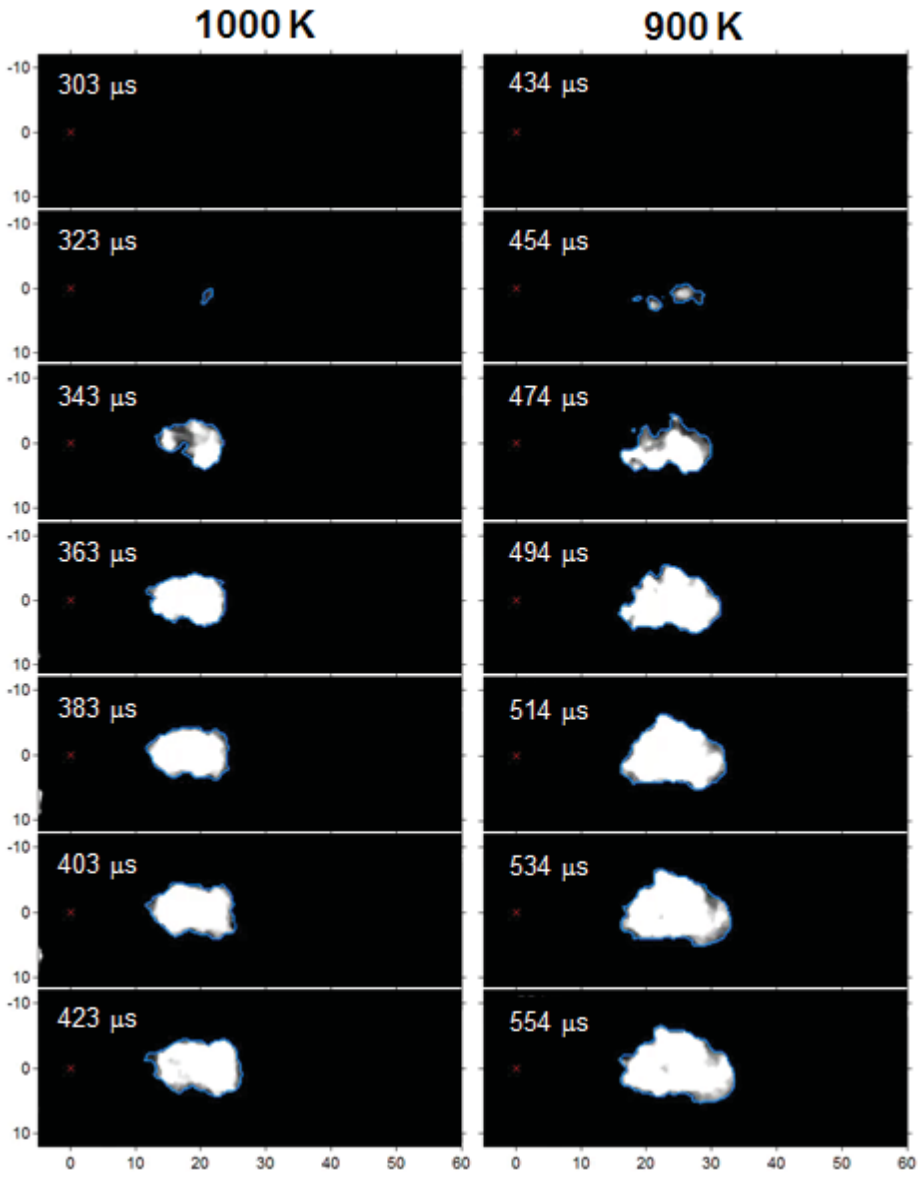


**Figure 64. Sequential images from [66] of the onset of high-temperature chemiluminescence during the ignition period for Plume 3. Bottom view collection using the monochromatic high-speed CMOS camera filtered < 600 nm. The ambient temperature is 1000 K (left column) and 900 K (right column).**

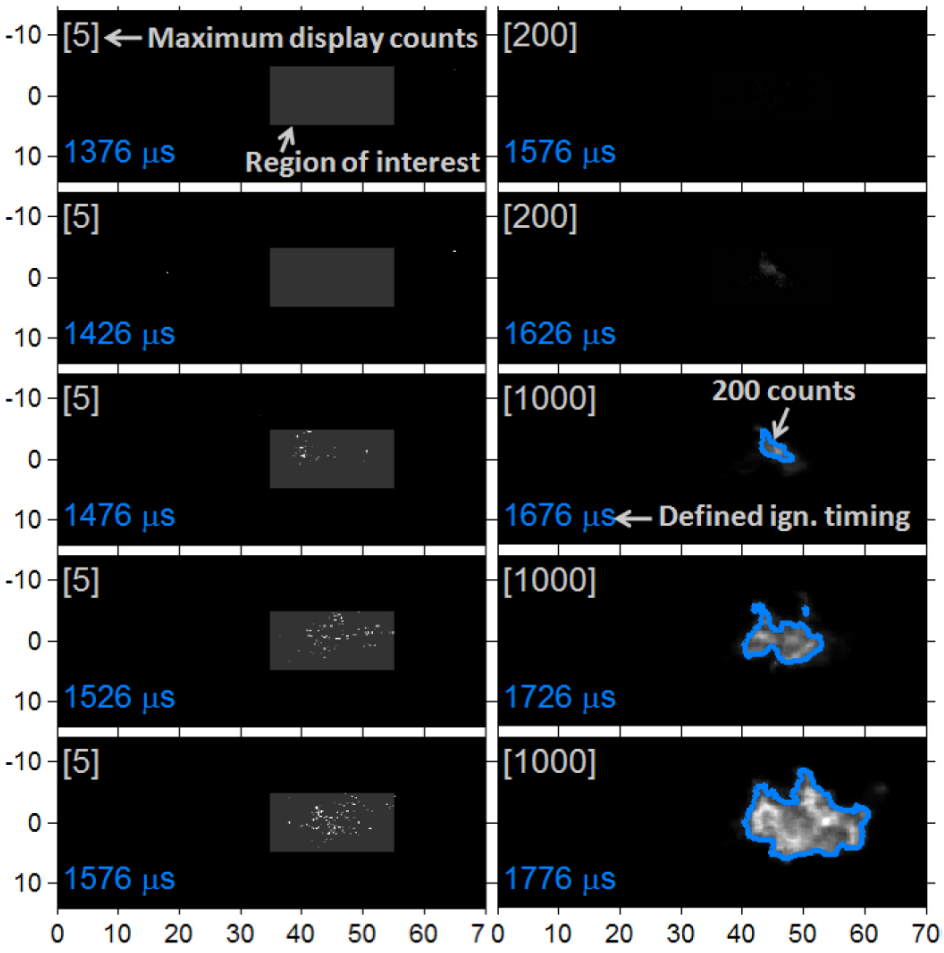


**Figure 65. Chemiluminescence images from [54] for the 750 K condition, test #3. High-temperature reactivity borders are shown in (blue). Relative image counts for display range is in brackets.**

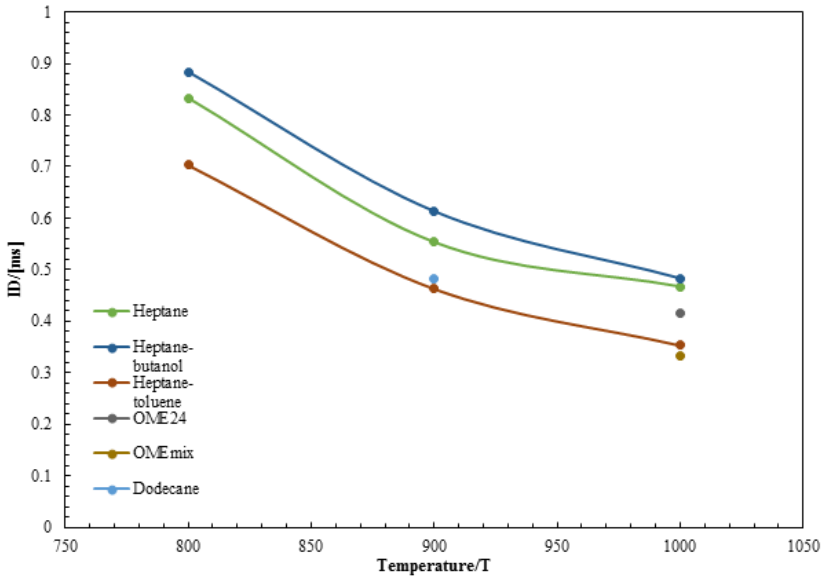


**Figure 66. OH* chemiluminescence of *n*-heptane at 1000 K condition.**

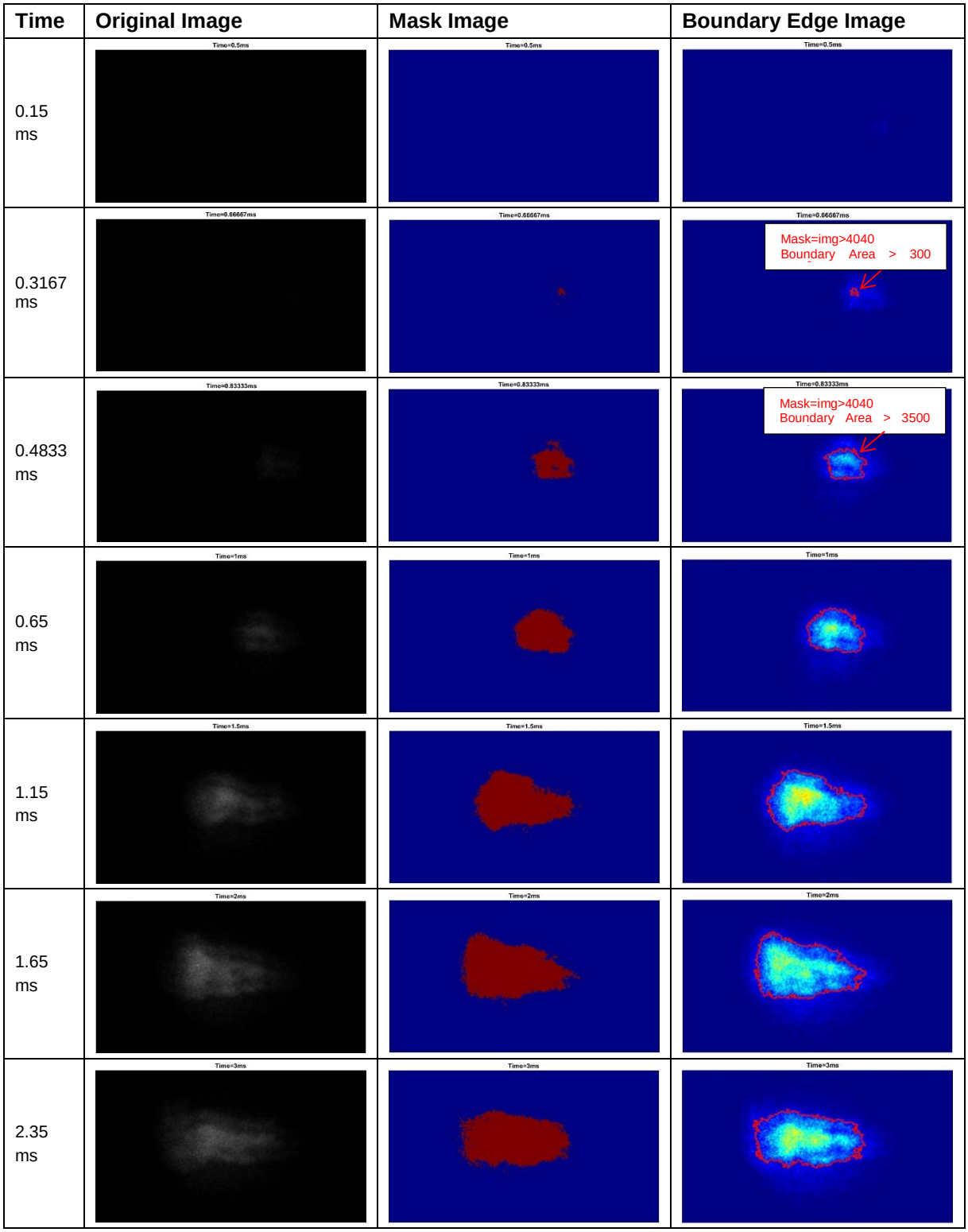


**Figure 67. OH* chemiluminescence of *n*-heptane at 1000 K condition**

## *WP4 summary and conclusions*

The aim of the investigations in WP4 was the experimental investigation of spray formation, ignition and soot formation/oxidation characteristics of different fuels under diesel engine conditions in a constant volume, high pressure and temperature, optically accessible combustion cell. To this end, the cell was adapted to include a hydrogen injection and ignition system, which allowed the gas temperture during the experiment to exceed 1000K. Purpose-built single-nozzle injectors were used for the investigations, which were designed for limitation of caviation and characterised in a Bosch tube in terms of injection

rate prior to the experiments in the cell. Simultaneous high-speed OH* chemiluminescense, Schlieren imaging and Mie-scattering were applied in order to determine spray liquid and vapour penetration, ignition timing and location as well as lift-off length. Temporally resolved soot concentration and temperature were obtained using the measurement of broadband radiation and using the 3-colour pyrometry method. In total 5 different fuels were tested, each at 4 different ambient gas temepratures and constant density.

The results showed that:

- Liquid penetration reduces with increasing ambient temperature and with decreasing latent heat of evaporation of the fuel
- Vapour penetration is only affected by the ambient density and the momentum of the fuel. At constant density, the penetration increases slightly after ignition due to the expansion of the gases, leading to a preparation of the vapour penetration curves for different ambient temperatures and thus ignition delays. With increasing fuel density, the vapour penetration at constant injection pressure increases due to the increase in the momentum of the spray.
- The lift-off length decreases with increasing ambient reactivity (temperature) as expected. The heptane/toluene blend showed the shortest lift-off length for high temperatures, while all other fuels showed similar values between them. Under low temperature conditions the OMEs showed the shortest lift-off lengths
- Soot concentration was shown to increase with increasing temperature due to the higher formation rate, as expected. Neat heptane showed the lowest soot concentration between the heptane blends. The oxygenated fuel blends showed no measureable soot at all conditions.
- Ignition delay decreased with increasing temperature as expected, and the measured values were very close to those found in the literature for similar conditions for heptane [54]. The OME fuels showed higher reactivity (lower ignition delay) than the heptane blends for all ambient temperatures,

# Technology transfer (WP5)

Work is ongoing to improve the code usability, modularity and flexibility. This includes in particular the development of scripts, which parse arbitrary chemistries in CHEMKIN format and provide input scripts for the STAR-CD pre-processor PROSTAR. The latter is especially useful for larger surrogate kinetics with large numbers of species and polynomial coefficients for the respective $c_p$ which need to be defined.

### *Computational improvements – In Situ Adaptive Tabulation (ISAT)*

To reduce the computational expense, the so-called In-Situ Adaptive Tabulation (ISAT) technique from [67] has been implemented and first tested in the stand-alone CMC code using the Luo et al. mechanism [37]. Calculations for auto-igniting flamelets starting from frozen mixing at “reference” conditions, i.e. 1000 K air (21 percent oxygen content) and 373 K fuel temperature boundaries at 42.5 bar at a peak conditional scalar dissipation rate of 10 $s^{-1}$ have shown a speed-up by a factor of ten (calculation times of 7,007.3 vs. 1,662.5 seconds up to ignition and 35.9 vs. 2.33 CPU hours for 0.72 ms integration time).

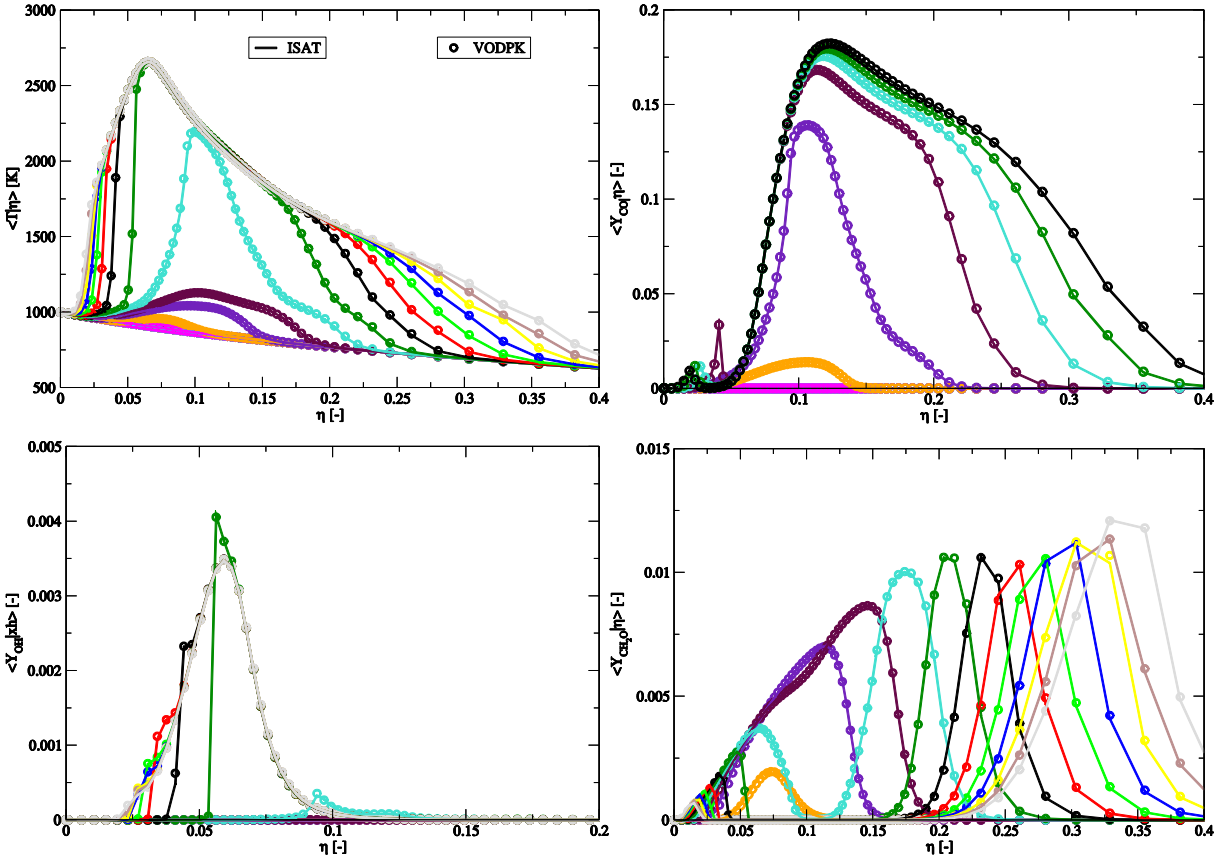


**Figure 68: Time evolutions of conditional temperature (upper left) and conditional mass fractions of CO (upper right), OH (lower left) and $CH_2O$ (lower right) for an auto-igniting n-dodecane flamelet. Solid lines are for the ISAT tabulation procedure, symbols for conventional integration by means of VODPK. $T_{air}$ = 1000 K, $T_{fuel}$=373 K, pressure = 42.5 bar and conditional scalar dissipation rate <N|η=0.5>=10 $s^{-1}$**

The predictions from the conventional integrator (DVODPK, [68], used in all former studies so far) are compared to the results obtained with ISAT in Figure 68 for the evolution of conditional temperature and conditional mass fractions of CO as well as of two radicals, namely formaldehyde (an ignition marker) and OH (high temperature tracer). It is evident that the results can be considered virtually identical, in view of the good agreement also of radical species, especially during the rapid transition at the time of ignition.

Given the good agreement between the tabulation technique and integration by means of VODPK and also the substantially reduced calculation time, ignition delays could subsequently be computed for a wide range of scalar dissipation rates and compared to previously obtained values for *n-heptane*, cf. Figure 69 below. As expected due to the higher cetane number, the ignition delays are considerably shorter for *n*-dodecane over the entire range. The critical strain rate, above which ignition can no longer occur is almost twice as high as for *n*-heptane.

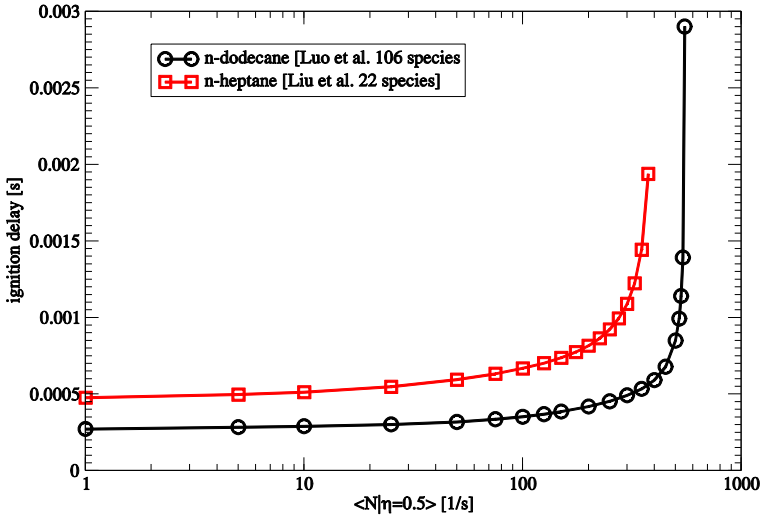


**Figure 69: ignition delay of n-dodecane (Luo chemistry) for different scalar dissipation rates compared to n-heptane chemistry from [18]**

In addition to these stand-alone ISAT calculations and comparisons for *n*-dodecane, ISAT has also been successfully interfaced with the STAR-CD/CMC code enabling full spray calculations. In a first step, the performance has been assessed using the Liu et al. [18] 44 species chemistry for *n*-heptane for a test-case from [11]. The chosen conditions are 21% $O_2$, 1000 K and 42 bar with an orifice diameter of 0.1 mm, an injection pressure of 1,500 bar and quasi-steady injection.

As can be seen from the pressure rate of change given in Figure 70, both approaches over-predict the ignition delay at this density, consistent with findings reported in Figure 1 above. The evolution following auto-ignition exhibiting multiple spikes (corresponding to different CMC nodes igniting) is very comparable between both approaches.

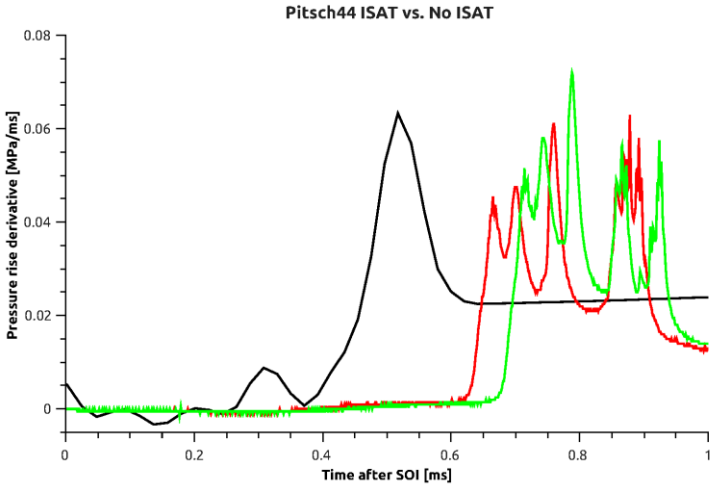


**Figure 70: comparison of pressure rate of change using ISAT tabulation with default and tighter tolerances versus classical time integration using the stiff integrator VODPK compared to the experimental data.**

The slightly earlier ignition when using ISAT can also be seen in the spatial distributions of the temperature shown in Figure 71; spatially, ignition is however predicted at the same location when making use of the tabulation technique. Following ignition, the flame rapidly engulfs the available premixed fuel and propagates also upstream against the incoming jet towards the injector until it

stabilises at the lift-off length. Although the distributions at 0.8 ms are not fully stabilised yet, the temperature distributions between the ISAT tabulation technique and the VODPK predictions agree very well further supporting the use of this approach for the calculation of auto-igniting fuel sprays.

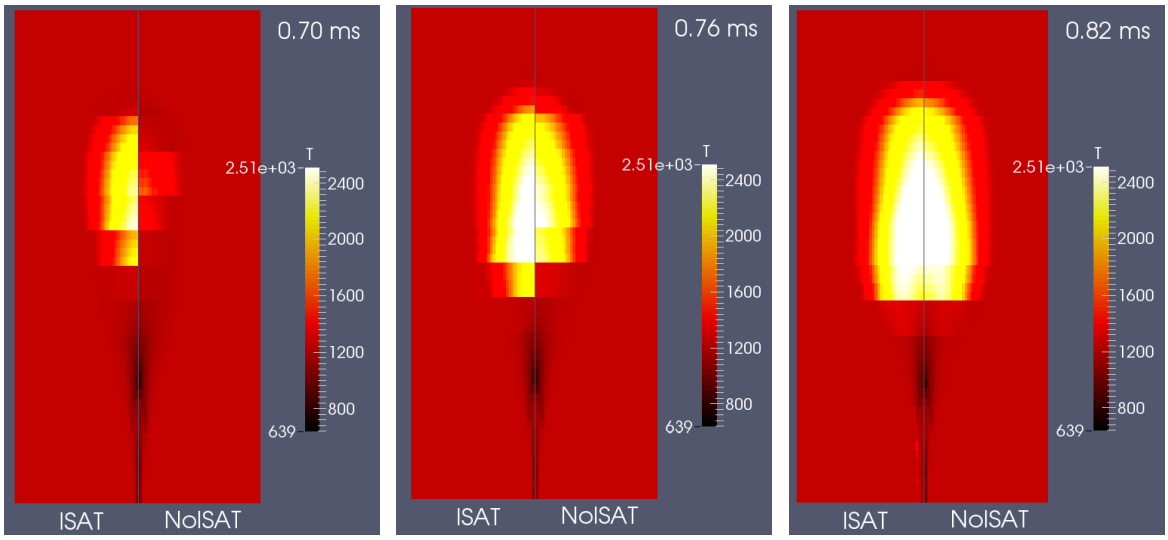


**Figure 71: comparison of spatial distribution of temperature at three different time instances: 0.70 ms (left), 0.76 ms (middle) and 0.82 ms (right) in a section through the spray axis using ISAT tabulation with default and tighter tolerances versus classical time integration using the stiff integrator VODPK.**

The computational time needed per time step is presented in Figure 72 below. In the early phase, the table for ISAT does not exist yet and needs to be built “in situ”. ISAT uses its own integrator (DDASAC) for time integration to do so, therefore the computational expense of the two approaches are very similar. From around 0.3 ms onwards, the tabulation however starts to retrieve already computed values and an increasing deviation between VODPK and ISAT starts to become evident up to roughly 680 time steps, when ignition occurs.

Following the ignition, the difference in the wall time needed per time step become very significant and amounts to roughly a factor of 15 throughout the remaining calculation.

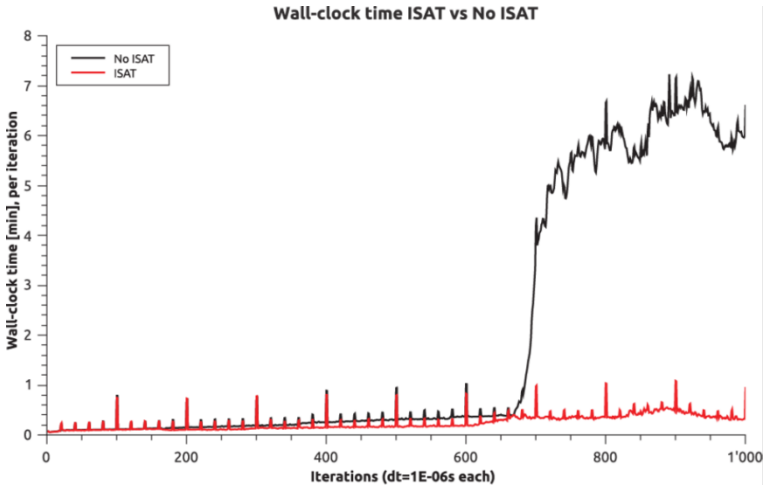


**Figure 72: comparison of wall time per integration step using ISAT tabulation with default tolerances versus classical time integration using the stiff integrator VODPK.**

While the result presented relate to the skeletal *n*-heptane kinetics from [18] with 44 species, the speed-up obtained is very important in view of the larger kinetics required e.g. for longer chain paraffinic fuels (XTL), oxygenated compounds and kinetics including substantial soot precursor sub-mechanisms.

For the *n*-dodecane kinetics of Luo et al. [37], a speed-up of roughly an order of magnitude in computational time was observed. The implementation of ISAT into the CMC code can therefore be considered a prerequisite with respect to efficient application of the developed platform to “Spray A” (cf. *n*-dodecane results reported for **WP2** above) and in view of its use in conjunction with other larger detailed kinetics.

### *Computational improvements – user coded fuel database*

A user coded fuel library has been developed, which includes thermophysical droplet properties for density, viscosity, surface tension, vapour pressure, latent heat, heat capacity and conductivity as functions of temperature.

Fuels added specifically within this project include methyl decanoate from NIST data, for which the origins of the data sources are clearly documented within the source code.

Extension of the database for new/additional fuels can readily be done since the source code is available.

### *Workflow improvements*

Scripts have been developed which parse the CHEMKIN chemical kinetics and species thermophysical data input files for automated generation of CFD solver pre-processor input. This ensures rapid and efficient script based setup of simulation setups and minimizes potential user errors.

# Dissemination of results (WP6)

The vast majority of achieved results have been accepted for publication in Journals [5, 12, 16, 21, 23, 24, 29, 42], peer reviewed conference proceedings [19, 20, 25, 28, 30] or presented in the ERCOFTAC September 2013 issue bulletin.

In addition to the attendance of events listed below, a selection of results has further been presented at the following invited/guest talks:

- “Modelling spray combustion with Conditional Moment Closure - a review”, *invited talk at the University of British Columbia,* 26th July 2013, Vancouver, Canada.
- “Experiments and modelling activities at LAV, ETH Zurich”, *Invited seminar at Centro Motores Térmicos (CMT) Universitat Politècnica de València*, 9th September 2014, Valencia, Spain.
- “Flow, Turbulence and Combustion – DNS, LES and RANS applied in the IC engine context”, *Invited research seminar at Loughborough University*, 24th October 2014, Loughborough, UK.
- “Modelling soot formation in Diesel engines with Conditional Moment Closure – effects of SOI, EGR and post-injection”, *guest talk at the final workshop of EU FP7 project* “FIRST”, 19th/20th November 2014, Derby, UK.

### *Networking*

### Events attended

- Society of Automotive Engineers, 11th International Conference on Engines & Vehicles, Capri, Napoli (Italy) 15th – 19th September 2013

- Swiss Federal Office of Energy “Swiss combustion research day 2013, ETH Zurich, Switzerland, 6th November 2013
- International Energy Agency 34th Task Leader Meeting on Energy Conservation and Emissions Reduction in Combustion, San Francisco, U.S.A., 21st – 25th July 2013
- Engine Combustion Network workshop 3 meeting, Ann Arbor, U.S.A., 4th/5th April 2014
- IEA TCP Combustion, Spray Collaborative Task workshop, Detroit, U.S.A. 7th April 2014
- International Multidimensional Engine Modelling User's Group Meeting, Detroit, U.S.A. 7th April 2014
- Society of Automotive Engineers, World Congress, Detroit, MI, 8th – 10th April 2014
- International Energy Agency 36th Task Leader Meeting on Energy Conservation and Emissions Reduction in Combustion, Stavanger, Norway, 9th – 13th June 2014
- “THIESEL” conference, Centro Motores Térmicos (CMT) Universitat Politècnica de València, Spain, 8th-12th September 2014
- ERCOFTAC “ETMM10” conference, Marbella, Spain, 17th – 19th September 2014
- Society of Automotive Engineers, Powertrains Fuels and Lubricants meeting, Birmingham, UK, 20th – 22nd October 2014
- “LES4ICE” 2014 workshop, Rueil-Malmaison, France, 3rd – 5th December 2014
- Mediterranean combustion Symposium, Rhodes, Greece, 7th – 11th June 2015
- International Energy Agency 37th Task Leader Meeting on Energy Conservation and Emissions Reduction in Combustion, St. Andrews, UK, 2nd – 5th August 2015
- Swiss Federal Office of Energy “Swiss combustion research day 2015, ETH Zurich, Switzerland, 9th September 2015
- Society of Automotive Engineers, 12th International Conference on Engines & Vehicles, Capri, Napoli (Italy) 13th – 17th September 2015
- IEA TCP Combustion, Spray Collaborative Task workshop, Detroit, U.S.A. 11th April 2016
- International Multidimensional Engine Modelling User's Group Meeting, Detroit, U.S.A. 11th April 2016
- Society of Automotive Engineers, World Congress, Detroit, 12th – 14th April 2016
- International Energy Agency 38th Task Leader Meeting on Energy Conservation and Emissions Reduction in Combustion, Ruka, Finnland, 26th June – 1st July 2016
- Premixed Turbulent Flames workshop, Incheon, Korea, 29th/30th July 2016
- International Symposium on Combustion, Seoul, Korea, 31st July – 6th August 2016
- CMC/MMC workshop, Seoul, Korea, 7th August 2016
- “THIESEL” conference, Centro Motores Térmicos (CMT) Universitat Politècnica de València, Spain, 13th-16th September 2016
- ERCOFTAC “ETMM11” conference, Palermo, Italy, 20th – 24th September 2016
- Society of Automotive Engineers, Powertrains Fuels and Lubricants meeting, Baltimore, U.S.A., 24th – 26th October 2016
- “LES4ICE” 2016 workshop, Rueil-Malmaison, France, 31st November – 1st December 2016
- Engine Combustion Network: ECN5 workshop, Wayne State University, Detroit, U.S.A. 31st March – 1st April 2017
- IEA TCP Combustion, Spray Collaborative Task workshop, Detroit, U.S.A., 3rd April 2017
- International Multidimensional Engine Modelling User's Group Meeting, Detroit, U.S.A. , 3rd April 2017
- Society of Automotive Engineers, World Congress, Detroit, 4th – 6th April 2017

## Contacts

- Dr. Paul Miles, Sandia National Laboratories, Livermore, U.S.A.
- Dr. Mark Musculus, Sandia National Laboratories, Livermore, U.S.A.
- Dr. Lyle Pickett, Sandia National Laboratories, Livermore, U.S.A.
- Dr. Scott Skeen, Sandia National Laboratories, Livermore, U.S.A.
- Prof. Jacqueline Chen, Sandia National Laboratories, Livermore, U.S.A.

- Dr. Hemanth Kolla, Sandia National Laboratories, Livermore, U.S.A.
- Dr. Julien Manin, Sandia National Laboratories, Livermore, U.S.A.
- Dr. Magnus Sjöberg, Sandia National Laboratories, Livermore, U.S.A.
- Dr. Xandra Margot, Centro Motores Termicos, University of Valencia, Spain
- Prof. Raoul Payri, Centro Motores Termicos, University of Valencia, Spain
- Prof. Jose-Maria García, Centro Motores Termicos, University of Valencia, Spain
- Prof. Edward Richardson, University of Southampton, UK
- Prof. Peter Lindstedt, Imperial College, London, UK
- Prof. Evatt Hawkes, University of New South Wales, Australia
- Prof. Andrei Lipatnikov, Chalmers University, Sweden
- Prof. Tim Lieuwen, Georgia Tech., U.S.A.
- Prof. James F. Driscoll, University of Michigan, U.S.A.
- Prof. Will Northrop, University of Minnesota, U.S.A.
- Prof. Hong Im, Clean Combustion Research Center, KAUST, Saudi-Arabia
- Dr. Konstantina Vogiatzaki, City University London, UK
- Dr. Andrew Garmory, University of Loughborough, UK
- Dr. Gary Page, University of Loughborough, UK
- Dr. Graham Wigley, University of Loughborough, UK
- Dr. Sibendu Som, Argonne National Laboratoires, U.S.A.
- Dr. Yuanjiang Pei, Argonne National Laboratories, U.S.A.
- Dr. Scott Goldsborough, Argonne National Laboratories, U.S.A.
- Dr. Steve Ciatti, Argonne National Laboratories, U.S.A.
- Dr. Chris Powell, Argonne National Laboratories, U.S.A.
- Dr. Paul Fischer, Argonne National Laboratories, U.S.A.
- Dr. Douglas Longman, Argonne National Laboratories, U.S.A.
- Dr. Chad Koci, Dr. Tim Bazyn, Caterpillar Inc., U.S.A.
- Dr. Fridolin Unfug, MAN, Germany
- Prof. Kyoungdoug Min, Seoul National University, Korea

# References


1. Wright, Y.M., et al. *Conditional Moment Closure For Two-Phase Flows – A Review Of Recent Developments And Application To Various Spray Combustion Configurations*. in *proceedings of the 8th International Conference of Computational Methods in Sciences and Engineering (ICCMSE-2010)*. 2010. Kos, Greece: AIP Conf. Proc.
2. Wright, Y.M., et al., *Simulations of spray autoignition and flame establishment with two-dimensional CMC.* Combustion and Flame, 2005. **143**(4): p. 402-419.
3. Wright, Y.M., et al., *Experiments and Simulations of n-Heptane Spray Auto-Ignition in a Closed Combustion Chamber at Diesel Engine Conditions.* Flow Turbulence and Combustion, 2010. **84**(1): p. 49-78.
4. Koss, H.J., et al., *Investigations of the Influence of Turbulence and Type of Fuel on the Evaporation and Mixture Formation in Fuel Sprays*. 1992: Final Report of JOULE Project on Integrated Diesel European Action (IDEA).
5. Bolla, M., et al., *Soot Formation Modeling of n-Heptane Sprays Under Diesel Engine Conditions Using the Conditional Moment Closure Approach.* Combustion Science and Technology, 2013. **185**(5): p. 766-793.
6. Schlatter, S., et al., *3D-CRFD Combustion Modeling of Gas Engines with Pilot Injection.* Proceedings of the 7th Dessau Gas Engine Conference, 2011.
7. Schlatter, S., et al., *Experimental Study of Ignition and Combustion Characteristics of a Diesel Pilot Spray in a Lean Premixed Methane/Air Charge using a Single Stroke Machine.* SAE Technical Paper No. 2012-01-0825, 2012.
8. De Paola, G., et al., *Diesel engine simulations with multi-dimensional conditional moment closure.* Combustion Science and Technology, 2008. **180**(5): p. 883-899.
9. Wright, Y.M., et al., *Multi-dimensional Conditional Moment Closure Modelling Applied to a Heavy-duty Common-rail Diesel Engine.* SAE International Journal of Engines, 2009. **2**(1): p. 714-726.
10. Bertola, A.G., *Technologies for lowest NOx and particulate emissions in DI-diesel engine combustion. influence of injection parameters, EGR and fuel composition*. 2004, ETH Zürich.
11. Pickett, L.M., *Engine Combustion Network.* http://www.sandia.gov/ecn/dieselSprayCombustion.php, 2013.
12. Bolla, M., et al., *Simulations of Diesel Sprays Using the Conditional Moment Closure Model.* SAE International Journal of Engines, 2013. **6**(2): p. 1249-1261.
13. D'Errico, G., et al., *Comparison of well-mixed and multiple representative interactive flamelet approaches for diesel spray combustion modelling.* Combustion Theory and Modelling, 2014. **18**(1): p. 65-88.
14. Skeen, S.A., et al., *A Progress Review on Soot Experiments and Modeling in the Engine Combustion Network (ECN).* SAE Int. J. Engines, 2016. **9**(2): p. 883-898.
15. Idicheria, C.A. and L.M. Pickett, *Ignition, soot formation, and end-of-combustion transients in diesel combustion under high-EGR conditions.* International Journal of Engine Research, 2011. **12**(4): p. 376-392.
16. Bolla, M., et al., *Influence of turbulence–chemistry interaction for n-heptane spray combustion under diesel engine conditions with emphasis on soot formation and oxidation.* Combustion Theory and Modelling, 2014. **18**(2): p. 330-360.
17. Siebers, D. and B. Higgins, *Flame lift-off on direct-injection diesel sprays under quiescent conditions.* SAE Technical Paper No. 2001-01-0530, 2001.
18. Liu, S.L., et al., *Effects of strain rate on high-pressure nonpremixed n-heptane autoignition in counterflow.* Combustion and Flame, 2004. **137**(3): p. 320-339.
19. Bolla, M., et al., *Influence of Injector Diameter (0.2-1.2 mm range) on Diesel Spray Combustion: Measurements and CFD Simulations.* SAE Technical Paper No. 2014-01-1419, 2014.
20. Srna, A., et al., *CMC Model Applied to Marine Diesel Spray Combustion: Influence of Fuel Evaporation Terms.* SAE Technical Paper No. 2014-01-2738, 2014(2014-01-2738).
21. Farrace, D., et al., *Predicting In-Cylinder Soot in a Heavy-Duty Diesel Engine for Variations in SOI and TDC Temperature Using the Conditional Moment Closure Model.* SAE International Journal of Engines, 2013. **6**(3): p. 1580-1593.
22. Huestis, E., P.A. Erickson, and M.P.B. Musculus, *In-Cylinder and Exhaust Soot in Low-Temperature Combustion Using a Wide-Range of EGR in a Heavy-Duty Diesel Engine.* SAE Technical Paper No. 2007-01-4017, 2007.

23. Bolla, M., et al., *Modelling of soot formation in a heavy-duty diesel engine with conditional moment closure.* Fuel, 2014. **117**: p. 309-325.
24. Farrace, D., et al., *Numerical Study of the Influence of EGR on In-Cylinder Soot Characteristics in a Heavy-Duty Diesel Engine using CMC.* SAE International Journal of Engines, 2014. **7**(1): p. 256-268.
25. Bolla, M., et al., *An Extended CMC Model for the Simulation of Diesel Engines with Multiple Injections*, in *International Multidimensional Engine Modeling Users' Group Meeting*. 2014: Detroit, Michigan.
26. Bobba, M.K., M.P.B. Musculus, and W. Neel, *Effect of Post Injections on In-Cylinder and Exhaust Soot for Low-Temperature Combustion in a Heavy-Duty Diesel Engine.* SAE Technical Paper No. 2010-01-0612, 2010.
27. O'Connor, J. and M. Musculus, *Effects of exhaust gas recirculation and load on soot in a heavy-duty optical diesel engine with close-coupled post injections for high-efficiency combustion phasing.* International Journal of Engine Research, 2014. **15**(4): p. 421-443.
28. Frapolli, N., et al., *Simulations of In-Cylinder Processes in a Diesel Engine Operated with Post-Injections using an Extended CMC Model.* SAE Technical Paper No. 2014-01-2571, 2014.
29. Pandurangi, S.S., et al., *Influence of EGR on Post-Injection Effectiveness in a Heavy-Duty Diesel Engine Fuelled with n-Heptane.* SAE International Journal of Engines, 2014. **7**(4): p. 1851-1862.
30. Barro, C., et al., *THE Post Injection: Coalescence of 3D CFD-CMC Simulation, 2D Visualizations in a Constant Volume Chamber and Application in a Modern Passenger Car Diesel Engine.* SAE Technical Paper No. 2015-24-2515, 2015.
31. Vishwanathan, G. and R.D. Reitz, *Modeling Soot Formation Using Reduced Polycyclic Aromatic Hydrocarbon Chemistry in n-Heptane Lifted Flames With Application to Low Temperature Combustion.* Journal of Engineering for Gas Turbines and Power-Transactions of the ASME, 2009. **131**(3).
32. Blomberg, C., et al., *Final report on project "Characterisation of high boiling point/synthetic fuels for HCCI and partially stratified Diesel engine combustion by means of optical experiments and global reaction models"*. 2015: Swiss Federal Office of Energy, grant no. SI/500801-01.
33. Wang, H., et al., *Development of an n-heptane-n-butanol-PAH mechanism and its application for combustion and soot prediction.* Combustion and Flame, 2013. **160**(3): p. 504-519.
34. Brakora, J.L., Y. Ra, and R.D. Reitz, *Combustion Model for Biodiesel-Fueled Engine Simulations using Realistic Chemistry and Physical Properties.* SAE International Journal of Engines, 2011. **4**(1): p. 931-947.
35. Luo, Z., et al., *A reduced mechanism for biodiesel surrogates for compression ignition engine applications.* Fuel, 2012. **99**(0): p. 143-153.
36. Herbinet, O., W.J. Pitz, and C.K. Westbrook, *Detailed chemical kinetic oxidation mechanism for a biodiesel surrogate.* Combustion and Flame, 2008. **154**(3): p. 507-528.
37. Luo, Z., et al., *Development and validation of an n-dodecane skeletal mechanism for spray combustion applications.* Combustion Theory and Modelling, 2014. **18**(2): p. 187-203.
38. Narayanaswamy, K., P. Pepiot, and H. Pitsch, *A chemical mechanism for low to high temperature oxidation of n-dodecane as a component of transportation fuel surrogates.* Combustion and Flame, (0).
39. Vasu, S.S., et al., *n-Dodecane oxidation at high-pressures: Measurements of ignition delay times and OH concentration time-histories.* Proceedings of the Combustion Institute, 2009. **32**(1): p. 173-180.
40. Pole, S. and W. Cheng, *Statistical calculations of spherical turbulent flames.* Symposium (International) on Combustion, 1988. **21**(1): p. 1473-1481.
41. Petersen, B.R., *Transient High-Pressure Hydrogen Jet Measurements*. 2006, University of Wisconsin.
42. Pandurangi, S.S., et al., *Onset and progression of soot in high-pressure n-dodecane sprays under diesel engine conditions.* International Journal of Engine Research, 2016. **18**(5-6): p. 436-452.
43. Vandersickel, A., Y.M. Wright, and K. Boulouchos, *Global reaction mechanism for the auto-ignition of full boiling range gasoline and kerosene fuels.* Combustion Theory and Modelling, 2013. **17**(6): p. 1020-1052.
44. Wright, Y.M., et al., *Annual report project "3D-CRFD models for low CO2/low-emission mixing controlled combustion of biogenic/synthetic fuels in engines based on detailed reaction kinetics"*. 2012: Swiss Federal Office of Energy, grant no. SI/500818-01.

45. Göldner, M., et al., *HCCI Combustion Using Engine Fuels with and without Oxygenated Compounds.* MTZ worldwide, 2017. **78**(4): p. 74-79.
46. Manin, J., et al., *Effects of Oxygenated Fuels on Combustion and Soot Formation/Oxidation Processes.* SAE Int. J. Fuels Lubr., 2014. **7**(3): p. 704-717.
47. Settles, G.S., *Schlieren and Shadowgraph Techniques: Visualizing Phenomena in Transparent Media.* 2001, Berlin, Germany: Springer-Verlag.
48. Pickett, L.M., S. Kook, and T. Williams, *Visualization of diesel spray penetration, cool-.* SAE International Journal of Engines, 2009. **2**(1): p. 439-459.
49. Naber, J. and D.L. Siebers, *Effects of gas density and vaporization on penetration and dispersion of diesel sprays.* SAE Technical Paper No. 960034, 1996.
50. Pastor, J.V., et al., *Segmentation of diesel spray images with log-likelihood ratio test algorithm for non-Gaussian distributions.* Applied Optics, 2007. **46**(6): p. 888-899.
51. Higgins, B. and D. Siebers, *Measurement of the Flame Lift-off locations on DI diesel Sprays Using OH* chemiluminescence.* SAE Technical Paper No. 2001-01-0918, 2001.
52. Gaydon, A.G., *The Spectroscopy of Flames*. 1974: Chapman and Hall.
53. Higgins, B. and D. Siebers, *Measurement of the Flame Lift-off locations on DI diesel Sprays Using OH* chemiluminescence.* SAE Technical Paper, 2001.
54. Lillo, M. and L.M. Pickett, *Diesel spray ignition detection and spatial/temporal correction.* SAE International Journal of Engines, 2012. **5**(3).
55. Pickett, L.M., S. Kook, and T.C. Williams, *Visualization of diesel spray penetration, cool flame, ignition, high-temperature combustion, and soot formation using high-speed imaging.* SAE technical paper No. 2009-01-0658, 2009.
56. Peters, N., *Turbulent combustion*. 2000: Cambridge university press.
57. Espey, C. and J.E. Dec, *The effect of TDC temperature and density on the liquid-phase fuel penetration in a DI diesel engine.* SAE Technical Paper No. 952456, 1995.
58. Pastor, J.V., et al., *Fuel effects on the liquid-phase penetration of an evaporating spray under transient diesel-like conditions.* Fuel, 2011. **90**(11): p. 3369.3381.
59. Jung, Y., et al., *Measurement of liquid and vapour penetration of diesel sprays with a variation in spreading angle.* SAE Technical Paper No. 2015-01-0946, 2015.
60. Kook, S. and L.M. Pickett, *Liquid length and vapor penetration of conventional, Fischer-Tropsch, coal-derived, and surrogate fuel sprays at high-temperature and high-pressure ambient conditions.* Fuel, 2012. **93**: p. 539-548.
61. Canaan, R.E., et al., *The influence of fuel volatility on the liquid-phase fuel penetration in a heavy-duty diesel engine.* SAE Technical Paper No. 980510, 1998.
62. Benajes, J., et al., *Experimental characterization of diesel ignition and lift-off length using a single-hole ECN injector.* Applied Thermal Engineering, 2013. **58**: p. 554-563.
63. Malbec, L.M., et al., *Characterization of a set of ECN Spray A injectors: Nozzle to nozzle variations and effect of spray characteristics.* SAE International Joiurnal of Engines, 2013. **6**(3): p. 1642-1660.
64. Pickett, L.M. and D.L. Siebers, *Fuel effects on soot processes of fuel jets at DI diesel conditions.* SAE Technical Paper No. 2003-01-3080, 2003.
65. Payri, F., et al., *Lift-off length and KL extinction measurements of biodiesel and Fischer-Tropsch fuels under quasi-steady diesel engine conditions.* SAE International Journal of Engines, 2011. **4**(2): p. 2278-2297.
66. Jung, Y., et al., *Assessment of the ignition and lift-off length characteristics of a diesel spray with a transient spreading angle.* SAE Technical Paper No. 2015-01-1828, 2015.
67. Pope, S.B., *Computationally efficient implementation of combustion chemistry using in situ adaptive tabulation.* Combustion Theory and Modelling, 1997. **1**(1): p. 41-63.
68. Brown, P.N., G.D. Byrne, and A.C. Hindmarsh, *Vode - a Variable-Coefficient Ode Solver.* Siam Journal on Scientific and Statistical Computing, 1989. **10**(5): p. 1038-1051.

# Appendix A

## *Droplet thermo-physical properties*

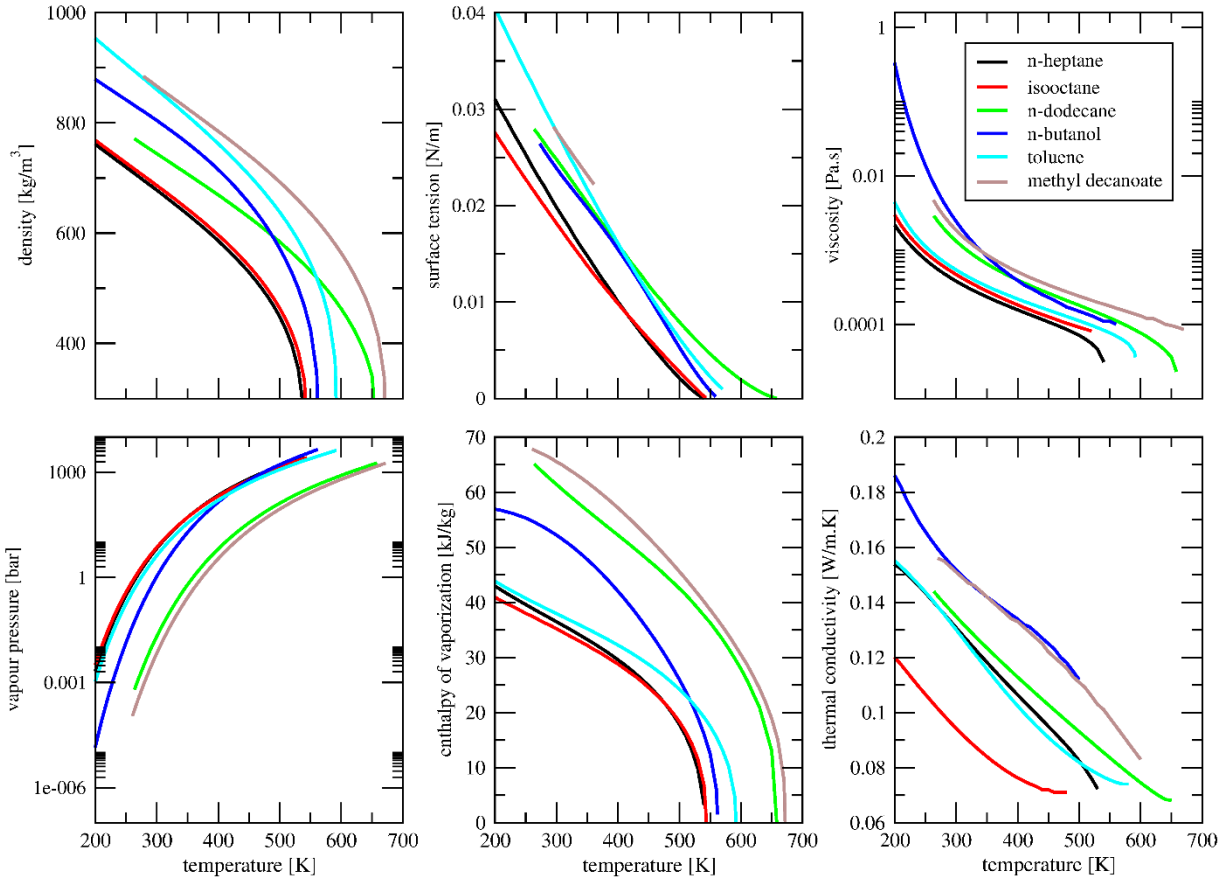


**Figure A: droplet thermo-physical properties as a function of temperature.**

## *Nozzles with cylindrically shaped holes*

| Nozzle Type | Nozzle Set # | | Orifice Diameter [mm] |
|---|---|---|---|
| | LAV | PSI | |
| A | 2 | 1 | 0.120 |
| B | 2 | 1 | 0.180 |
| C | 2 | 1 | 0.240 |
| D | 2 | 1 | 0.320 |

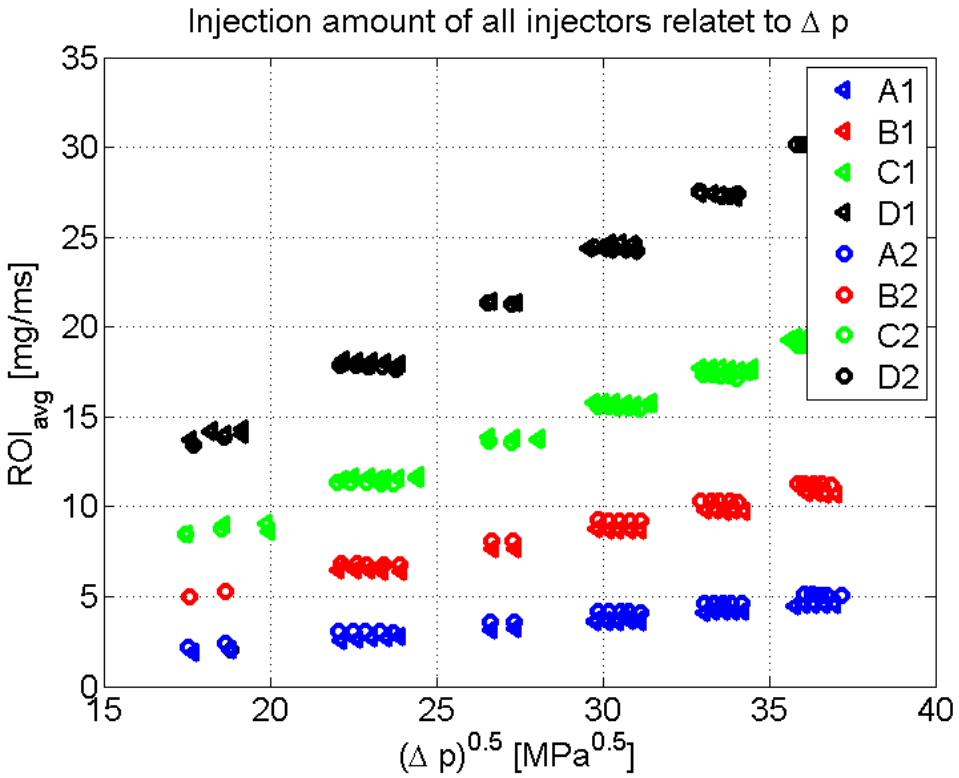


**Figure B: Average rate of Injection ($ROI_{avg}$) related to the pressure difference (ΔP) obtained at different combinations of injection pressures (40-140 MPa) and back pressures (11-3 MPa) for the nozzles C1 and C2 with orifice diameter 0.240 mm.**

### *Fuel composition*

The composition of all fuel blends that were used is expressed as a percentage of the volume of the total mixture. The detailed composition of each one of the fuel can be found in Table 14.

**Table 14. Composition of all fuel used expressed as a percentage of the volume of the total mixture.**

| | ***n*-heptane** | ***n*-heptane / Butanol** | ***n*-heptane / Toluene** | **OME234** | **OMEmix** |
|---|---|---|---|---|---|
| *n*-heptane | 100% | 90.9% | 70% | - | - |
| 1-butanol | - | 9.1% | - | - | - |
| Toluene | - | - | 30% | - | - |
| OME1 | - | - | - | 0.3% | - |
| OME2 | - | - | - | 33.1% | 0.5% |
| OME3 | - | - | - | 37.9% | 78.7% |
| OME4 | - | - | - | 27.4% | 19.8% |
| OME5 | - | - | - | - | 0.4% |
| OME6 | - | - | - | - | <0.1% |
| Trioxane | - | - | - | 1.2% | - |

### *Vaporization values*

The enthalpy of vaporization and boiling points of fuel components nad fuel blends are listed in Table 15.

**Table 15. Enthalpy of vaporization, boiling points and density of fuel components and fuel blends.**

| | Enthalpy of vaporization [kJ/mol] | Boling point [°C] at 1 atm. | Density [kg/m$^3$] at 298K |
|---|---|---|---|
| *n*-heptane | 36 | - | 684 |
| 1-butanol | 52 | - | 810 |
| Toluene | 37 | - | 867 |
| OME2 | - | 104 | 960 |
| OME3 | - | 155 | 1030 |
| OME4 | - | 200 | 1070 |
| Heptane / Butanol | - | - | 695 |
| Heptane / Toluene | - | - | 739 |
| OME234 | - | - | 1015 |
| OMEmix | - | - | 1046 |

### *Flame temperature and soot concentration*

The measured flame temperatures and soot amounts of the three *n*-heptane blends are presented in Table 16.

**Table 16. Temperature and KL values for 800 K, 900 K and 1000 K of ambient temperature.**

| Ambient temperature | 800 K | | 900 K | | 1000 K | |
|---|---|---|---|---|---|---|
| | KL [-] | T [K] | KL [-] | T [K] | KL [-] | T [K] |
| *n*-heptane | $2.59 \times 10^{-10}$ | 2451 | $3.20 \times 10^{-10}$ | 2502 | $3.47 \times 10^{-10}$ | 2638 |
| Heptane / Butanol | $3.38 \times 10^{-10}$ | 2410 | $4.58 \times 10^{-10}$ | 2463 | $4.5 \times 10^{-10}$ | 2581 |
| Heptane / Toluene | $5.32 \times 10^{-10}$ | 2489 | $4.50 \times 10^{-10}$ | 2584 | $5.82 \times 10^{-10}$ | 2665 |